IMPACT OF WIND ENERGY CONVERSION SYSTEMS ON GENERATOR DISTANCE PHASE BACKUP PROTECTION

A Thesis

Submitted to the College of Graduate and Postdoctoral Studies

In Partial Fulfillment of the Requirements

For the Degree of Master of Science

In the Department of Electrical and Computer Engineering

University of Saskatchewan

Saskatoon, Saskatchewan

By

Fei Sun

PERMISSION TO USE

I agree that the Library, University of Saskatchewan, may make this thesis freely available for inspection. I further agree that permission for copying of this thesis for scholarly purpose may be granted by the professor or professors who supervised the thesis work recorded herein or, in their absence, by the Head of the Department or the Dean of the College in which the thesis work was done. It is understood that due recognition will be given to me and to the University of Saskatchewan in any use of the material in this thesis. Copying or publication or any other use of this thesis for financial gain without approval by the University of Saskatchewan and my written permission is prohibited.

Request for permission to copy or to make any other use of the material in this thesis in whole or part should be addressed to:

Head of the Department of Electrical and Computer Engineering

University of Saskatchewan

57 Campus Drive

Saskatoon, Saskatchewan S7N 5A9

Canada

ABSTRACT

The need for clean, renewable energy has resulted in new mandates to augment, and in some cases replace conventional, fossil based generation with renewable generation resources. Wind generation is among those resources that have been at the center of attention. These resources are environmentally friendly, renewable, and they do not produce green-house gases. Therefore, there has been a significant growth in the integration of wind power into power systems networks in recent years. This structural change in power systems results, however, in new concerns regarding the reliable and secure operation of the power system with high penetration of wind energy conversion systems.

This thesis investigates the impact of large doubly-fed induction generator- and full-frequency converter-based wind farms on the performance of generator distance phase backup protection (Relay (21)) and the generator capability curves. In this context, comprehensive studies are conducted on a sample power system incorporating large DFIG- and FFC-based wind farms tapped to the transmission system. The results of these studies which provide an in-depth assessment of Relay (21) performance in the presence of this type of wind energy conversion systems show that a wind farm tapped to a transmission line has an adverse effect on the distance phase backup protection of a nearby generator. The severity of such an impact varies according to the fault type and its location. Moreover, the adverse effect of the wind farms on Relay (21) performance extends to affect the coordination between generator distance phase backup protection and the generator overexcited capability limits. Such an impact varies also according to the fault type, fault location and generator loading. The time-domain simulation studies are carried out using the ElectroMagnetic Transient Program (EMTP/RV).

ACKNOWLEDGEMENTS

My utmost sincere gratitude goes to my supervisor Dr. Sherif O. Faried. I sincerely appreciate it that his comprehensive knowledge taught me in developing my academic understanding, his patience helped me to attain further knowledge in the field and his wisdom nourished my mind. I am highly grateful to his strong support of my M.Sc. study and my research.

I would also like to address my gratitude to Dr. Elsamahy for his invaluable help and his precious time in providing his knowledge and his advice. And I would like to give my appreciation to Keaton A. Wheeler for his great help in cultivating a deeper understanding of my research.

Last but not least, I want to thank my beloved mother X.H. Liu and my farther L. Sun for their unlimited support in my study, my life and my career.

TABLE OF CONTENTS

LIST OF FIGURES

LIST OF TABLES

LIST OF SYMBOLS

AC	Alternating Current
AVM	Average value model
BtB	Back to back
CT	Current transformer
d	Direct axis
DC	Direct current
DFIG	Double fed induction generator
e_d, e_q	d- and q- axis components of the stator voltage
E_f	Internal or rotor field excitation voltage
e_{fd}	Filed voltage
G	Generator
GCC	Generator capability curve
GOEC	Generator steady-state overexcited capability limit
GSC	Grid side converter
HV	High-voltage
i_d, i_q	d- and q- axis components of the stator current
I_{Line1}, I_{Line2}	Line currents
L_{11d}	Self-inductance of the d-axis damper winding
L_{11q}, L_{22q}	Self-inductances of the q-axis damper winding
L_{ad}	d-axis magnetizing inductance
L_{aq}	q-axis magnetizing inductance
L_d, L_q	d- and q- axis components of the stator inductance
L_{ffd}	Self-inductance of the field winding

LV	Low-voltage
MTA	Relay (21) Maximum Torque Angle
MVA	Apparent power
MVAR	Reactive power
MW	Active power
P	Real power
$P_{bus1\ to\ M}$	Active power flows from Bus 1 to Bus M
P_{DFIG}	DFIG-based wind farm active power
PEMI	Percentage error in the measured impedance by Relay (21)
P_{gen}	Generator active power
PMSG	Permanent-magnet synchronous generator
PMW	Pulse-width modulated
Q	Reactive power
q	Quadrature axis
$Q_{bus1\ to\ M}$	Reactive power flows from Bus 1 to Bus M
Q_{DFIG}	DFIG-based wind farm reactive power
Q_{gen}	Generator reactive power
R_{1d}, R_{2d}	d-axis damper winding resistances
R_{1q}, R_{2q}	q-axis damper winding resistances
R_{21}	Relay (21)
R_a	Armature resistance
R_c	Current transformation ratio
R_L	Resistance of the series capacitor compensated transmission line
RPF	Rated power factor

RPFA	Rated power factor angle
RSC	Rotor-Side Converter
R_v	Voltage transformation ratio
t	Time
T_{ELEC}	Electrical torque
T_{MECH}	Mechanical torque
V_b	Infinite-bus voltage
V_{bd}, V_{bq}	d- and q- axis components of infinite-bus voltage
V_C	Voltage across the capacitor of the series capacitor compensated transmission line
V_{Cd}, V_{Cq}	d- and q- axis components of voltage across the capacitor of the series capacitor compensated transmission line
V_L	Voltage across the inductance of the series capacitor compensated transmission line
V_{Ld}, V_{Lq}	d- and q- axis components of voltage across the inductance of the series capacitor compensated transmission line
V_R	Voltage across the resistance of the series capacitor compensated transmission line
V_{Rd}, V_{Rq}	d- and q- axis components of voltage across the resistance of the series capacitor compensated transmission line
VT	Voltage transformer
V_t	Generator terminal voltage
V_{td}, V_{tq}	d- and q- axis components of generator terminal voltage
WF	Wind farm
X_C	Series capacitor reactance

X_d	Generator direct-axis synchronous reactance
X_L	Inductive reactance of the series capacitor compensated transmission line
X_s	Generator stator reactance
Z_1	Zone 1
Z_2	Zone 2
Z_{21}	Relay (21) reach
Z_3	Zone 3
Z_{GCC}	Maximum setting of Relay (21) to keep the coordination with GOEC limit
Z_{max}	The maximum setting of Relay (21)
Z_N	Impedance measured by relay (21) without wind farm
Z_{sl}	Transmission line series impedance
Z_t	Transformer series impedance
Z_w	Impedance measured by relay (21) with wind farm
Ψ_{1d}	d-axis damper winding flux linkage
Ψ_{1q}, Ψ_{2q}	q-axis damper winding flux linkages
Ψ_d, Ψ_q	d- and q- axis components of the stator flux linkages
ω	Angular velocity
ω_0	Synchronous frequency (337 rad/sec)
θ_N	Angle of the impedance measured by relay (21) without wind farm
θ_w	Angle of the impedance measured by relay (21) with wind farm

1. INTRODUCTION

1.1 Renewable Energy and Large Wind Farms

Unlike fossil energy, such as coal, petrol, and natural gas, renewable energy is collected from the resources that can be replenished over a short period of time, such as sunlight, wind, rain, tides, waves and geothermal heat [1]. The energy consumption from such sources is growing rapidly in recent years. In 2012, renewable energy contributed 19% to the world energy consumption [1]. It is believed that this clean, sustainable energy will become the solution to the global warming effect and the depletion of coal and oil in the near future.

In the renewable energy family, wind energy is among the fastest growing renewable energy technologies in the world. Increasing by approximately 30% a year globally over the last decade, wind energy has proven to be a clean, abundant and completely renewable source of energy. From 2004 to 2014, wind power had grown more than sevenfold from 47GW to 369GW. Canada has a total installation of 10204 MW by June 2015 [2], [3]. Owing to the rapidly increasing use of wind power, the aspect of integrating high levels of wind power into the grid has become a reality. Examples of large wind farms in the world are the 6000 MW Gansu wind farm in China, the 1320 Alta Wind Energy Center in California, the781.5 MW Roscoe wind farm in Texas and the 845 MW Shepherds Flat wind farm in Oregon [4].

Integrating more and more large capacity of wind farms into the power grid will surely bring some potential undesirable impacts, especially on the existing protective relays. Until now, these relays are set without considering the presence of wind farms.

1.2 Generator Protection [5] - [7]

There are many different types of faults that synchronous generators may experience and, therefore, many different types of protection. All generators will not have the same level of protection, however. As a general rule, the larger, more expensive machines will have the greatest number of different protective systems simply because serious damage of these units is very costly, both in terms of the repair and also the cost due to the unavailability of the unit. Generally, all generators will have basic protection against stator short circuit, but not all generators will have all of the other protective measures described concisely in this section. Table 1.1 provides an overview of the “major” synchronous generator protections.

Table 1.1: An overview of major synchronous generator protections [7].

Problem Location	Type of Problem
Stator winding	Phase fault
	Ground fault
	Turn-to-turn fault
	Open circuit
	Overheating
	Overvoltage
	Unbalanced current
	Generator fault backup
	External fault backup
Field winding	Shorted winding
	Grounded winding
	Overheating
N/A	Motoring
	Loss of excitation
	Loss of synchronism

1.3 Distance Relay Fundamentals [5] - [8]

Distance relays utilize a combination of the voltage and current at the relay location to determine the apparent impedance seen by the relay under all conditions. In this context, the apparent impedance is defined as the relay phasor voltage divided by the relay phasor current, where both quantities are in per unit and are measured at the relay location. When there is no fault present, the relay will see normal voltages and currents, resulting in rather large values of the apparent impedance magnitude, with an impedance angle corresponding to the load power factor. When plotted on the complex impedance (Z) plane, the apparent impedance for this type

of normal condition will usually lie near the real axis, but can be either positive or negative, depending on the direction of power flow. Reactive power flow will move the apparent impedance off the real axis in either direction, depending again on the direction of flow.

It should be recognized immediately that, because the distance relay uses both the current and voltage signals at the relay location, it is inherently directional. Viewed as fundamental frequency phasor quantities, a positive direction of power flow is indicated when the current phase is within 90° of the voltage.

Under fault conditions, the impedance viewed at a relay location will change drastically. First, the voltage will usually be depressed to some degree and the current will be much greater than the normal condition. This translates into a much smaller apparent impedance, which is largely reactive because the transmission line impedance between the relay and the fault point is largely reactive, except for possible arc resistance. This means that low values of impedance can be interpreted as a fault condition, with the direction to the fault point being known, as well as the approximate ohmic value, which can be interpreted as a distance to the fault.

Distance relays are designed such that a maximum impedance seeing can be adjusted to form a threshold for tripping. These relay thresholds are often plotted in the complex Z plane and may take the form of straight lines, circular arcs or complete circles. An example of a relay with three zones of protection is shown in Figure 1.1, which illustrates a circular characteristic passing through the origin, which is commonly known as a “mho” characteristic. Measurements taken by the relay that fall close to the origin and inside of the specified threshold setting are identified as faults for which the relay should operate. Measurements taken that result in impedance outside the threshold settings are conditions for which the relay should not operate. Timers are used to delay clearing if the fault is observed to fall in Zone 2 or Zone 3, with increasing delays for the more remote zones. This allows the distance relay to act as backup protection for adjacent lines.

In most cases, distance relays are set to “reach” a given distance along the protected transmission line, that is, the threshold setting is translated into a given ohmic value that is converted into the desired distance. A common reach setting might be 80 or 90% of the total length of the protected line. There is an obvious danger of trying to reach exactly 100% of the line length, as any small error may cause an incorrect line trip due to reaching beyond the remote bus. Many distance relays offer two or more “zones” of protection, so that measurements of

more distant faults will be cleared, but with a given time delay. An example of a protected transmission line with time graded settings is shown in Figure 1.2.

Using time-graded distance protection, as shown in Figure 1.2, there is a portion of the transmission line for which all faults are within the Zone 1 setting of relays at both ends and, therefore, will be cleared without intentional time delay. Consider a line that has relays set for Zone 1 reach of 80% of the line length. This condition results in 40% of all faults being cleared following a time delay, i.e. Zone 2 clearing. This time delay may not be acceptable, especially on EHV lines that often are relied upon for high power transfer. Thus, distance protection alone may be considered inadequate for "some" transmission lines.

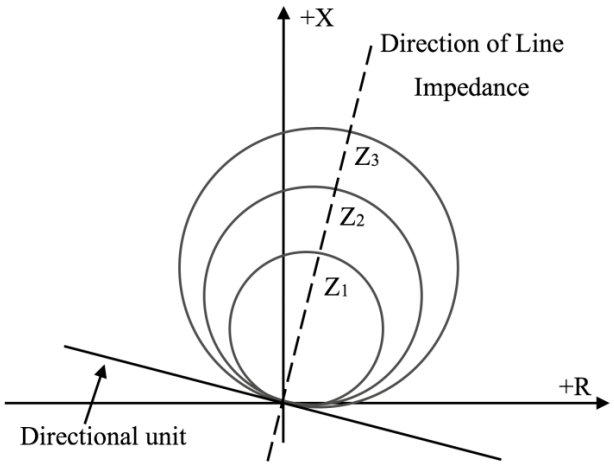

Figure 1.1: Distance protection zones in the Z plane.

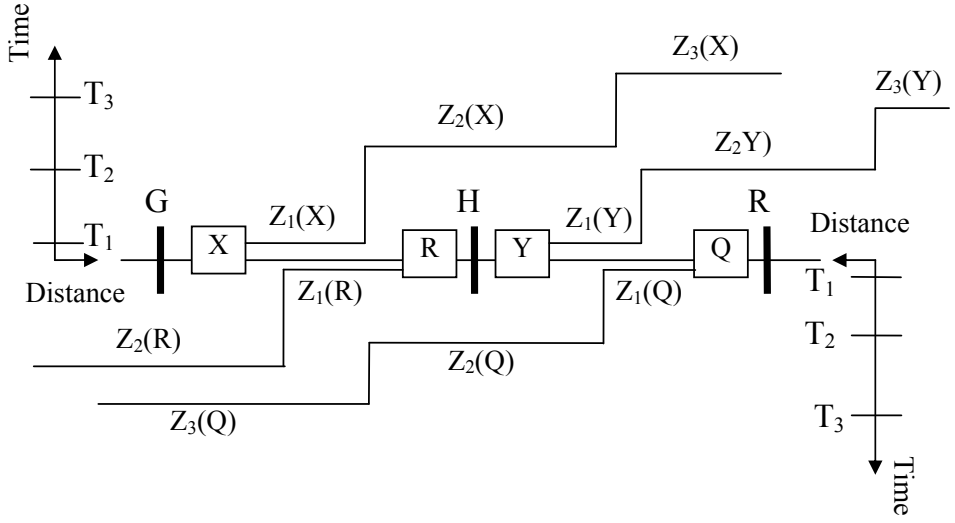

Figure 1.2: Distance relay different zones and graded time delay schematic: distance protection zones in the Z plane and zoned distance protection on adjacent transmission lines.

1.4 Wind Turbine

A wind turbine is a device that converts the wind's kinetic energy into electrical power [9]. The wind farm, which consists of multiple arrays of large turbines, is becoming a more and more important source of renewable energy. It is widely used in many countries as part of their energy strategy to decrease the emission of carbon dioxide and the reliance on fossil fuels.

There are horizontal and vertical types of wind turbines, and the wind farms are equipped with horizontal types, due to the low power efficiency of the vertical types. Common horizontal types of wind turbines include DFIG (Doubly-fed Induction Generator) wind turbine and FFC (Full-Scale Frequency Converter) wind turbine. The DFIG-based wind turbines are becoming increasingly popular because of the low cost of the converter, since the capacity and the size of the converters of a DFIG wind turbine are much smaller than those of an FFC wind turbine with the same output capacity to the grid.

1.5 Doubly-fed Induction Generator Wind Turbine

The basic structure of a doubly-fed induction generator (DFIG) wind turbine is shown in Figure 1.3. The stator of the induction machine is directly connected to the grid and the wound rotor windings are connected to the grid through slip rings and an indirect AC-AC converter system which controls both the rotor and the grid currents. The AC-AC converter system consists of two three-phase pulse-width modulated (PWM) Voltage-Sourced Converters (VSC) connected by a DC bus. A line inductor and an AC filter are used at the DC/AC converter to improve the power quality [10].

The control of the DFIG is realized by controlling the AC/DC converter and DC/AC converter using vector control techniques. The function of the AC/DC converter is to control the active and reactive powers delivered to the grid, and to follow a tracking characteristic to adjust the generator speed for optimal power generation depending on the wind speed. On the other hand, the function of the DC/AC converter is to keep the DC bus voltage constant and to support the grid with reactive power during system faults [11]. Details on DFIG wind turbine controls are given in [12].

The main advantage of the DFIG is the low cost of its converters as their rating is typically 25% to 30% of the DFIG rated power. As a result, the cost of the converters and electromagnetic interference (EMI) filters is also reduced.

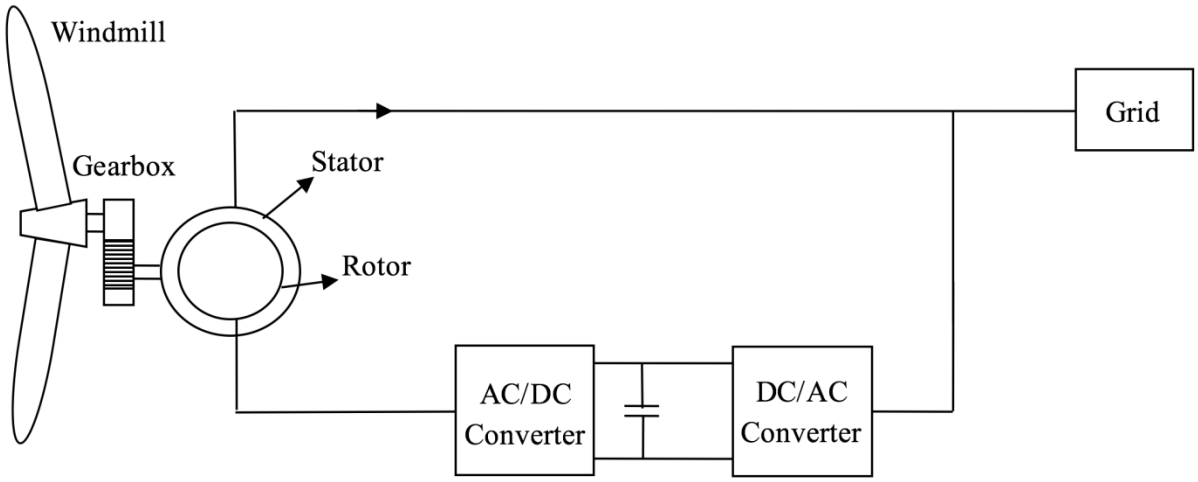

Figure 1.3: Schematic diagram of a DFIG wind turbine.

1.6 Full-Scale Frequency Converter Wind Turbine

Full-scale Frequency Converter (FFC) wind turbines are becoming popular in wind farms, since they can meet the stringent grid code requirements more easily than DFIG turbines. This is because FFC wind turbine has full control capability for real and reactive power output, with the generator decoupled from the grid.

The FFC wind turbine employs a permanent–magnet synchronous generator (PMSG) that has a large number of poles; hence a gear box is not required. This is also known as a direct-drive wind turbine generator where the synchronous machine rotates at the slow turbine speed and generates electrical power with frequency well below that of the gird (the synchronous frequency). The increased generator weight is offset by the absence of the gearbox. Further, the reliability and maintenance considerations for a gearbox are eliminated. Hence, this concept is particularly attractive for offshore locations [13].

Figure 1.4 shows a FFC PMSG wind turbine connected to the grid through an AC-AC converter system. Depending on the size of the wind turbine, the PMSG side converter (AC/DC converter) can be either a diode rectifier or a VSC. On the other hand, the DC/AC converter is

typically a VSC. In the studies conducted in this thesis, the back-to-back (BtB) VSC topology is adopted [14].

Similar to the DFIG, the control of the FFC is realized by controlling the AC/DC converter and DC/AC converter using also vector control techniques [11]. The AC/DC converter controls the active power delivered by the PMSG, and follows a tracking characteristic to adjust the PMSG speed for optimal power generation depending on wind speed. The function of DC/AC converter is maintaining the DC bus voltage at its desired level, i.e. transmitting the active power delivered to the DC link by the AC/DC converter. DC/AC converter also controls the reactive power delivered to the grid.

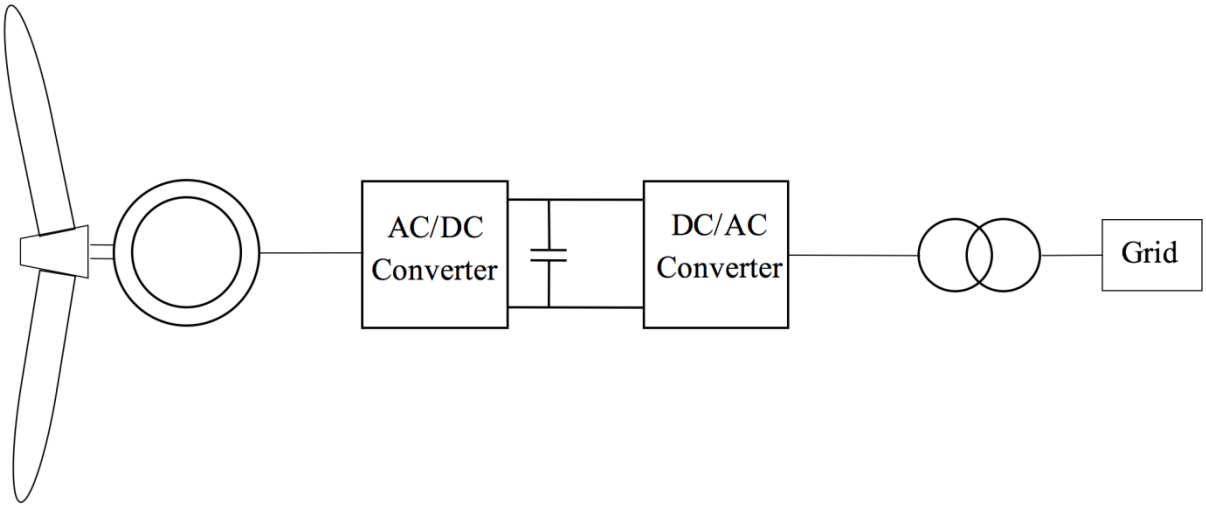

Figure 1.4: Simple Schematic diagram of a FFC wind turbine.

1.7 Literature Review

Renewable energy, especially wind power using wind turbine generators (WTGs), is popular these days, not only because it is a green and environmental-friendly energy, but also because the governmental policies intend to bring up the penetration level of this type of energy [15]. Under this situation, the expansion of the WTGs is assured. Yet the risks it brings are challenging the existing power system. During the last few years, research has been conducted in different aspects in order to identify the potential problems those WTGs might introduce to the security of the power system.

Reference [15] investigated the protection challenges which can be brought by DFIG and FFC wind turbines. The results of these investigations reveal that FFC wind turbines response to

symmetrical and unsymmetrical faults is insignificant and their fault current magnitudes usually stay under the full-load current. The impact of the Low Voltage Ride Through (LVRT) capability of the wind turbine on distance relays is reported in [16]. As the system encounters a system fault, the voltage dip it brings can rapidly demagnetize the DFIG stator, resulting in large outrush currents in both the stator and rotor windings [17]. This leads to the requirement of LVRT capability to maintain wind farms connections during voltage dips [18]. The most common way to reach this is to use crowbar units, which automatically disconnect the rotor excitation before experiencing high current, making the DFIG behave as a conventional squirrel cage induction generator without controllability. This characteristic would further deteriorate the terminal voltage, since the stator needs to absorb reactive power from the system to keep excitation. Furthermore, this absorption of reactive power when the crowbar is activated can lead the distance relay to lose the coordination with protection system [16].

As it can be noticed from the previous discussion, most of the published research on the impact of large wind farms on power system protection is focused on transmission line distance relays. Virtually, no research work has been reported until now on the impact of wind energy conversion systems on generator distance phase backup protection.

1.8 Research Objective and Scope of the Thesis

Power system protection is considered as the first line of defense against system disturbances. Therefore, fast, accurate and reliable operation of the power system protective system is vital to power system security. Studies of past major disturbances and blackouts in North America showed that protective relay mal-operation either caused or aggravated the situation. As a result, it is very important to study the performance of the protection system for different operating conditions and system configurations.

Reported studies on the impact of transmission line midpoint Static Synchronous Compensator (STATCOM) on the performance of generator phase backup protection (distance Relay (21)) reveal that the midpoint STATCOM has an adverse effect on such a protection which can be in the form of under-reach, overreach or a time delay [19], [20]. As the Grid-Side Converters (GSC) of Doubly-Fed Induction Generator (DFIG) and Full-Frequency Converter (FFC) wind turbines appear to the generators in nearby generating stations as STATCOMs, high penetration of these types of renewable energy conversion systems is expected to have an

adverse effect on the performance of generator distance relays. Moreover, as many DFIG-based wind farms are equipped with STATCOMS for reactive power support, this adverse effect is more aggravated.

The objective of this research is to carry out extensive studies to explore the impact of DFIG- FFC-based wind farms on the generator distance phase backup protection (distance Relay (21)) in order to identify the important issues that protection engineers need to consider when designing and setting the generator protection system. The results of these investigations provide an in-depth assessment of Relay (21) performance in the presence of these types of wind energy conversion systems.

2. POWER SYSTEM MODELING FOR LARGE DISTURBANCE STUDIES

2.1 General

In this chapter, the system used for the studies reported in this thesis is described and the mathematical models of its various components are presented. A digital time-domain simulation of a case study of the system during three-phase fault and line-to-line are presented at the end of this chapter.

2.2 System under Study

The system used in the investigations of this thesis is shown in Figure 2.1. It consists of a 700 MVA thermal generating station connected via a transformer to two large systems through two 500 kV transmission lines designated as L_1 and L_2. Two wind farms (DFIG- and FFC-based turbines) are tapped to L_1 and L_2 at buses M and N respectively. The compositions, ratings, operating wind speeds and power outputs of the wind farms are given in Table 2.1 and the system data are given in Appendix A. Faults are assumed to occur on L_1 at F_1 and F_2 at distances 100 km and 300 km respectively from Bus M and on L_2 at F_3 which is 200 km from Bus 1. Dynamic simulation studies on this test system are conducted using the EMTP/RV.

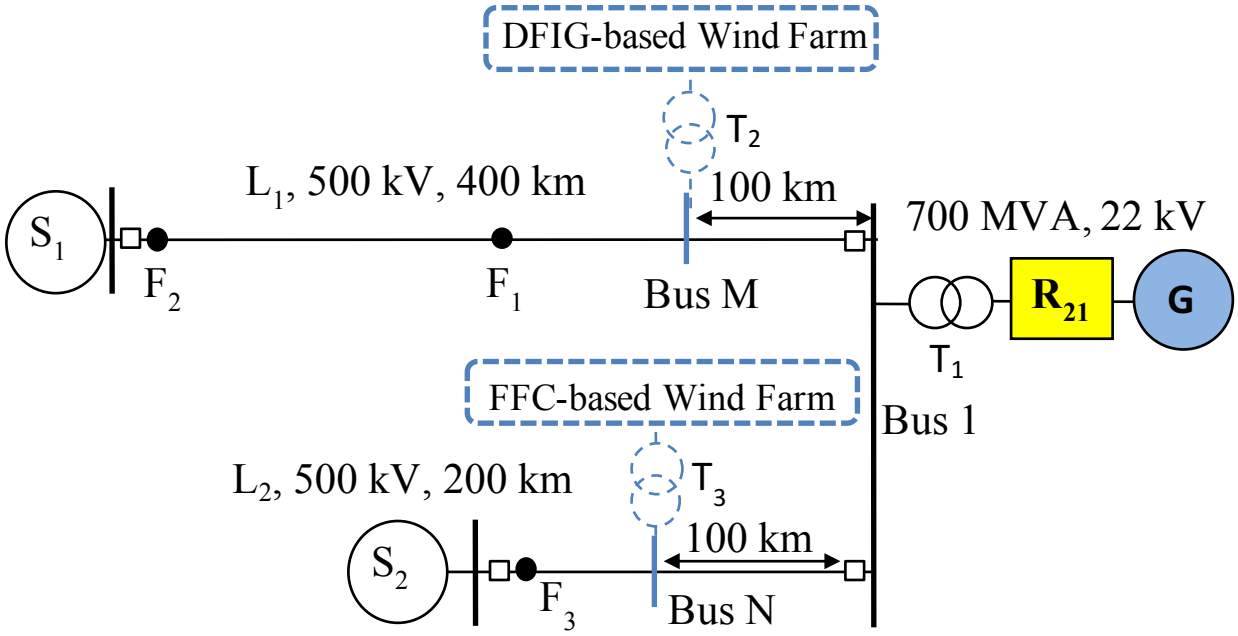

Figure 2.1: System under study.

Table 2.1: Wind farm compositions.

Wind farm	Rating, operating speed and output power
DFIG	Aggregated model of 400 × 1.5 MW wind turbines, wind speed = 11.24m/s, power ≈ 580 MW.
FFC	Aggregated model of 100 × 2 MW permanent–magnet synchronous generator (PMSG)-based wind turbines, wind speed = 15 m/s, power ≈ 200 MW.

2.3 Power System Modeling

The nonlinear differential equations of the system under study are derived by developing individually the mathematical models which represent the various components of the system, namely the synchronous generator, the DFIG-and FFC-based wind farms, the excitation system, the transmission line and the two large systems. Knowing the mutual interaction among these models, the whole system differential equations can be formed.

2.3.1 Modeling of the synchronous machine

In a conventional synchronous machine, the stator circuit consisting of a three-phase winding produces a sinusoidally space distributed magnetomotive force. The rotor of the machine carries the field (excitation) winding which is excited by a DC voltage. The electrical damping due to the eddy currents in the solid rotor and, if present, the damper winding is represented by three equivalent damper circuits; one on the direct axis (d-axis) and the other two on the quadrature axis (q-axis). The performance of the synchronous machine can be described by the equations given below in the d-q reference frame [21]. In these equations, the convention adopted for the signs of the voltages and currents are that v is the impressed voltage at the terminals and that the direction of positive current i corresponds to generation. The sign of the currents in the equivalent damper windings is taken positive when they flow in a direction similar to that of the positive field current as shown in Figure 2.2.

With time t expressed in seconds, the angular velocity ω expressed in rad/s $(\omega_0 = 377 rad/\sec)$ and the other quantities expressed in per unit, the stator equations become:

$$e_d = \frac{1}{\omega_0}\frac{d\Psi_d}{dt} - \frac{\omega}{\omega_0}\Psi_q - R_a i_d \tag{2.1}$$

$$e_q = \frac{1}{\omega_0}\frac{d\Psi_q}{dt} + \frac{\omega}{\omega_0}\Psi_d - R_a i_q \tag{2.2}$$

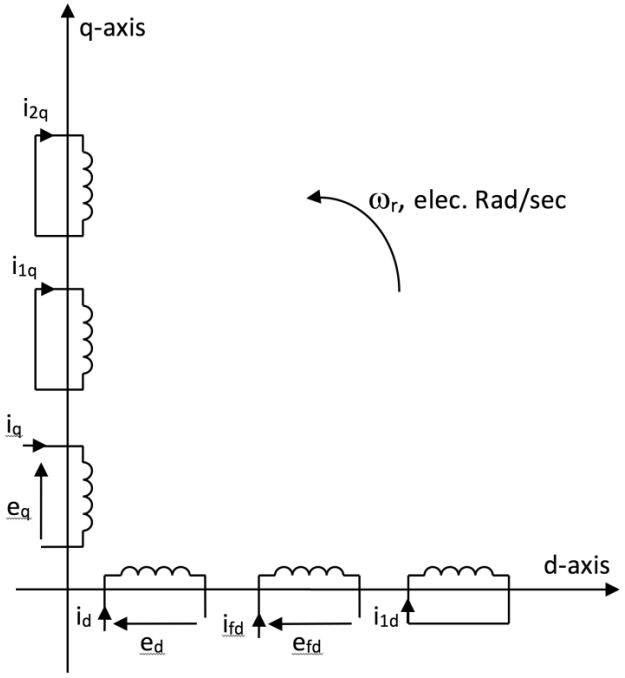

Figure 2.2: Modeling of the synchronous machine in the d-q reference frame.

The rotor equations:

$$e_{fd} = \frac{1}{\omega_0}\frac{d\Psi_{fd}}{dt} + R_{fd} i_{fd} \tag{2.3}$$

$$0 = \frac{1}{\omega_0}\frac{d\Psi_{1d}}{dt} + R_{1d} i_{1d} \tag{2.4}$$

$$0 = \frac{1}{\omega_0}\frac{d\Psi_{1q}}{dt} + R_{1q} i_{1q} \tag{2.5}$$

$$0 = \frac{1}{\omega_0}\frac{d\Psi_{2q}}{dt} + R_{2q} i_{2q} \tag{2.6}$$

The stator flux linkage equations:

$$\Psi_d = -L_d i_d + L_{ad} i_{fd} + L_{ad} i_{1d} \tag{2.7}$$

$$\Psi_q = -L_q i_q + L_{aq} i_{1q} + L_{aq} i_{2q} \tag{2.8}$$

The rotor flux linkage equations:

$$\Psi_{fd} = L_{ffd} i_{fd} + L_{ad} i_{1d} - L_{ad} i_d \tag{2.9}$$

$$\Psi_{1d} = L_{ad} i_{fd} + L_{11d} i_{1d} - L_{ad} i_d \tag{2.10}$$

$$\Psi_{1q} = L_{11q} i_{1q} + L_{aq} i_{2q} - L_{aq} i_q \tag{2.11}$$

$$\Psi_{2q} = L_{aq} i_{1q} + L_{22q} i_{2q} - L_{aq} i_q \tag{2.12}$$

The air-gap torque equation:

$$T_{ELEC} = \Psi_d i_q - \Psi_q i_d \tag{2.13}$$

The overall differential equations which describe the transient performance of the synchronous machine are given by the following matrix equation:

$$\left[\frac{dX_{syn}}{dt}\right] = \left[At_{syn}\right]\left[X_{syn}\right] + \left[Bt_{syn}\right]\begin{bmatrix} V_{td} \\ V_{tq} \\ e_{fd} \end{bmatrix} \tag{2.14}$$

where

$$\left[X_{syn}\right] = \begin{bmatrix} i_d & i_q & i_{fd} & i_{1q} & i_{1d} & i_{2q} \end{bmatrix}^T$$

$$\left[At_{syn}\right] = \left[L\right]^{-1}\left[Qt\right]$$

$$\left[Bt_{syn}\right] = \left[L\right]^{-1}\left[Rt\right]\left[L\right] = \begin{bmatrix} -L_d & 0 & L_{ad} & 0 & L_{ad} & 0 \\ 0 & -L_q & 0 & L_{aq} & 0 & L_{aq} \\ -L_{ad} & 0 & L_{ffd} & 0 & L_{ad} & 0 \\ 0 & -L_{aq} & 0 & L_{11q} & 0 & L_{aq} \\ -L_{aq} & 0 & L_{ad} & 0 & L_{11d} & 0 \\ 0 & -L_{aq} & 0 & L_{aq} & 0 & L_{22q} \end{bmatrix} \tag{2.15}$$

$$\left[Qt\right] = \begin{bmatrix} \omega_0 R_a & -\omega L_q & 0 & \omega L_{aq} & 0 & \omega L_{aq} \\ \omega L_d & \omega_0 R_a & -\omega L_{ad} & 0 & -\omega L_{ad} & 0 \\ 0 & 0 & -\omega_0 R_{fd} & 0 & 0 & 0 \\ 0 & 0 & 0 & -\omega_0 R_{1q} & 0 & 0 \\ 0 & 0 & 0 & 0 & -\omega_0 R_{1d} & 0 \\ 0 & 0 & 0 & 0 & 0 & -\omega_0 R_{2q} \end{bmatrix}$$

$$[Rt] = \begin{bmatrix} \omega_0 & 0 & 0 \\ 0 & \omega_0 & 0 \\ 0 & 0 & \omega_0 \\ 0 & 0 & 0 \\ 0 & 0 & 0 \\ 0 & 0 & 0 \end{bmatrix}$$

here, the superscript ^{T} means matrix transpose.

The synchronous machine swing equation can be written as:

$$\frac{2H}{\omega_o}\frac{d\omega}{dt} = T_{MECH} - T_{ELEC} \tag{2.16}$$

$$\frac{d\delta}{dt} = \omega - \omega_o \tag{2.17}$$

In the above two equations (2.16 and 2.17), ω is in radians per second, the inertia constant H is in seconds, and the load angle δ is in radians, ω_o is the synchronous frequency (377 rad/sec) and the mechanical and electrical torques T_{MECH} and T_{ELEC} are in per unit.

2.3.2 Modeling of the transmission line

A series capacitor-compensated transmission line may be represented by the *RLC* circuit shown in Figure 2.3 [22]. In the voltage phasor diagram shown in Figure 2.4, the rotor angle δ is the angle (in elec. rad) by which the q-axis leads the reference voltage V_b. The differential equations for the circuit elements, after applying Park's transformation [22], can be expressed in the d-q reference frame by the following matrix expressions.

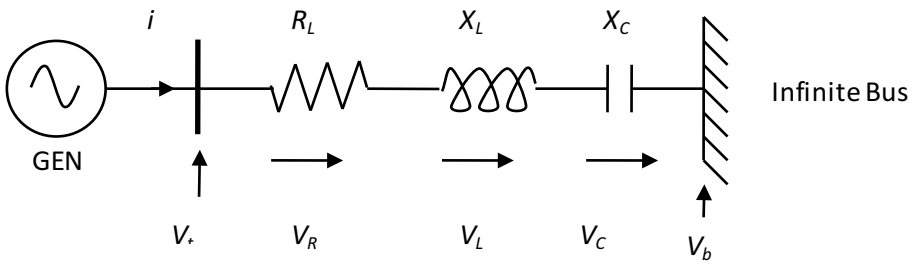

Figure 2.3: A series capacitor-compensated transmission line.

The voltage across the resistance:

$$\begin{bmatrix} V_{Rd} \\ V_{Rq} \end{bmatrix} = \begin{bmatrix} R_L & 0 \\ 0 & R_L \end{bmatrix} \begin{bmatrix} i_d \\ i_q \end{bmatrix} \tag{2.18}$$

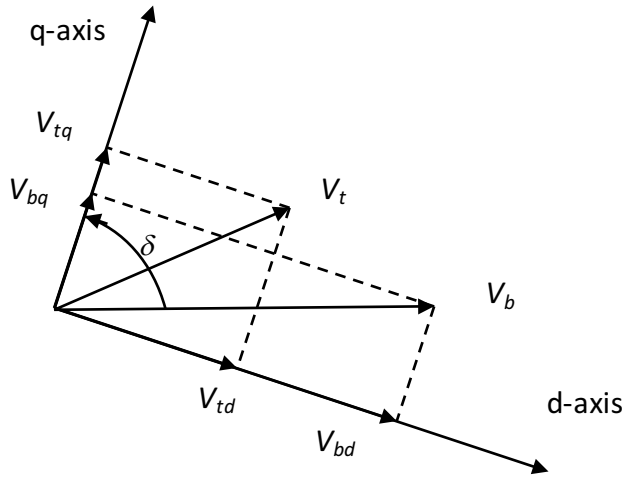

Figure 2.4: Voltage phasor diagram.

The voltage across the inductance:

$$\begin{bmatrix} V_{Ld} \\ V_{Lq} \end{bmatrix} = \begin{bmatrix} 0 & -\dfrac{\omega}{\omega_0} X_L \\ \dfrac{\omega}{\omega_0} X_L & 0 \end{bmatrix} \begin{bmatrix} i_d \\ i_q \end{bmatrix} + \begin{bmatrix} \dfrac{X_L}{\omega_0} & 0 \\ 0 & \dfrac{X_L}{\omega_0} \end{bmatrix} \begin{bmatrix} \dfrac{di_d}{dt} \\ \dfrac{di_q}{dt} \end{bmatrix} \tag{2.19}$$

The voltage across the capacitor:

$$\begin{bmatrix} \dfrac{dV_{Cd}}{dt} \\ \dfrac{dV_{Cq}}{dt} \end{bmatrix} = \begin{bmatrix} \omega_0 X_C & 0 \\ 0 & \omega_0 X_C \end{bmatrix} \begin{bmatrix} i_d \\ i_q \end{bmatrix} + \begin{bmatrix} 0 & \omega \\ -\omega & 0 \end{bmatrix} \begin{bmatrix} V_{Cd} \\ V_{Cq} \end{bmatrix} \tag{2.20}$$

The overall equations of the transmission line can be written as

$$\begin{bmatrix} \dfrac{dV_{Cd}}{dt} \\ \dfrac{dV_{Cq}}{dt} \\ V_{td} \\ V_{tq} \end{bmatrix} = [Att] \begin{bmatrix} V_{Cd} \\ V_{Cq} \end{bmatrix} + [Rt1] \begin{bmatrix} \dfrac{di_d}{dt} \\ \dfrac{di_q}{dt} \end{bmatrix} + [Rt2] \begin{bmatrix} i_d \\ i_q \end{bmatrix} + [Btt][V_b] \tag{2.21}$$

where

$$[Att]=\begin{bmatrix} 0 & \omega \\ -\omega & 0 \\ 1 & 0 \\ 0 & 1 \end{bmatrix}$$

$$[Rt1]=\begin{bmatrix} 0 & 0 \\ 0 & 0 \\ \frac{X_L}{\omega_0} & 0 \\ 0 & \frac{X_L}{\omega_0} \end{bmatrix}$$

$$[Rt2]=\begin{bmatrix} \omega_0 X_C & 0 \\ 0 & \omega_0 X_C \\ R_L & -\frac{\omega}{\omega_0} X_L \\ \frac{\omega}{\omega_0} X_L & R_L \end{bmatrix} \qquad (2.22)$$

$$[Btt]=\begin{bmatrix} 0 \\ 0 \\ \sin\delta \\ \cos\delta \end{bmatrix}$$

It is worth noting here that if the transmission line is not series capacitive compensated, the capacitive reactance and the voltage across the capacitor are set to zero in Equations (2.20, 2.21 and 2.22).

2.3.3 Excitation system

The block diagram representation of the excitation system used in this study is shown in Figure 2.5, and the corresponding data are given in Appendix A [22].

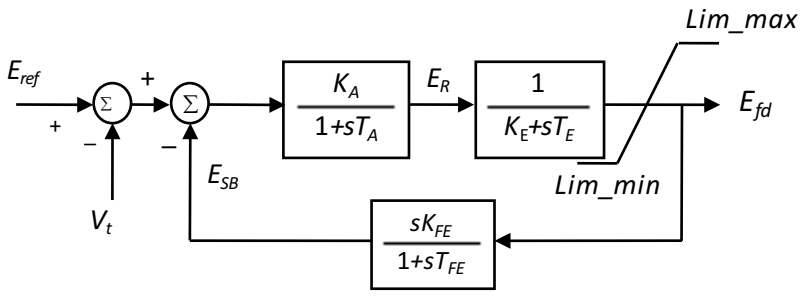

Figure 2.5: Block diagram of the excitation system.

Utilizing the relationship between the excitation system output voltage and the field voltage given by $E_{fd} = \frac{L_{ad}}{R_{fd}} e_{fd}$, the state-space equation of the excitation system can be derived from its block diagram and is given by

$$\left[\frac{dX_v}{dt}\right] = [At_v][X_v] + [Bt_v]\begin{bmatrix} V_t \\ E_{ref} \end{bmatrix} \tag{2.23}$$

where

$$[X_v] = \begin{bmatrix} e_{fd} & E_R & E_{SB} \end{bmatrix}^T$$

$$[At_v] = \begin{bmatrix} -\frac{K_E}{T_E} & \frac{1}{T_E}\frac{R_{fd}}{L_{ad}} & 0 \\ 0 & -\frac{1}{T_A} & -\frac{K_A}{T_A} \\ -\frac{K_E K_F}{T_E T_F}\frac{L_{ad}}{R_{fd}} & \frac{K_F}{T_F T_E} & -\frac{1}{T_F} \end{bmatrix} \tag{2.24}$$

$$[Bt_v] = \begin{bmatrix} 0 & 0 \\ -\frac{K_A}{T_A} & \frac{K_A}{T_A} \\ 0 & 0 \end{bmatrix}$$

2.3.4 Modeling of the transformer

The three-phase transformer is constructed by using three single-phase transformers connected in Delta (LV side)/Y grounded (HV side). The transformer leakage and magnetizing reactances as well as the winding resistances and core loss are represented in the model.

2.3.5 Modeling of the DFIG Wind Turbine

The basic configuration of a DFIG wind turbine is shown in Figure 2.6, where the stator of the induction machine is directly connected to the grid and the wound rotor is connected to the grid through a back-to-back (BtB) link. The BtB link consists of two, three-phase pulse-width modulated (PWM) VSCs (Rotor-Side Converter (RSC) and Grid-Side Converter (GSC)) coupled to a common DC bus. A line inductor and an AC filter are used at the GSC to improve power quality. A crowbar is used as a backup protection device. Details of DFIG wind turbines mathematical modeling and control are given in [23].

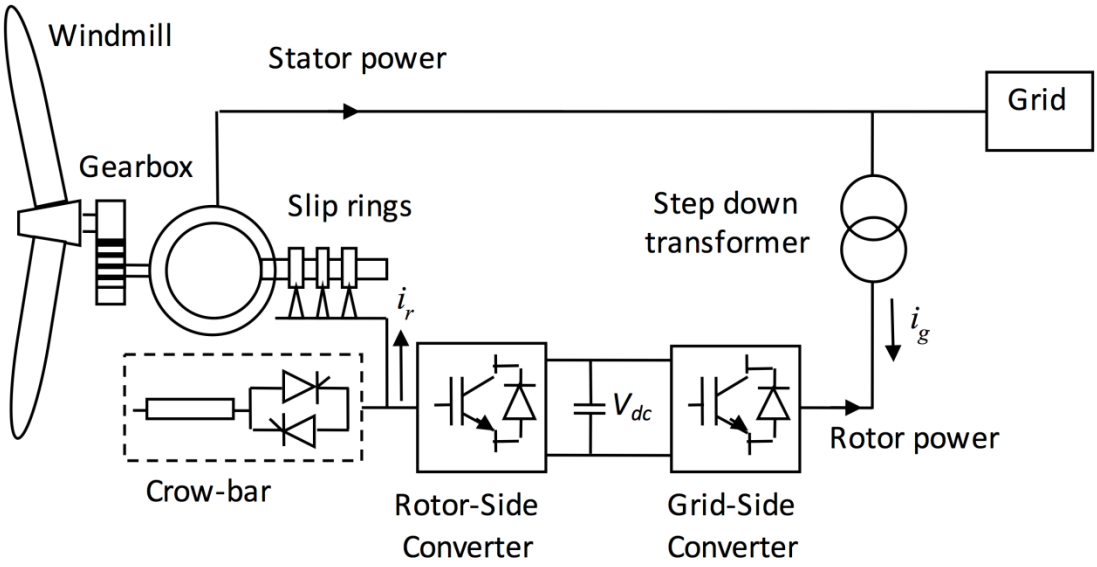

Figure 2.6: Schematic diagram of a DFIG wind turbine.

The aggregated model of 1.5 MW, 60 Hz DFIG wind turbines in [10] is used in this thesis. The model includes a pitch control to limit the maximum speed, a DC resistive chopper to limit the DC voltage and avoid the crowbar ignition during AC faults, a two-mass model to represent low frequency oscillations of the wind turbine drive system and over/under voltage protection. The DFIG converters are modeled with their average value models (AVM) [24], [25].

2.3.6 Modeling of the FFC Wind Turbine

The FFC concept uses a permanent–magnet synchronous generator (PMSG) connected to the grid through a BtB link as shown in Figure 2.7. Depending on the size of the wind turbine, the PMSG side converter (MSC) can be either a diode rectifier or a VSC. On the other hand, the GSC is typically a VSC. This thesis considers the BtB VSC topology.

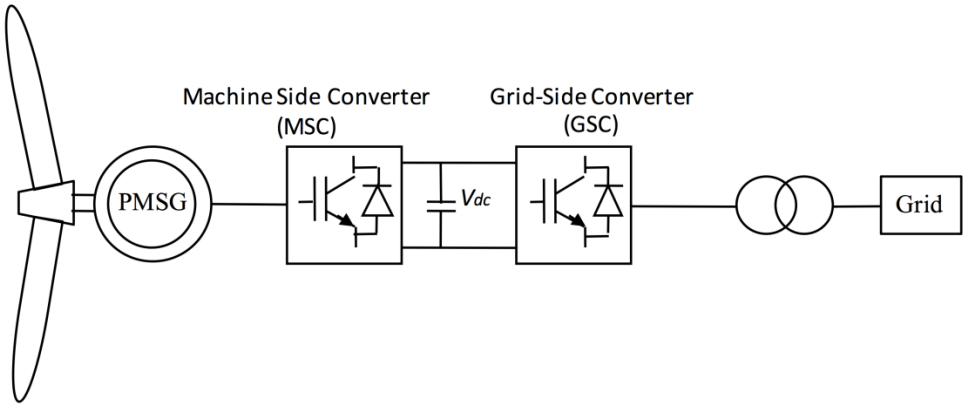

Figure 2.7: Schematic diagram of a FFC wind turbine.

Similar to the DFIG, the control of the FFC is achieved by controlling the MSC and GSC [25]. The MSC controls the active power delivered by the PMSG, and follows a tracking characteristic to adjust the PMSG speed for optimal power generation depending on wind speed. The function of GSC is maintaining the DC bus voltage, i.e. transmitting the active power delivered to the DC link by the MSC. It is also used to control the reactive power delivered to the grid. Details of permanent–magnet synchronous generator wind turbines mathematical modeling and control are given in [14].

A generic 2 MW, 60 Hz FFC model is used in studies of this thesis. The model includes a pitch control, DC chopper and over/under voltage protections. A two-mass model is used to represent the turbine drive system. The FFC converters are modeled with their AVMs.

2.3.7 Modeling of the two Large Systems

The two large systems, S_1 and S_2 are modeled by constant voltage source at the synchronous frequency behind a very small inductive reactance.

2.4 A Sample Case Study

In the studies conducted in this thesis, the ElectroMagnetic Transient Program (EMTP-RV) is used for modeling the various system components and producing the time-domain simulation results [26]. Due to the initialization process in the EMTP-RV, simulation results are displayed starting at time equal two seconds. Moreover, faults are assumed to occur at t = 2 seconds.

Figure 2.8 shows the power flow results for the bus voltages and the line real power flows of the system under study. The transient time responses of the generator real power output and speed(measured respectively with respect to the load angle and speed of generator), the DFIG- and FFC-based wind farm real power outputs, bus M and bus N voltages and the real power flows in the transmission lines during and after clearing three-cycle, three-phase and line-to-line faults at F_1 are shown respectively in Figures 2.9 and 2.10. Figures 2.11 and 2.12 show the same transient time responses for the cases of sustained three-phase and line-to-line faults at the same location. Such sustained faults are due to failures in the transmission line protection.

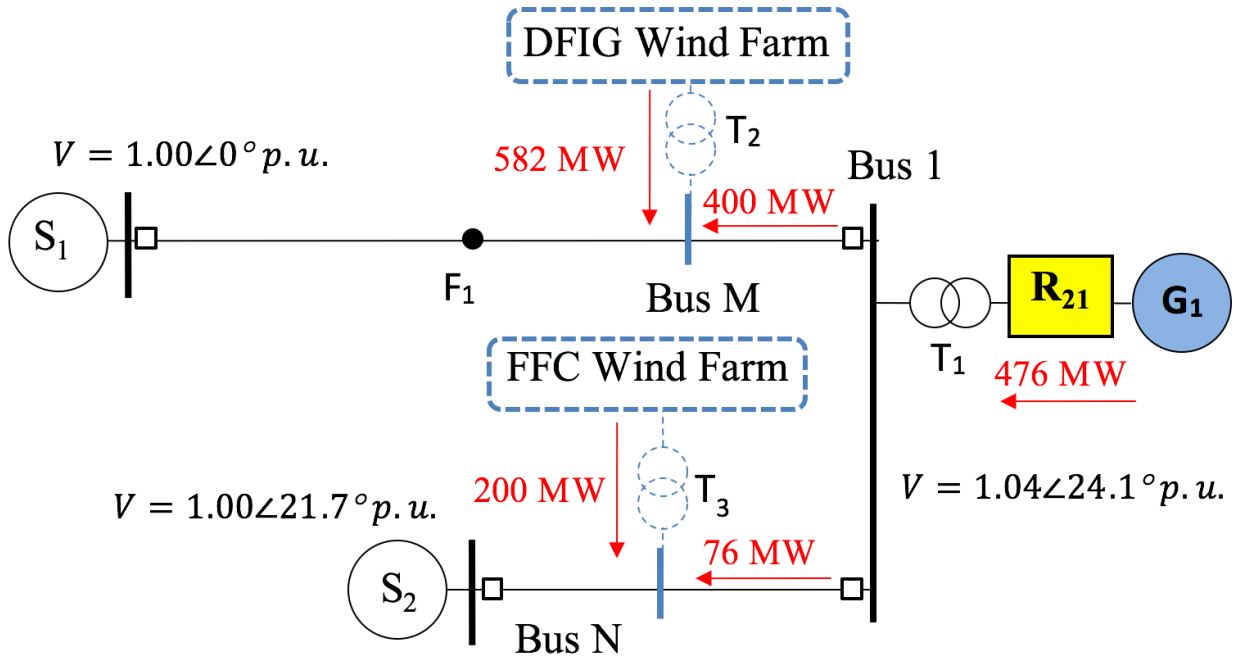

Figure 2.8: Load flow results of the bus voltages and real power flows of the system under study.

The following observations can be made from examining Figures 2.9 and 2.10 (successful fault clearings):

- The system is stable after fault clearing for both types of faults as the generator power and speed oscillate around their pre-fault steady-state values. The power flows on the transmission lines and the wind farm terminal voltages drop immediately at the instant of fault inception but recover after fault clearing.

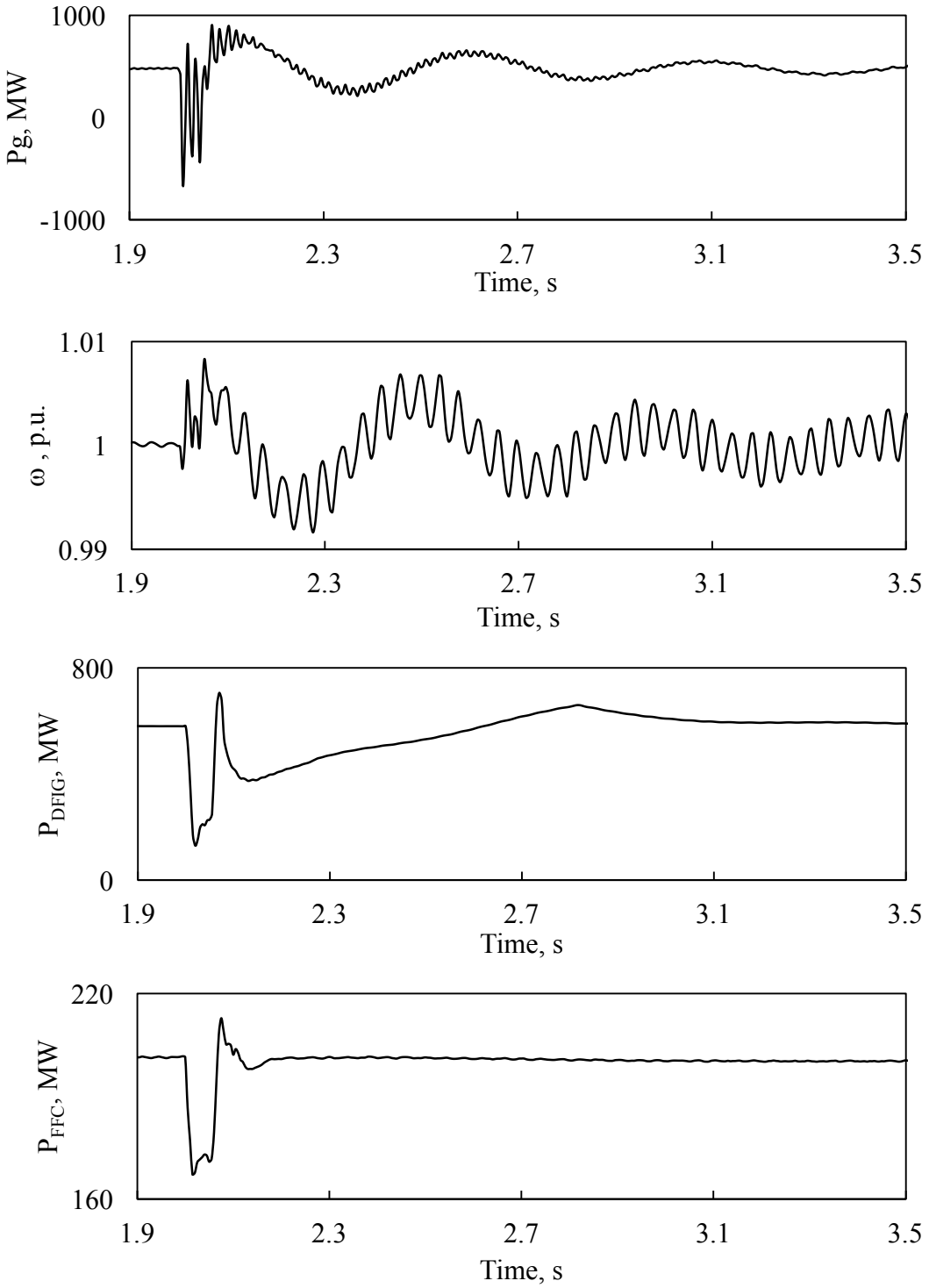

Figure 2.9: Transient time response of generator active power and speed, DFIG- and FFC-based wind farm active powers and terminal voltages and real power flow on L_1 and L_2 during and after clearing a three-cycle, three-phase fault at F_1.

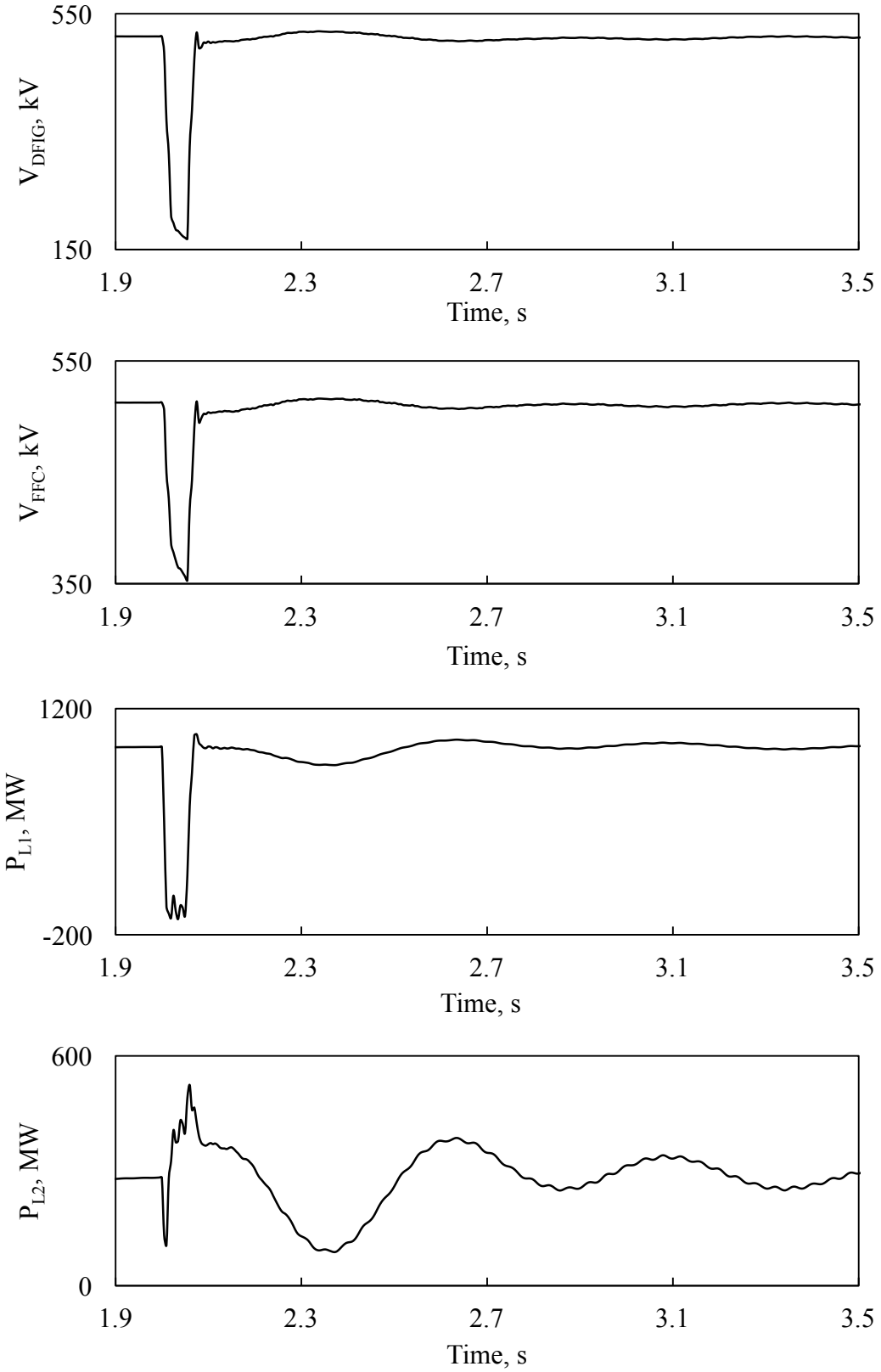

Figure 2.9: Continued.

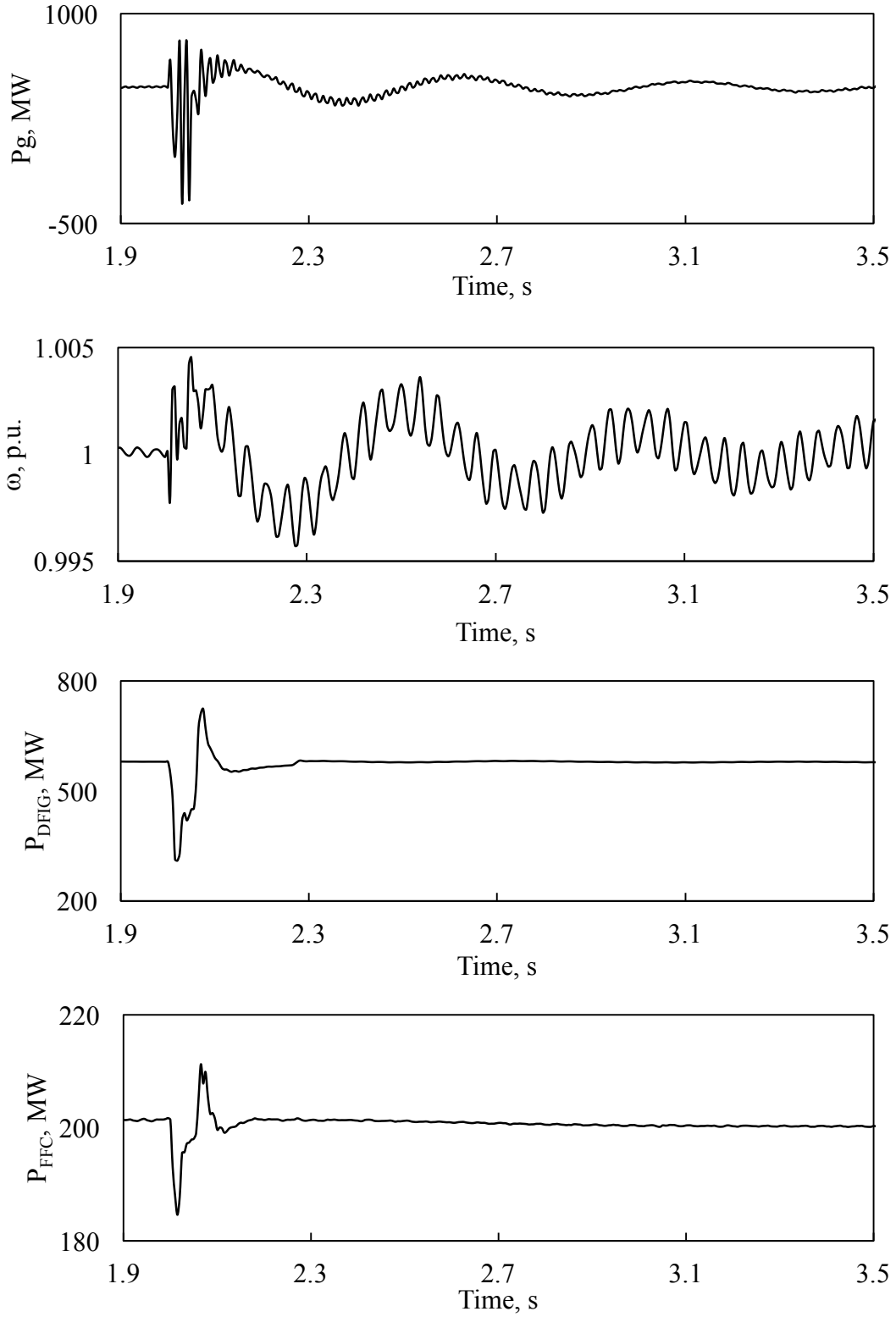

Figure 2.10: Transient time response of generator active power and speed, DFIG- and FFC-based wind farm active powers and terminal voltages and real power flow on L_1 and L_2 during and after clearing a three-cycle, line-to-line fault at F_1.

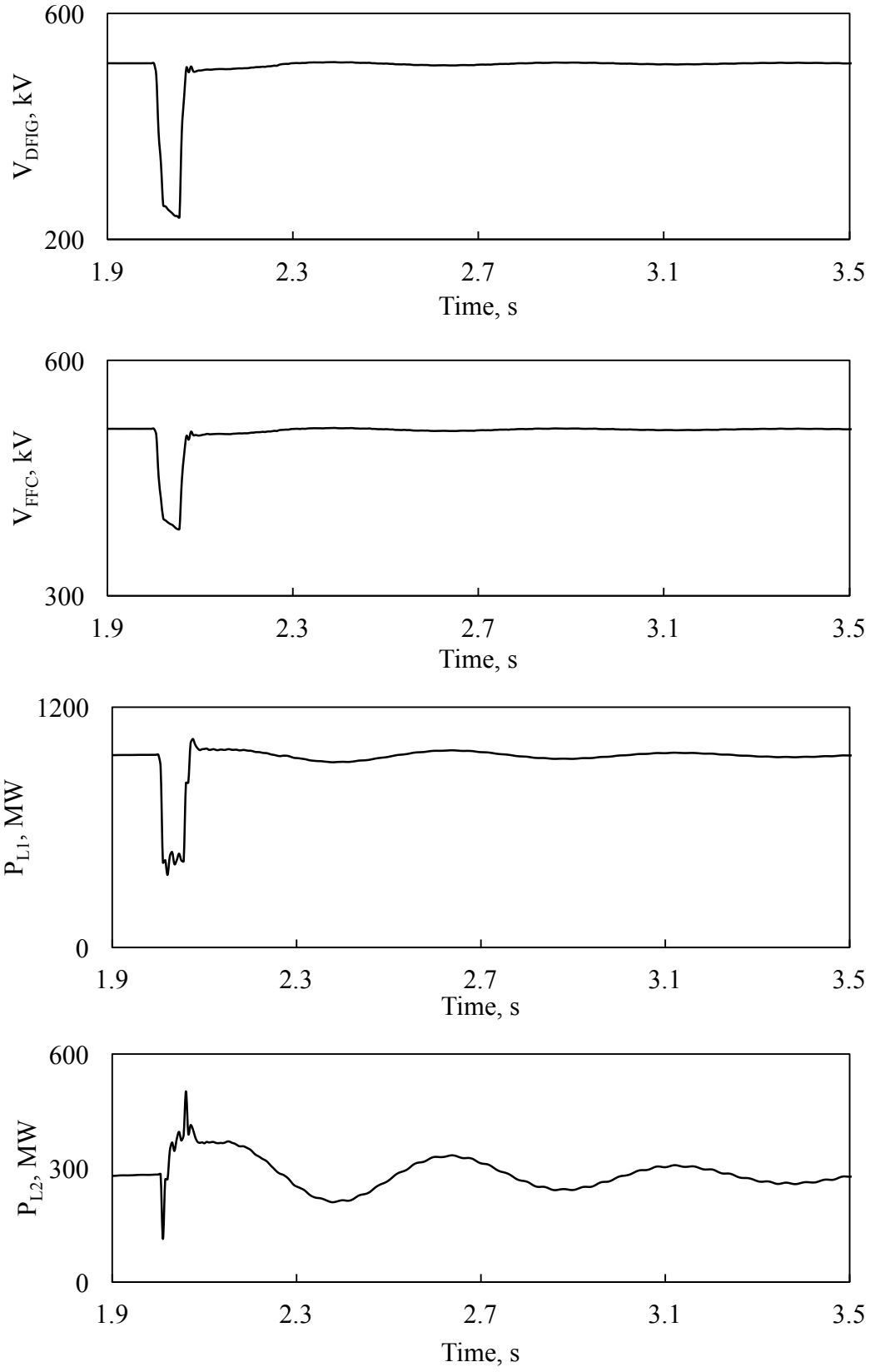

Figure 2.10: Continued.

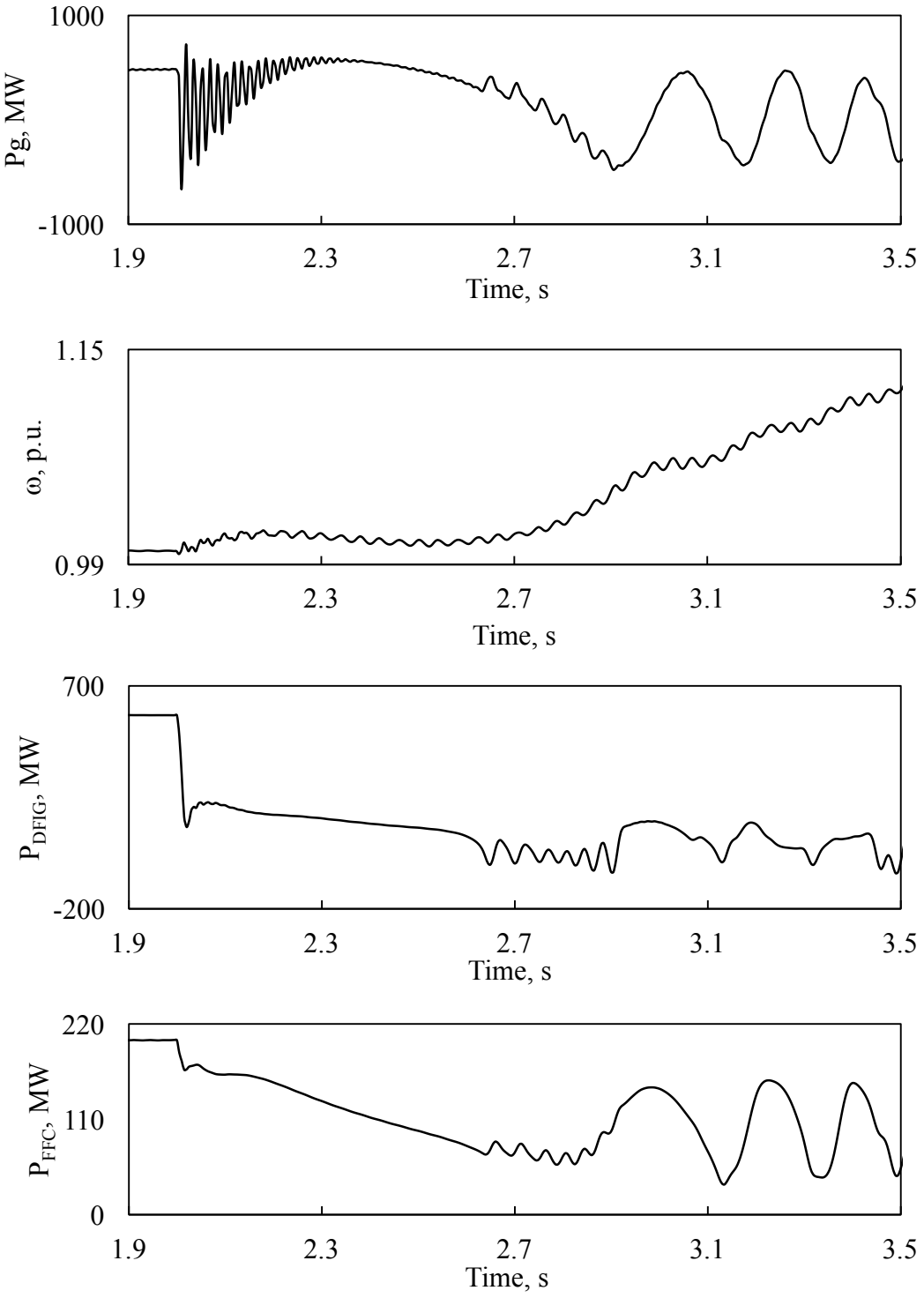

Figure 2.11: Transient time response of generator active power and speed, DFIG- and FFC-based wind farm active powers and terminal voltages and real power flow on L_1 and L_2 during a sustained three-phase fault at F_1.

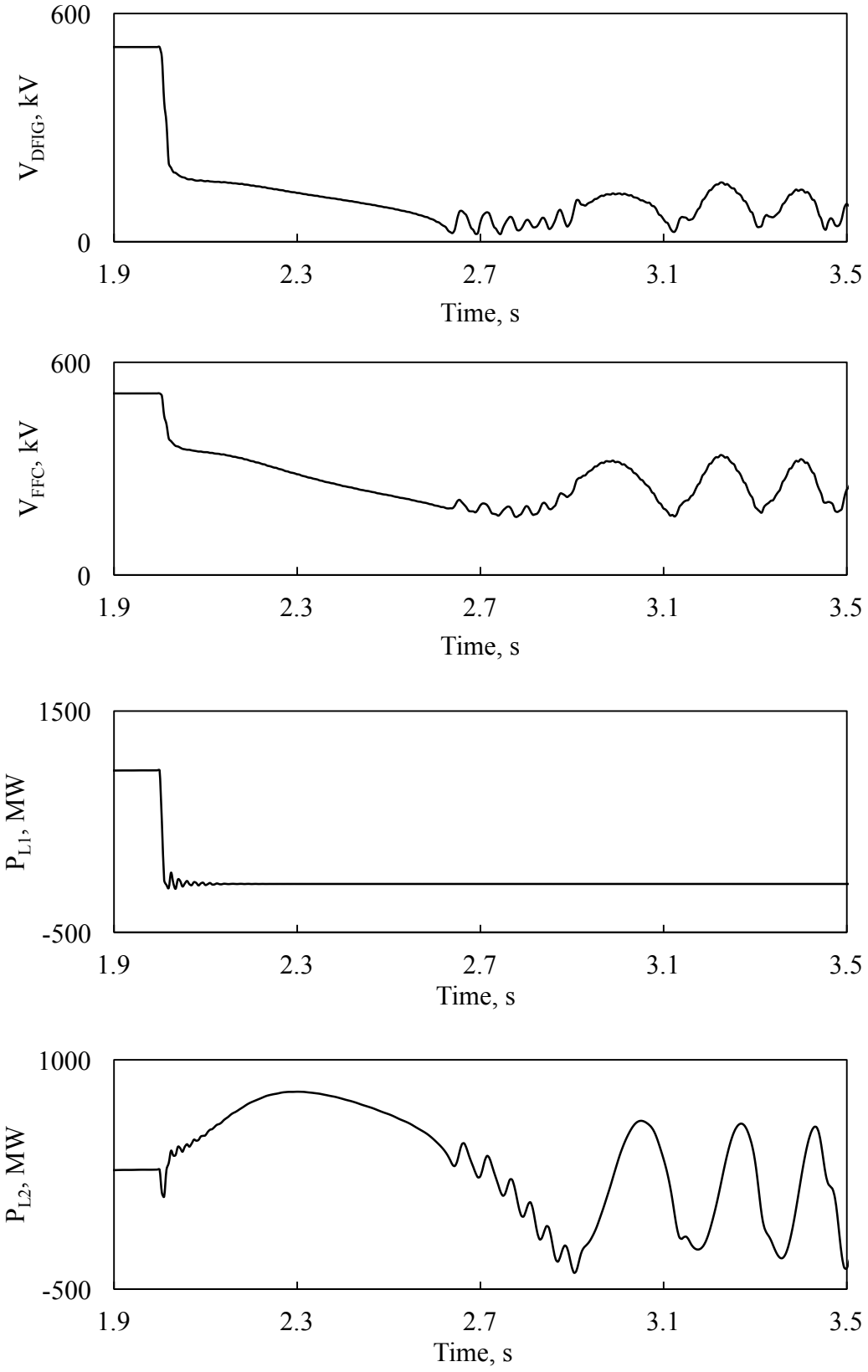

Figure 2.11: Continued.

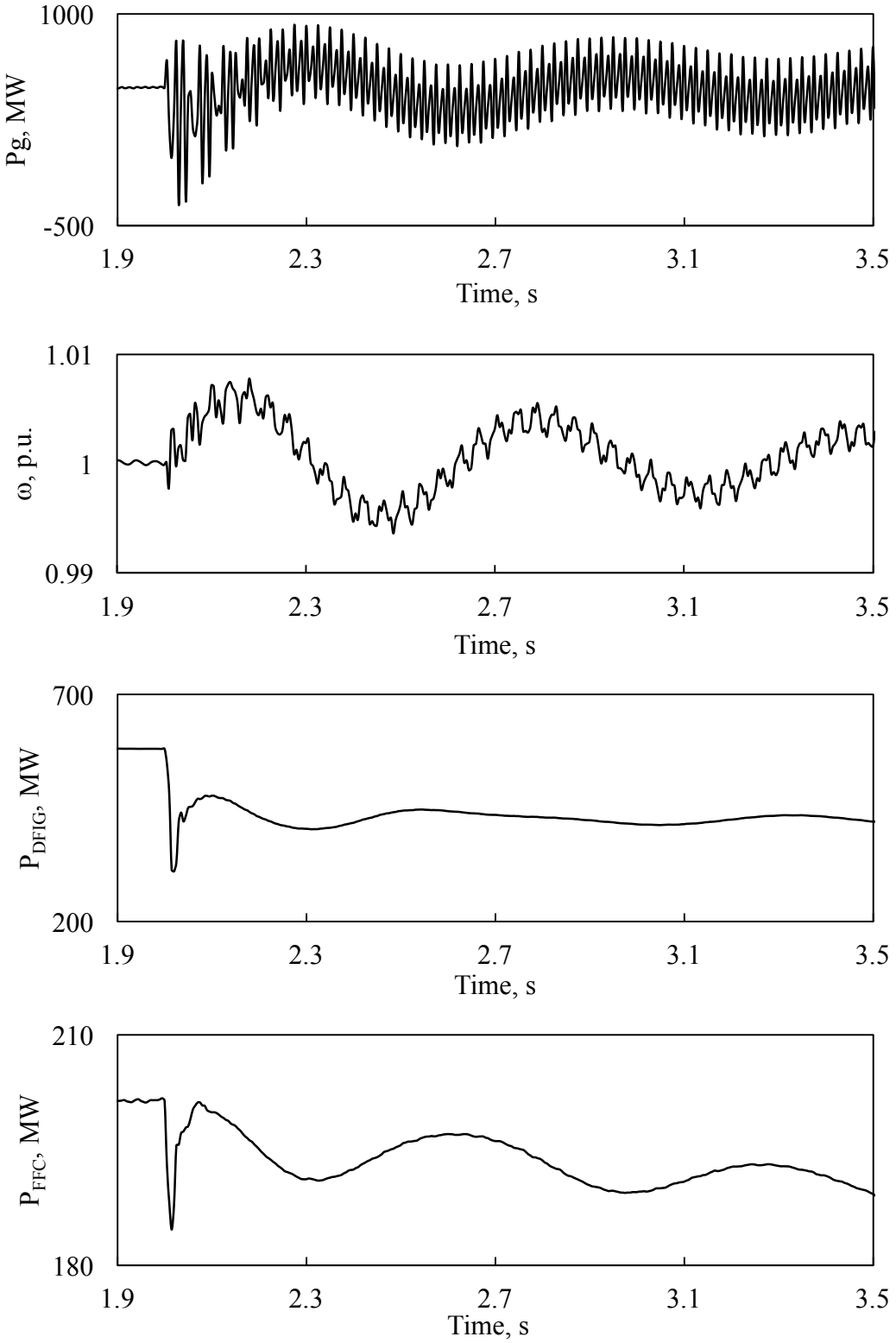

Figure 2.12: Transient time response of generator active power and speed, DFIG- and FFC-based wind farm active powers and terminal voltages and real power flow on L_1 and L_2 during a sustained line-to-line fault at F_1.

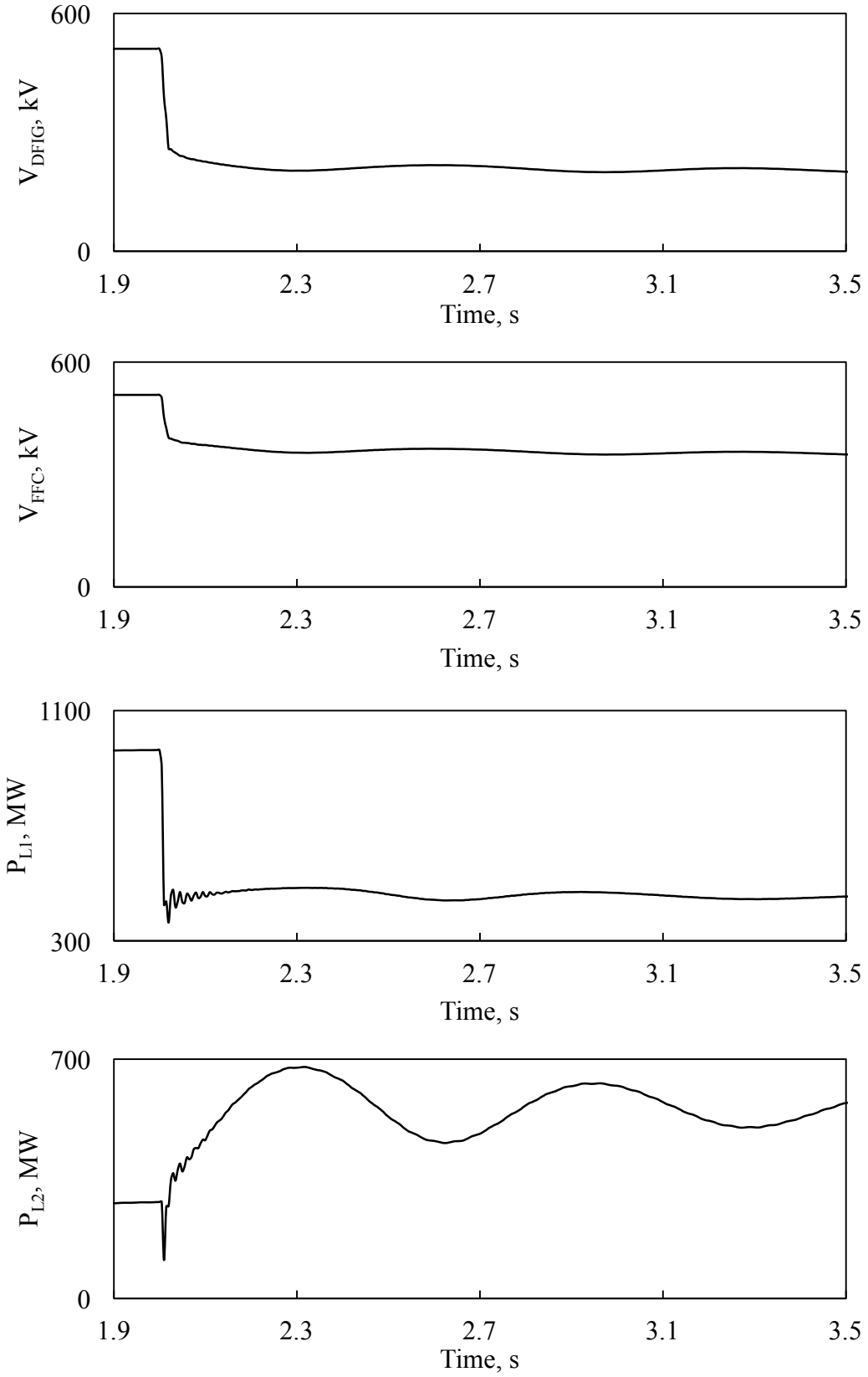

Figure 2.12: Continued.

The following observations can be made from examining Figures 2.11 and 2.12 (unsuccessful fault clearings):

- In the case of a three-phase fault, the system loses its stability as the generator speed is increasing and its real power exhibits a low-frequency sustained oscillations.
- In the case of a line-to-line fault, the generator real power also exhibits sustained oscillations with a frequency of 120Hz.

2.5 Summary

This chapter introduces the system used for the studies reported in this thesis and presents the mathematical models of its various components. A digital time-domain simulations of a case study of the system during three-phase and line-to-line faults is presented to validate the developed model, and some observations are noted. As it has been shown in the study case that a failure in clearing a fault due to a malfunction in the transmission line relaying may result in system instability, a generator phase backup protection is a necessity.

3. IMPACTS OF DFIG- AND FFC- BASED WIND FARMS ON GENERATOR DISTANCE PHASE BACKUP PROTECTION AND THE COORDINATION BETWEEN RELAY (21) AND THE GENERATOR CAPABILITY CURVES

3.1 Introduction

In this chapter, investigations are carried out to explore the effect of the DFIG- and FFC-based wind farms on the performance of generator distance phase backup protection (Relay (21)). In this context, comparative studies between the relay performance with and without the presence of the wind farms during line-to-line and three-phase faults at different locations are presented. The investigations extend also to examine the impact of the wind farms on the coordination between Relay (21) and the generator capability curves.

3.2 Generator Capability Curves

The need to coordinate generator protection with generator control and load capability requires the knowledge of generator steady-state and dynamic characteristics. The nameplate ratings of a generator define only one limiting point of operation for the machine. It is logical to assume that a reduction in the MVAR output would allow some increase in the MW output and that a reduction in the MW would allow a higher MVAR output. These allowable variations are defined by the generator capability limits, which are usually provided by the manufacturer [6], [21]. These limits, when plotted in the P (MW) – Q (MVAR) plane, form the Generator Capability Curve (GCC). Figure 3.1 shows the capability curves for turbogenerators and hydrogenerators. The operating terminal voltage range allowed by standards is 95% – 105% of rated voltage, but generator capability curves are normally plotted for the rated terminal voltage. The capability curve contains two or more boundaries for MW and MVAR limits.

The capability curve of a turbogenerator (cylindrical rotor synchronous machine) is a composite of three distinct limits (A-B, B-D and D-E). The upper boundary of the curve (A-B) is the rotor field thermal limit specified at a DC current rating. This boundary is often approximated by an arc with a center at a value equal to the short circuit ratio (SCR) in per unit on the negative y axis (the MVAR axis) and a radius of E_f/X_d where E_f is the internal or rotor

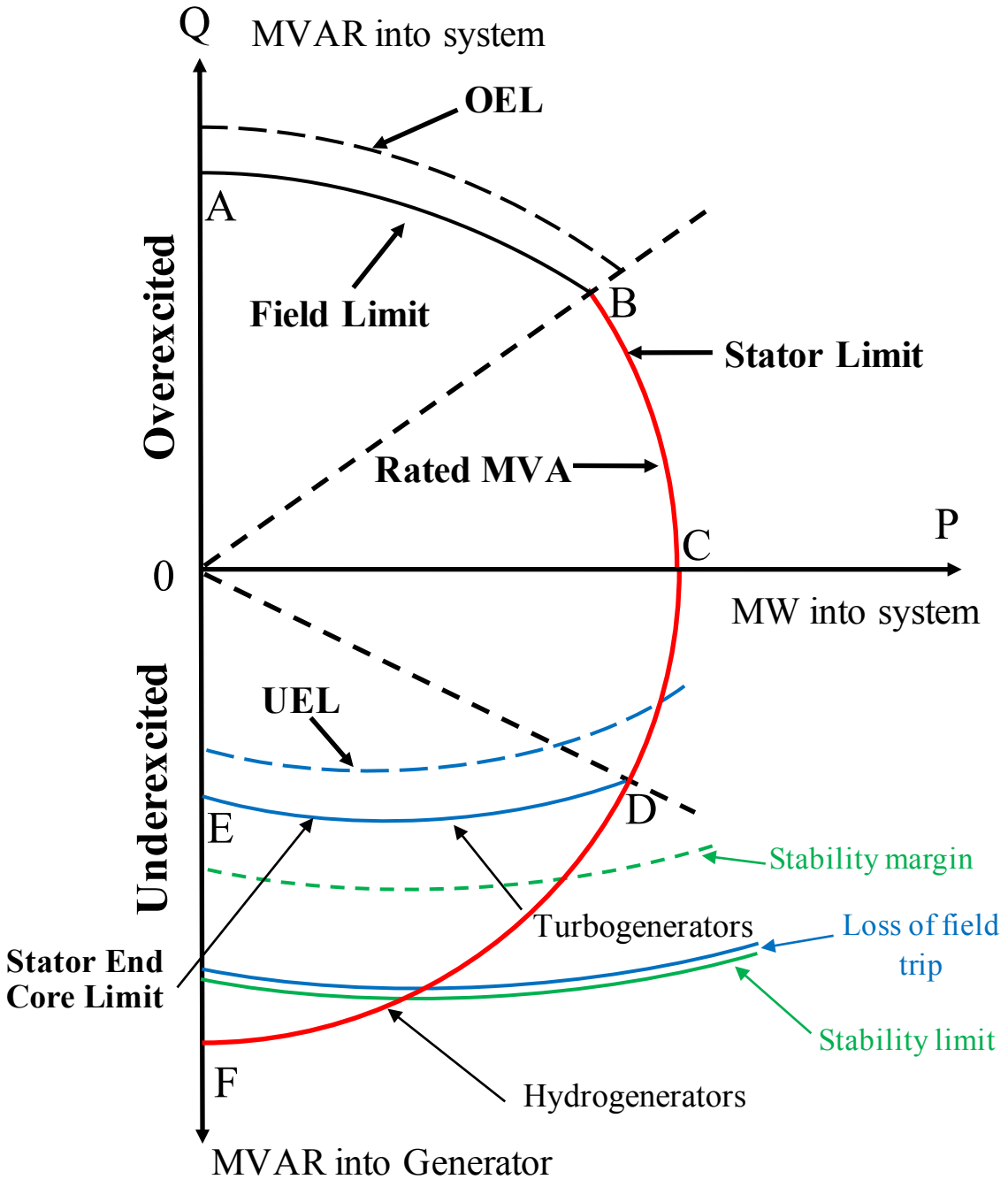

Figure 3.1: Generator capability curves for turbogenerators and hydrogenerators

field excitation voltage given that the synchronous generator terminal voltage is one per unit. The right hand boundary (B-D) is the synchronous generator stator current limit. The center of the arc defining this limit is the origin. The curve (A-C) is termed as the generator steady-state overexcited capability (GOEC) limit which ensures the operation of the generator within the

overexcited region. The lower boundary (D-E) is the end iron heating limit (heating in the end laminations of the stator core) which occurs during leading power factor, underexcited operating conditions. The curve (C-E) is termed as the generator steady-state underexcited capability (GUEC) limit which guides the operation of the generator within the underexcited region.

The capability curve for a hydrogenerator is different from that of a turbogenerator. Hydro units are of salient-pole construction and have negligible end core losses. Thus, their capability curves have only two distinct limits. The field circuit imposed lagging Vars limit from A to B and the stator winding current limit which extends as a continuous arc from B to F. Therefore, the leading VAR limit is determined by the current rating of the stator winding. Similarly, the boundary (A-C) represents the generator steady-state overexcited capability (GOEC) limit while the boundary (C-F) represents the generator steady-state underexcited capability (GUEC) limit.

The utility application engineer will design some additional limitations in both the overexcited and underexcited regions for generator control purposes. The overexcitation limiter (OEL) limits the generator operation in the overexcited region within generator capability curve. Some users set the OEL just under the machine capability curve, while others set it just over the machine capability as shown in Figure 3.1 to allow full machine capability.

In the underexcited region, every machine will have a steady-state stability limit which is a function of both the synchronous generator characteristics and the stiffness of the electrical system to which the machine is paralleled. A loss-of-field relay can be set to trip the machine before this limit is exceeded. An acceptable margin is computed in order to make an underexcitation alarm relay setting and additional margin is provided in order to set either a minimum excitation limiter (MEL) or underexcitation reactive ampere limiter (UEL) in the automatic voltage regulator.

3.2.1 Coordination between Relay (21) and GOEC

Figure 3.1 shows that the generator steady-state overexcited capability (GOEC) limit is plotted on a P-Q (MW - MVAR) plane (curve ABC). On the other hand, the generator distance phase backup protection relay measures impedance and its characteristic is typically displayed on an R – X (ohm) plane. To coordinate the GOEC limit with Relay (21) characteristic, it is necessary to convert the GOEC limit to an R - X plot. Figure 3.2 illustrates this conversion

where the current transformer (CT) and the voltage transformer (VT) ratios (R_c/R_v) convert the primary ohms to the secondary side quantities that are set within the relay and the kV is the rated voltage of the generator [6], [27].

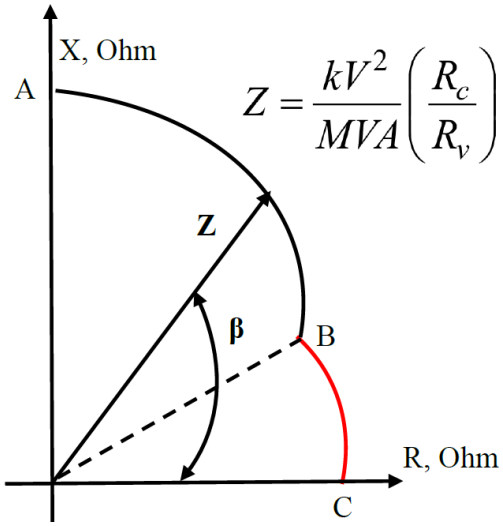

Figure 3.2: Transformation of a P-Q plot to an R-X plot.

3.3 Impedance Measured by Relay (21)

Different methods are applied in distance relays, but the goal is common, which is to measure the positive-sequence impedance from the relay to the fault. To get the phase fault protection functioning, phase elements (A-B, B-C, C-A) are put into utilization. Figure 3.3 shows a sample system illustrating how Relay (21) is configured. The system is made up of a no-load synchronous generator which connects to a radial transmission line through a step up transformer. In the following analysis, X'_d is used as the reactance of synchronous machine, E is defined as the internal e.m.f., X_{g2} is the synchronous machine negative-sequence reactance. Moreover, Z_{s1} and Z_{s2} are the positive- and negative-sequence phase impedances respectively, which are defined as

$$Z_{s1} = Z_{T1} + Z_{sl1} \tag{3.1}$$

$$Z_{s2} = Z_{T2} + Z_{sl2} \tag{3.2}$$

where the Z_T is the transformer impedance and the Z_{sl} is the transmission line impedance from bus A to the fault point.

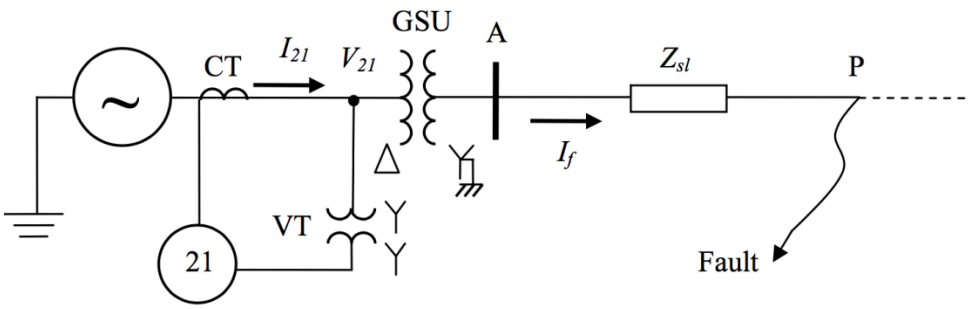

Figure 3.3: A single-line diagram of a synchronous generator connected to a radial transmission system.

To convert the sequential parameters to the phase parameters (for a phase sequence ABC) are following, where $a = 1\angle 120^\circ$

$$V_A = V_1 + V_2 + V_0 \tag{3.3}$$

$$V_B = a^2V_1 + aV_2 + V_0 \tag{3.4}$$

$$V_c = aV_1 + a^2V_2 + V_0 \tag{3.5}$$

$$I_A = I_1 + I_2 + I_0 \tag{3.6}$$

$$I_B = a^2I_1 + aI_2 + I_0 \tag{3.7}$$

$$I_c = aI_1 + a^2I_2 + I_0 \tag{3.8}$$

Under this conversion, the phase-to-phase voltages and currents can be retained from the equations above as following the equations

$$V_A - V_B = \sqrt{3}(V_1\angle 30^\circ + V_2\angle -30^\circ) \tag{3.9}$$

$$V_B - V_C = \sqrt{3}(V_1\angle 270^\circ + V_2\angle 90^\circ) \tag{3.10}$$

$$V_C - V_A = \sqrt{3}(V_1\angle 150^\circ + V_2\angle -150^\circ) \tag{3.11}$$

$$I_A - I_B = \sqrt{3}(I_1\angle 30^\circ + I_2\angle -30^\circ) \tag{3.12}$$

$$I_B - I_C = \sqrt{3}(I_1\angle 270^\circ + I_2\angle 90^\circ) \tag{3.13}$$

$$I_C - I_A = \sqrt{3}(I_1\angle 150^\circ + I_2\angle -150^\circ) \tag{3.14}$$

From the above equations, each phase distance element measures the impedance by the following equations

$$Z_{AB} = \frac{V_A - V_B}{I_A - I_B} \tag{3.15}$$

$$Z_{BC} = \frac{V_B - V_C}{I_B - I_C} \tag{3.16}$$

$$Z_{CA} = \frac{V_C - V_A}{I_C - I_A} \tag{3.17}$$

which implies the following if substitute Eqs. (3.9) to (3.12) into Eqs. (3.15) to (3.17)

$$Z_{AB} = \frac{V_1 \angle 30° + V_2 \angle -30°}{I_1 \angle 30° + I_2 \angle -30°} \tag{3.18}$$

$$Z_{BC} = \frac{V_1 \angle 270° + V_2 \angle 90°}{I_1 \angle 270° + I_2 \angle 90°} \tag{3.19}$$

$$Z_{CA} = \frac{V_1 \angle 150° + V_2 \angle -150°}{I_1 \angle 150° + I_2 \angle -150°} \tag{3.20}$$

1. Three-phase fault

Only positive-sequence voltage and current exist in the symmetrical fault. By substituting $V_2 = 0$ and $I_2 = 0$ into Eqs. (3.18) to (3.20), we can get

$$Z_{AB} = Z_{BC} = Z_{CA} = \frac{V_1}{I_1} \tag{3.21}$$

which results

$$Z_{AB} = Z_{BC} = Z_{CA} = Z_{s1} \tag{3.22}$$

The above equations indicate that each relay element sees the impedance of the positive-sequence impedance from the relay to the fault location.

2. Phase-to-phase fault

Figure 3.4 shows the connection between positive- and negative-sequence circuit, the positive- and negative-sequence voltage and current are

$$I_1 = -I_2 \tag{3.23}$$

$$V_1 = E - I_1 X'_d \tag{3.24}$$

$$V_2 = -I_2 X_{g2} \tag{3.25}$$

$$I_1 = \frac{E}{X'_d + X_{g2} + Z_{s1} + Z_{s2}} = \frac{E}{X'_d + X_{g2} + 2Z_{s1}} \tag{3.26}$$

which by substituting Eqs. (3.32) to (3.26) into Eqs. (3.18) to (3.20) can result

$$Z_{AB} = 2Z_{s1}\angle -60° + \sqrt{3}X_{g2}\angle -90° \tag{3.27}$$

$$Z_{BC} = Z_{s1} \tag{3.28}$$

$$Z_{CA} = 2Z_{s1}\angle 60° + \sqrt{3}X_{g2}\angle 90° \tag{3.29}$$

From the above Eqs. (3.27) to (3.29), we can conclude that only the respective element will see the correct impedance from the relay to the location, and the other two elements see the impedance with enlarged value and disordered angle.

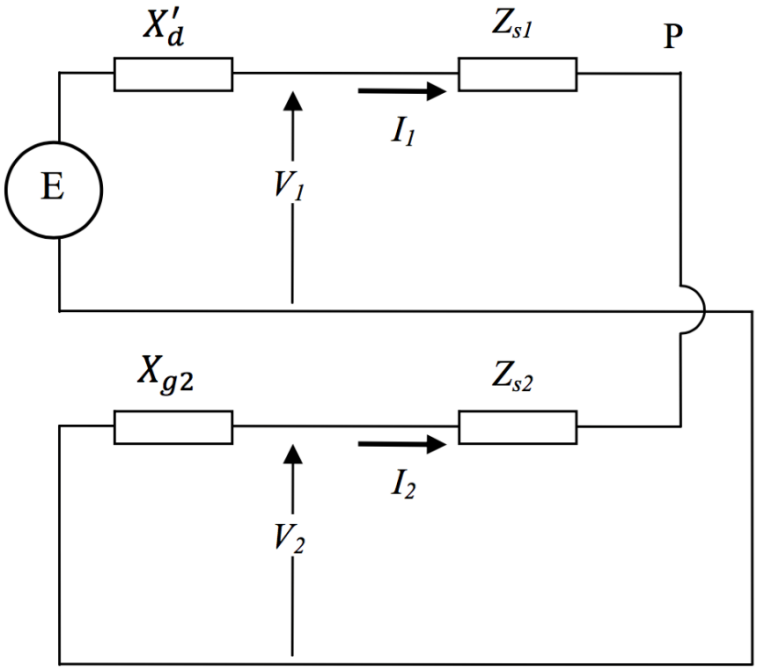

Figure 3.4: Connection of positive- and negative-sequence circuit of a phase-to-phase fault at fault location P.

3. Fault with infeed current

Practically, when a fault occurs, a transmission line will possibly carry infeed currents from interconnected transmission lines. Figure 3.5 illustrates the above example but with an infeed current I_{line1} and I_{line2}. Impedance seen by the relay becomes enlarged because the current measured by the relay is not the same value as the current flown on the transmission line.

With the infeed current, the voltage measure by the relay during a three phase fault is

$$V_{21} = Z_T I_{21} + Z_{sl} I_f \tag{3.30}$$

The impedance seen by the relay Z_{21} is

$$Z_{21} = \frac{V_{21}}{I_{21}} = \frac{Z_T I_{21} + Z_{sl} I_f}{I_{21}} = Z_T + Z_{sl} \frac{I_f}{I_{21}} \tag{3.31}$$

This equation indicates that the impedance measured by the relay with infeed current will be enlarged, which makes it necessary that the setting of the relay should be larger than the exact impedance from the relay to the protection point.

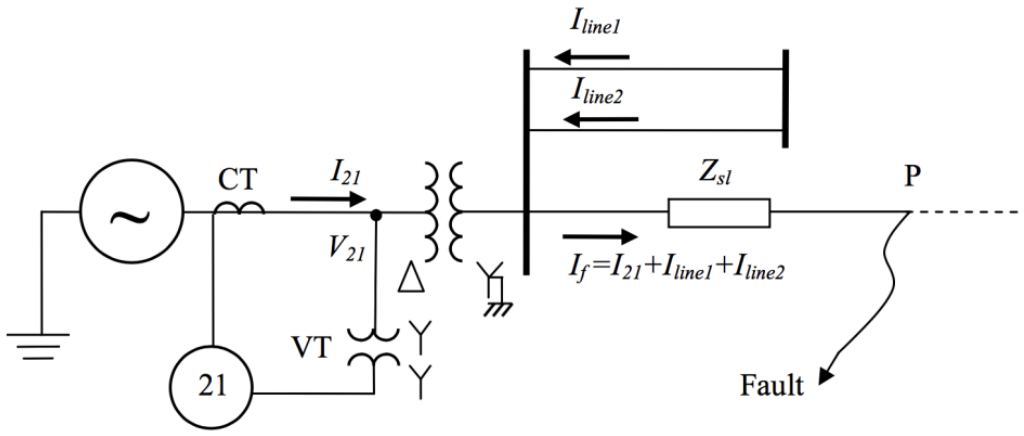

Figure 3.5: Impedance measured by relay with infeed currents.

3.4 Setting of Generator Distance Phase Backup Protection

The role of generator phase backup protection is to disconnect the generator during non-ground faults (line-to-line and three-phase) outside the generator protection zone that have not been cleared by other protective systems after an adequate time delay has elapsed [6]. Relay (21) elements are typically set at the smallest of the following three criteria [28]:

1. 120% of the longest transmission line with in-feeds. This setting is used when Relay (21) is required to function as a backup for the distance protection on the transmission system connected to the generator bus.

2. 50% to 67% of the generator load impedance (Z_{load}) at the rated power factor angle (RPFA) of the generator. This provides a 150% to 200% margin over the generator full load. This setting is used when the relay is required to protect the generator itself against any contingencies outside its short-timed overexcitation thermal capability.

3. The maximum setting of Relay (21) designated as Z_{GCC} is 80% to 90% of the generator load impedance at the maximum torque angle (MTA) of the relay impedance setting (typically 85°). This setting is the maximum setting that Relay (21) can reach if the generator is required to have one last extra margin of operation for its short-timed overexcitation thermal capability. Z_{GCC} is regarded as the last line of defense against any operating condition that might cause a severe damage to the generator main components. In other words, this setting is used to ensure that the coordination between Relay (21) and the generator steady-state overexcited thermal capabilities (GCC) is maintained at different generator loadings. In the investigations conducted in this paper, the value 90% is selected.

The calculated impedance settings for Relay (21) according to the above three criteria for the system under study are given in Table 3.1. Figure 3.6 shows two settings of criterion 2, Z_{GCC} and the generator capability curve GCC. The GCC is constructed at the generator rated voltage and converted from the P-Q plane to the R-X plane [21], [28].

Table 3.1: Relay (21) impedance settings

Criterion	Relay (21) Impedance	
1	$Z_{21} = 18.94\Omega$	
2	50% of Z_{load}	$Z_{21} = 12.51\Omega$
	60% of Z_{load}	$Z_{21} = 15.02\Omega$
	67% of Z_{load}	$Z_{21} = 16.77\Omega$
3	At 90°, $Z_{21} = 17.91\Omega$	

The time delay of Relay (21) element should be set to maintain a proper coordination with transmission line protection. In other words, Relay (21) time should be longer than that of transmission line backup protection (typically from 0.8 to 1 second). In the investigations

conducted in this thesis, a delay time of one second is used. It is worth noting also that during the investigations of this thesis, the circuit breaker corresponding to Relay (21) is blocked in order to give a presentation of the full impedance trajectory during all studied contingences.

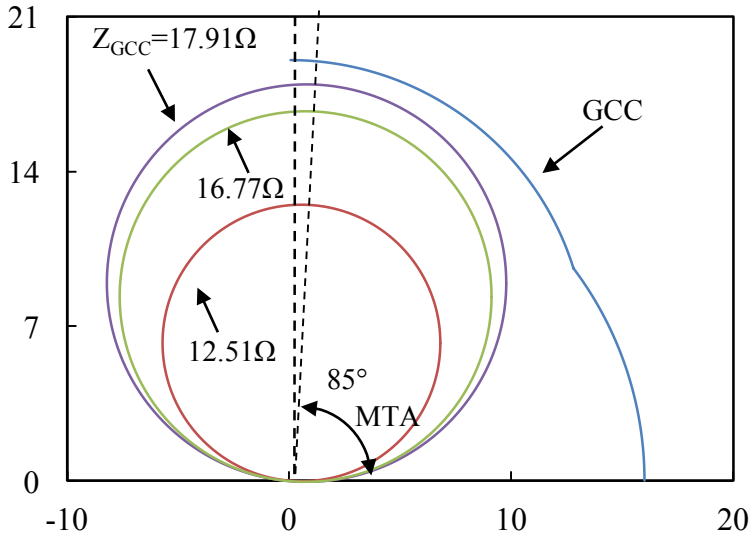

Figure 3.6: Two settings of criterion 2, Z_{GCC} and GCC

3.5 Setting Relay (21) According to 67% of the Generator Load Impedance at the Rated Power Factor Angle of the Generator

In order to investigate the impact of the two types of wind farms on the performance of Relay (21), the relay protective zone reach is set at 67% of the generator load impedance at the rated power factor angle of the generator ($Z_{Relay\ (21)} = Z_{21} = 16.77\ \Omega$) at MTA = 85°. This provides a 150% margin over the generator full load.

3.5.1 Performance of Relay (21) during a three-phase fault at F_1

Figure 3.7 illustrates Relay (21) tripping signal and measured impedance trajectory, the transient time responses of the generator active and reactive powers as well as the active and reactive power flows from bus 1 to bus M for the case of no wind farms in the system and 85% generator loading. At such a loading condition, the generator delivers 476 MW and 357 MVAR to systems S_1 and S_2 respectively. Figure 3.8 depicts the same responses for the case of DFIG- and FFC-based wind farms at buses M and N in addition to the wind farm real and reactive powers.

It can be seen from Figure 3.7 that in the absence of the wind farms, Relay (21) performs as expected and issues a tripping signal as the measured impedance trajectory penetrates and stays inside the relay zone. It is worth noting here that Relay (21) behaves in the same way for 65% and 75% generator loadings. In the presence of the wind farms, Figure 3.8 shows that the long fault duration of this relatively close-in fault causes the generator to lose its stability. The adverse effect of this instability extends to the DFIG- and FFC-based wind farms. The generator out of step protection would trip the generator before Relay (21) takes any action.

The effect of the generator loading on the performance of Relay (21) in the presence of the wind farms is examined at two other generator loadings, namely 65% and 75% of the rated power at rated power factor. However, unlike the 85% loading condition, at 65% and 75% generator loading conditions, there is insignificant impact of the wind farms on the performance of Relay (21).

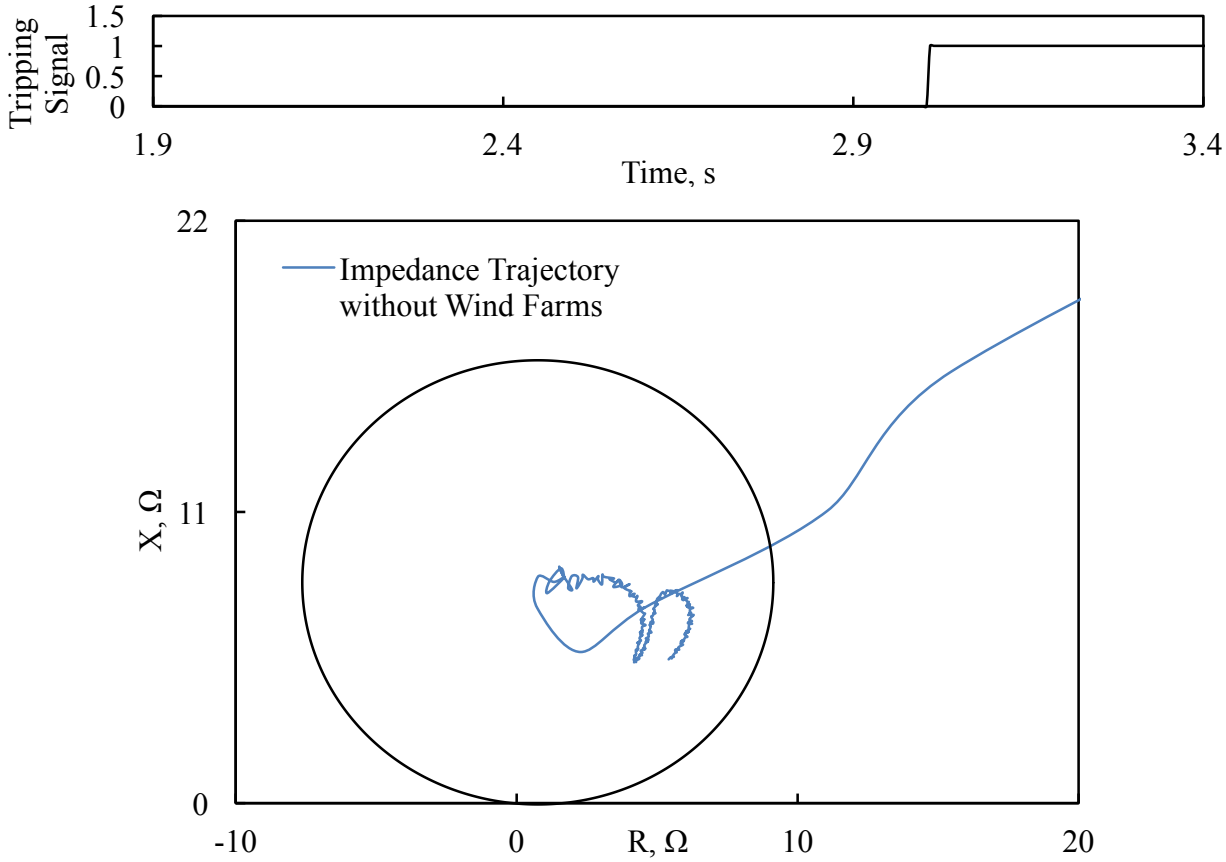

Figure 3.7: Relay (21) tripping signal, measured impedance trajectory, transient time responses of generator active and reactive powers, active and reactive power flows from bus 1 to bus M during a three-phase fault at F_1 (no wind farm in the system, generator loading is 85%).

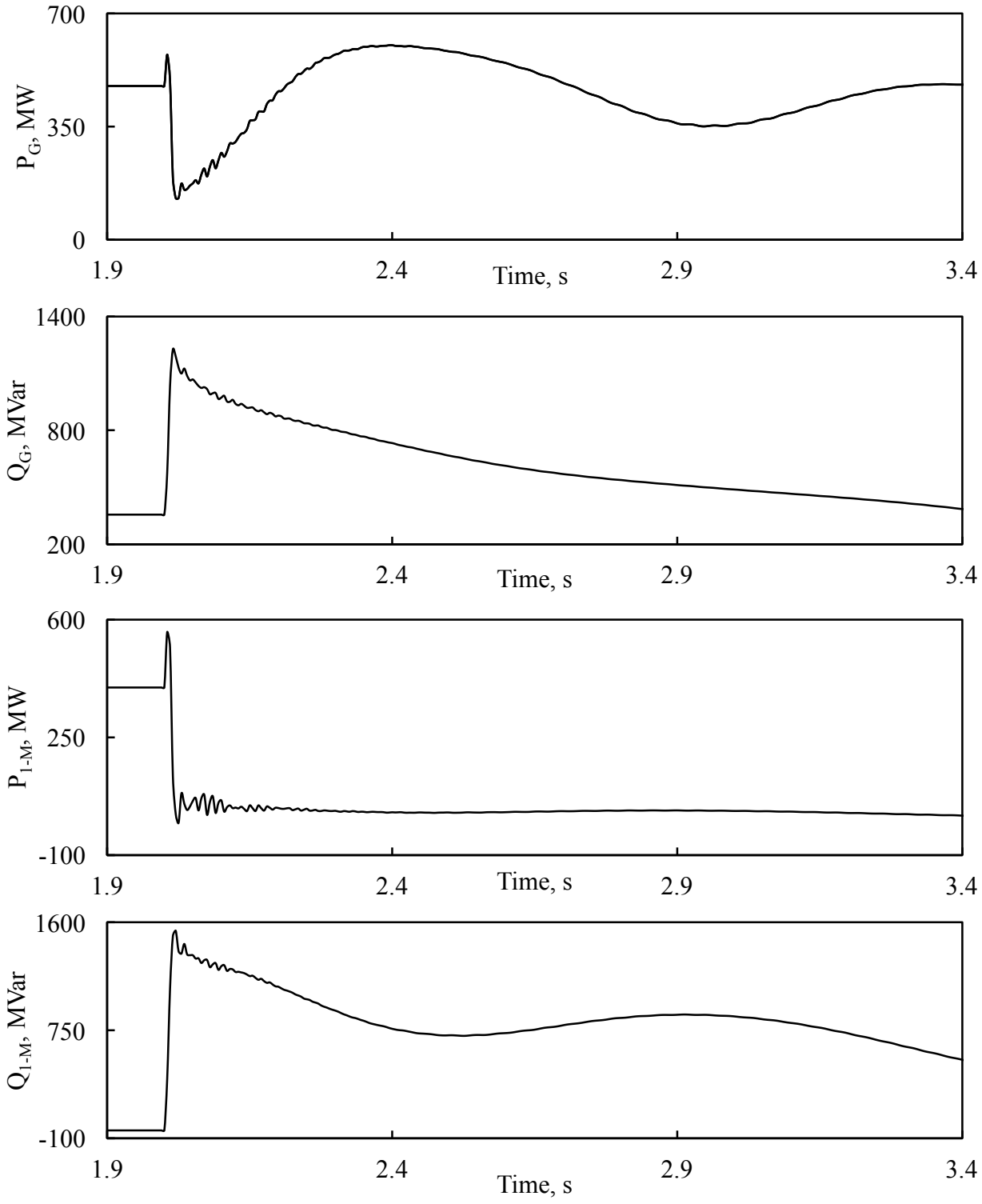

Figure 3.7: Continued.

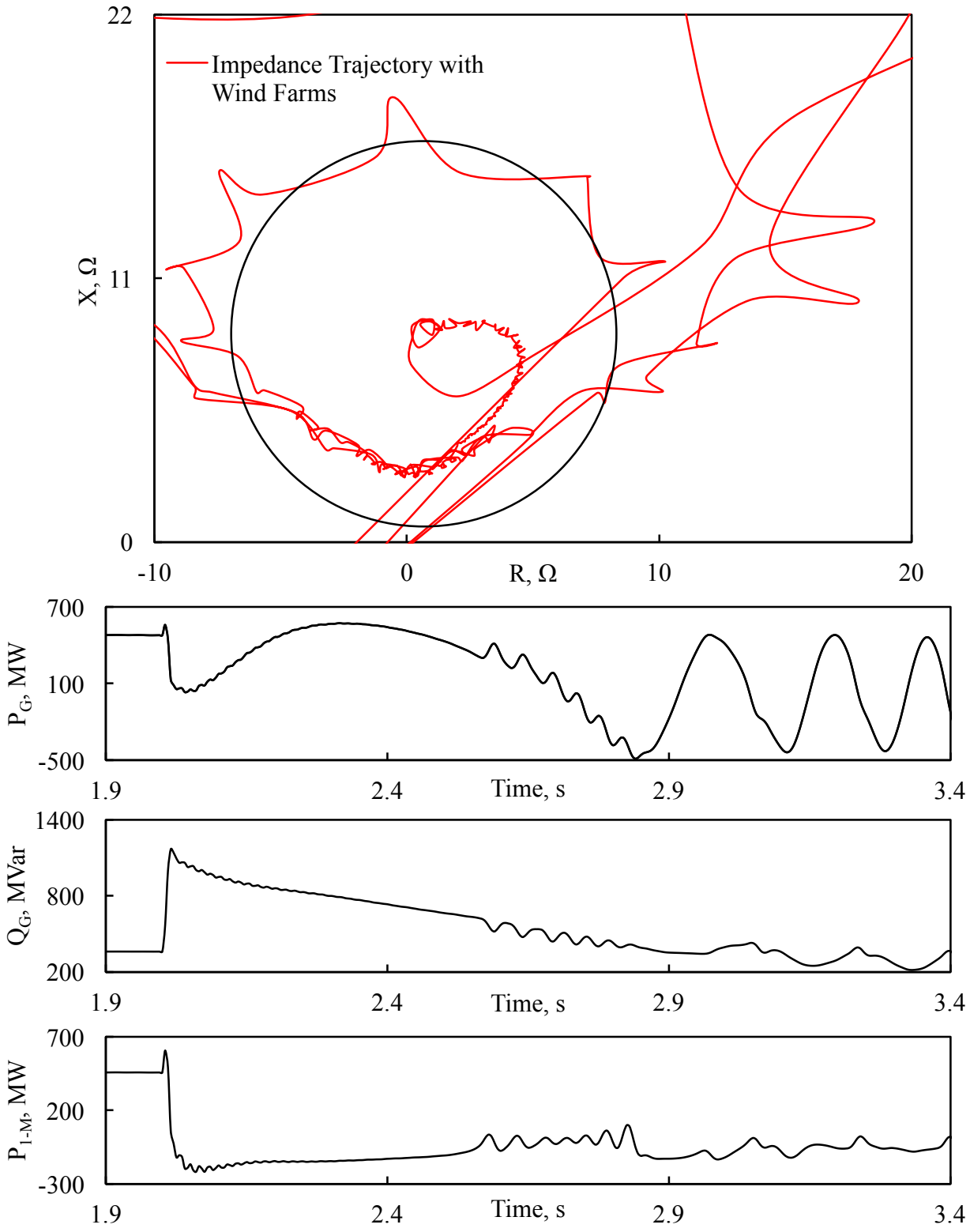

Figure 3.8: Relay (21) measured impedance trajectory, transient time responses of generator active and reactive powers, active and reactive power flows from bus 1 to bus M, DFIG- and FFC-based wind farm active and reactive powers during a three-phase fault at F_1 (generator loading is 85%).

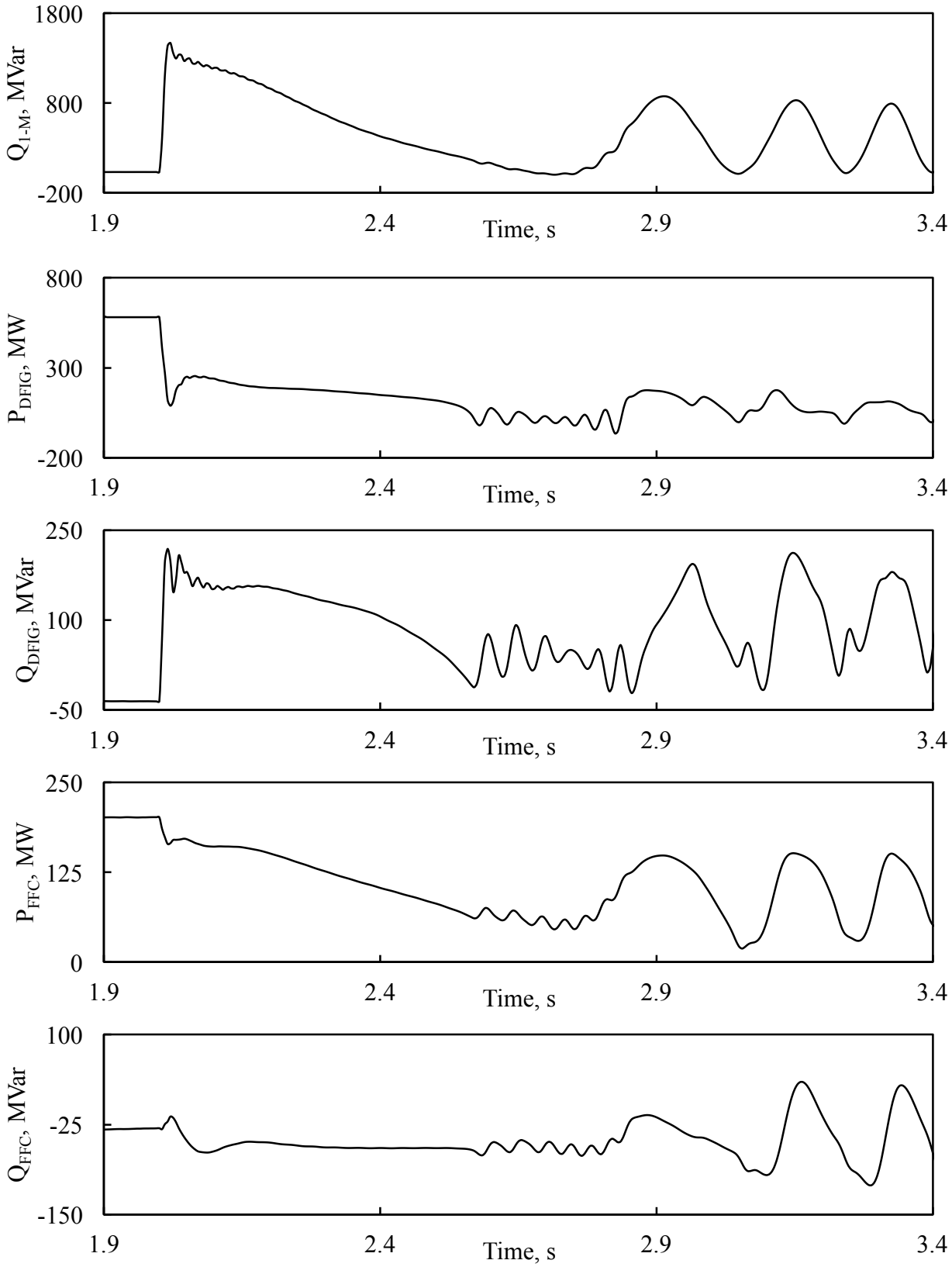

Figure 3.8: Continued.

3.5.2 Performance of Relay (21) during a line-to-line fault at F_1

Figure 3.9 illustrates Relay (21) tripping signal, the transient time responses of the generator active and reactive powers as well as the active and reactive power flows from bus 1 to bus M for the case of no wind farms in the system and 85% generator loading. Figure 3.10 depicts the same responses for the case of DFIG- and FFC-based wind farms at buses M and N in addition to the wind farm real and reactive powers and Relay (21) measured impedance trajectories. Unlike the case of the three-phase fault at F_1, the presence of the wind farms does not cause Relay (21) to misoperate as shown in Figures 3.9 and 3.10. However, a noticeable difference between the measured impedance trajectories can be seen. It is worth noting here again that Relay (21) behaves in the same way for 65% and 75% generator loadings.

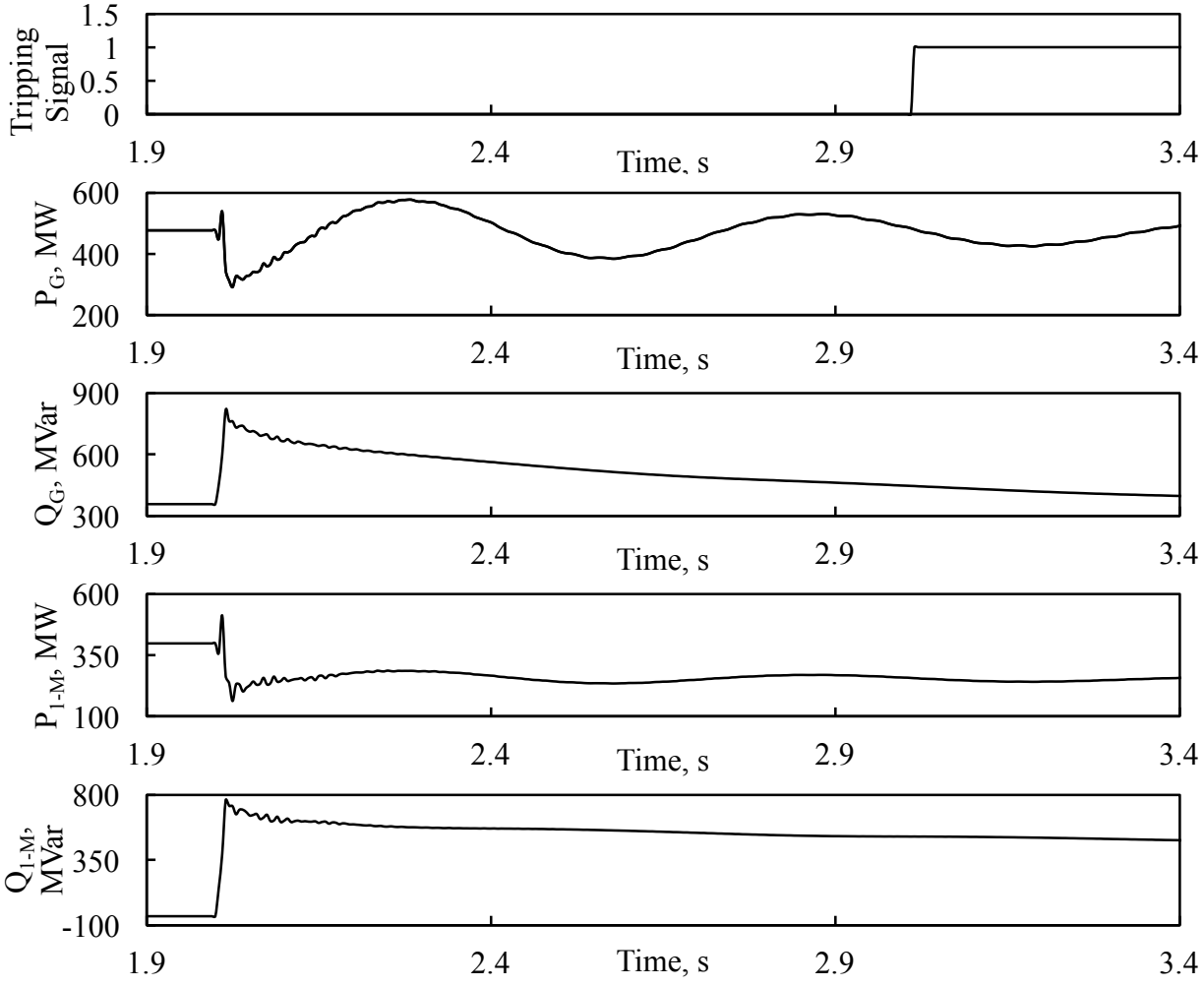

Figure 3.9: Relay (21) tripping signal, transient time responses of generator active and reactive powers, active and reactive power flows from bus 1 to bus M during a line-to-line fault at F_1 (no wind farm in the system, generator loading is 85%).

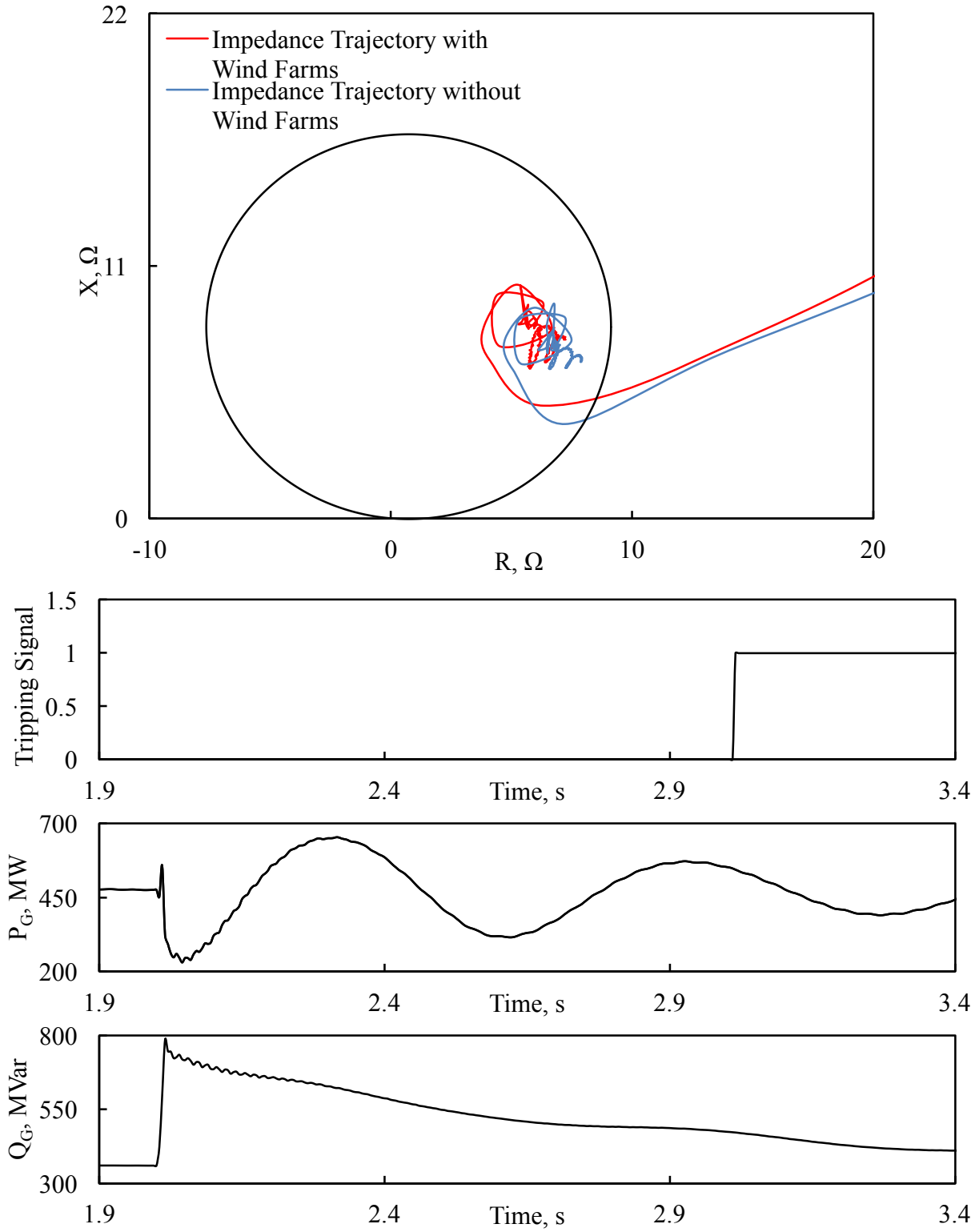

Figure 3.10: Relay (21) measured impedance trajectory and its tripping signal, transient time responses of generator active and reactive powers, active and reactive power flows from bus 1 to bus M, DFIG- and FFC-based wind farm active and reactive powers during a line-to-line fault at F_1 (generator loading is 85%).

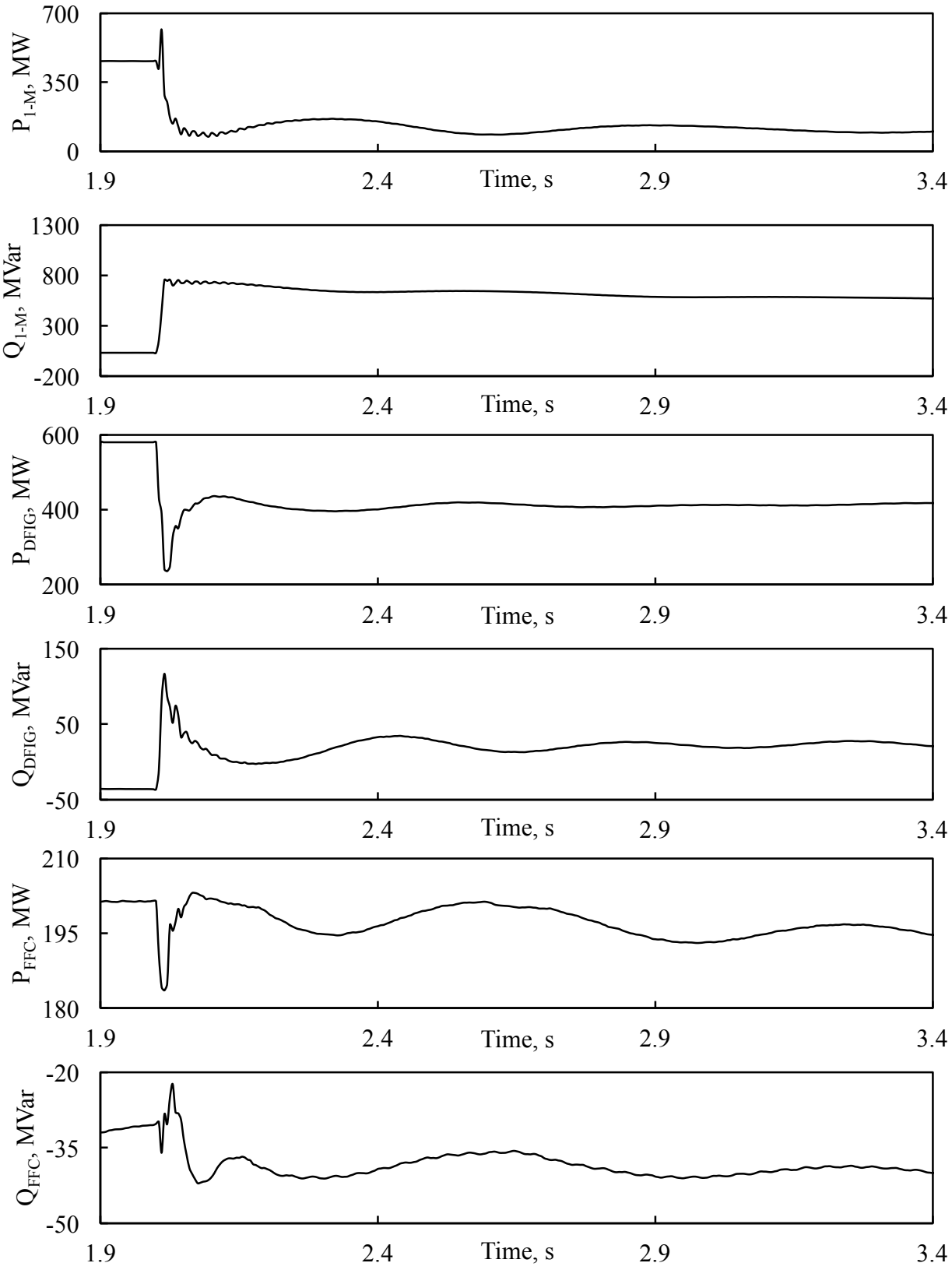

Figure 3.10: Continued.

3.5.3 Performance of Relay (21) during a three-phase fault at F_2

Figure 3.11 illustrates Relay (21) tripping signal, the transient time responses of the generator active and reactive powers as well as the active and reactive power flows from bus 1 to bus M for the case of no wind farms in the system and 85% generator loading. Figure 3.12 depicts the same responses for the case of DFIG- and FFC-based wind farms at buses M and N in addition to Relay (21) measured impedance trajectories and the wind farm real and reactive powers.

In response to the sudden system voltage drops caused by the high reactive power requirement due to the fault, the generator field current increases and results in an increase in the generator reactive power output (QG). The occurrence of the fault activates the DFIG grid- and rotor-side converters protection system that causes the crowbar to isolate the converters. As a result, the DFIG wind turbines operate as induction generators and the wind farm starts to absorb a large amount of reactive power from the system as shown in Figure 3.12. The increase in the reactive power flow from bus 1 to bus M is also noticeable in Figure 3.12. It can also be seen from the figure that there is also reactive power consumption by the FFC-based wind farm during the fault.

The performance of Relay (21) during the fault can be evaluated by examining its tripping signal and measured impedance trajectories depicted in Figure 3.12 in the absence and presence of the wind farms. It can be seen from this figure that, in the case of no wind farms, the impedance trajectory penetrates and stays inside Relay (21) zone for enough time for the relay to issue a trip signal. To the contrary, the presence of the wind farms causes the impedance trajectory to enter and leave the relay zone in a short time, not enough for the relay to detect the fault. In other words, the presence of the wind farms causes Relay (21) to under-reach. It is worth noting here that the same behavior was observed for 65% and 75% generator loadings.

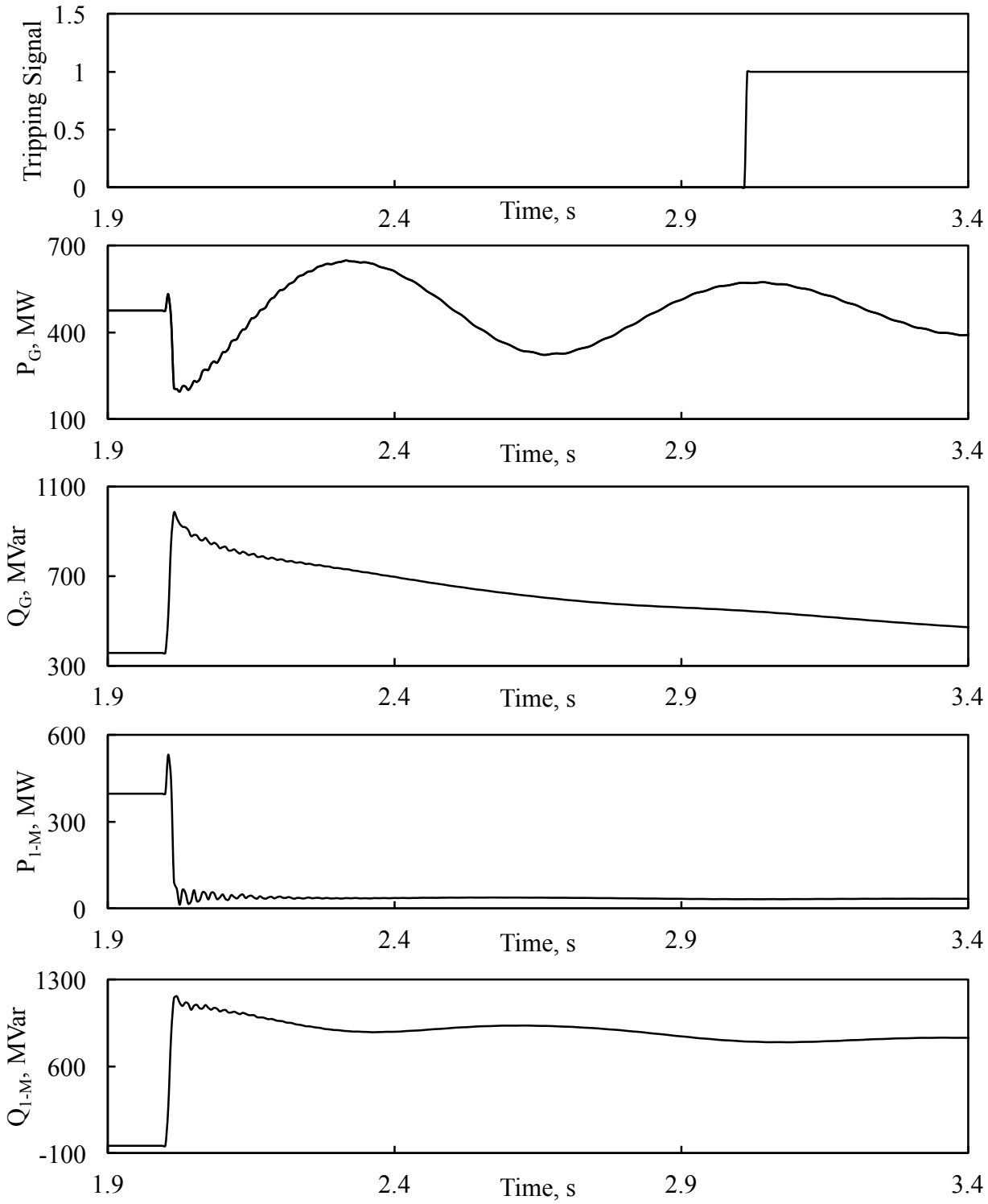

Figure 3.11: Relay (21) tripping signal, transient time responses of generator active and reactive powers, active and reactive power flows from bus 1 to bus M during a three-phase fault at F_2 (no wind farm in the system, generator loading is 85%).

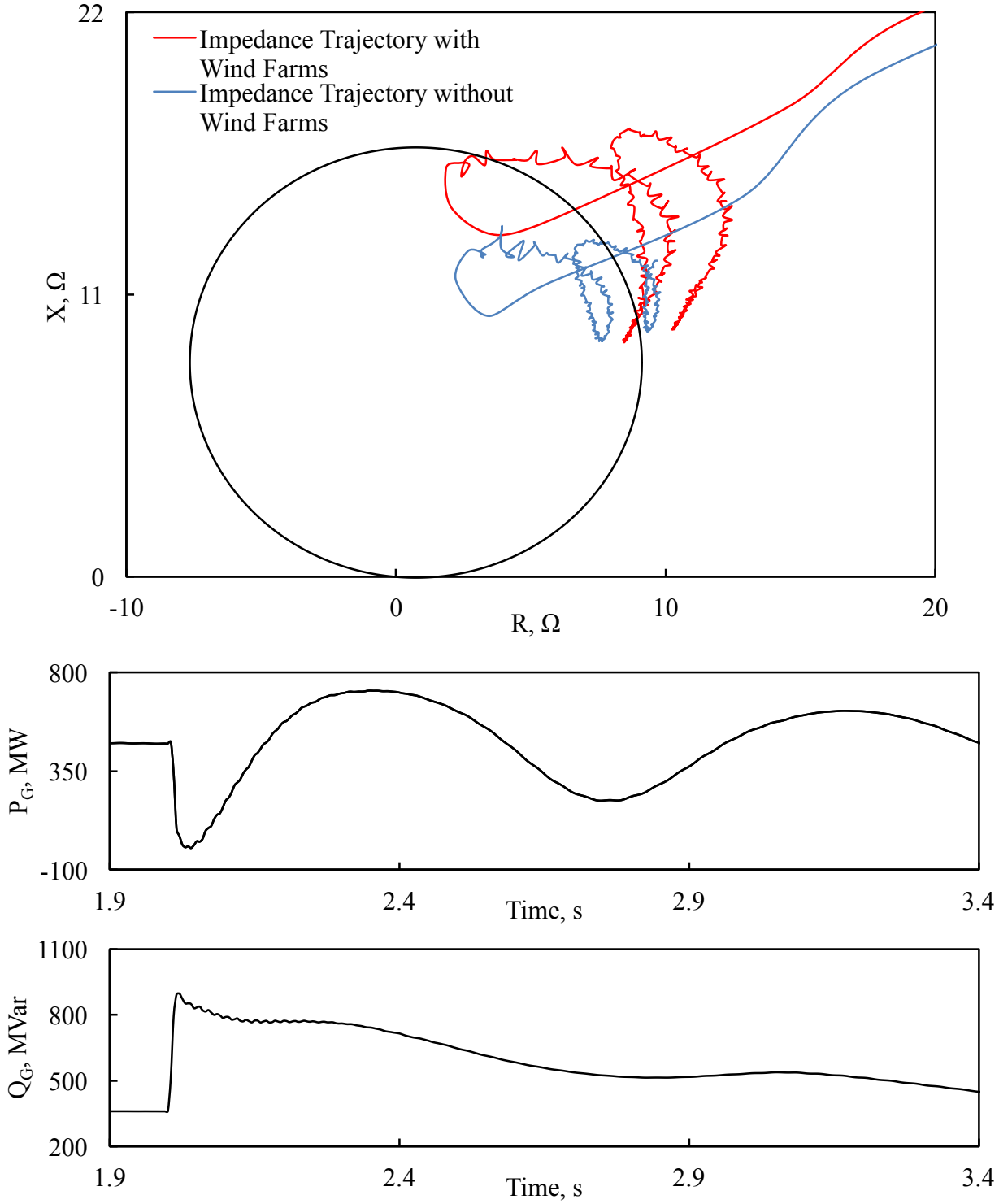

Figure 3.12: Relay (21) measured impedance trajectory, transient time responses of generator active and reactive powers, active and reactive power flows from bus 1 to bus M, DFIG- and FFC-based wind farm active and reactive powers during a three-phase fault at F_2 (generator loading is 85%).

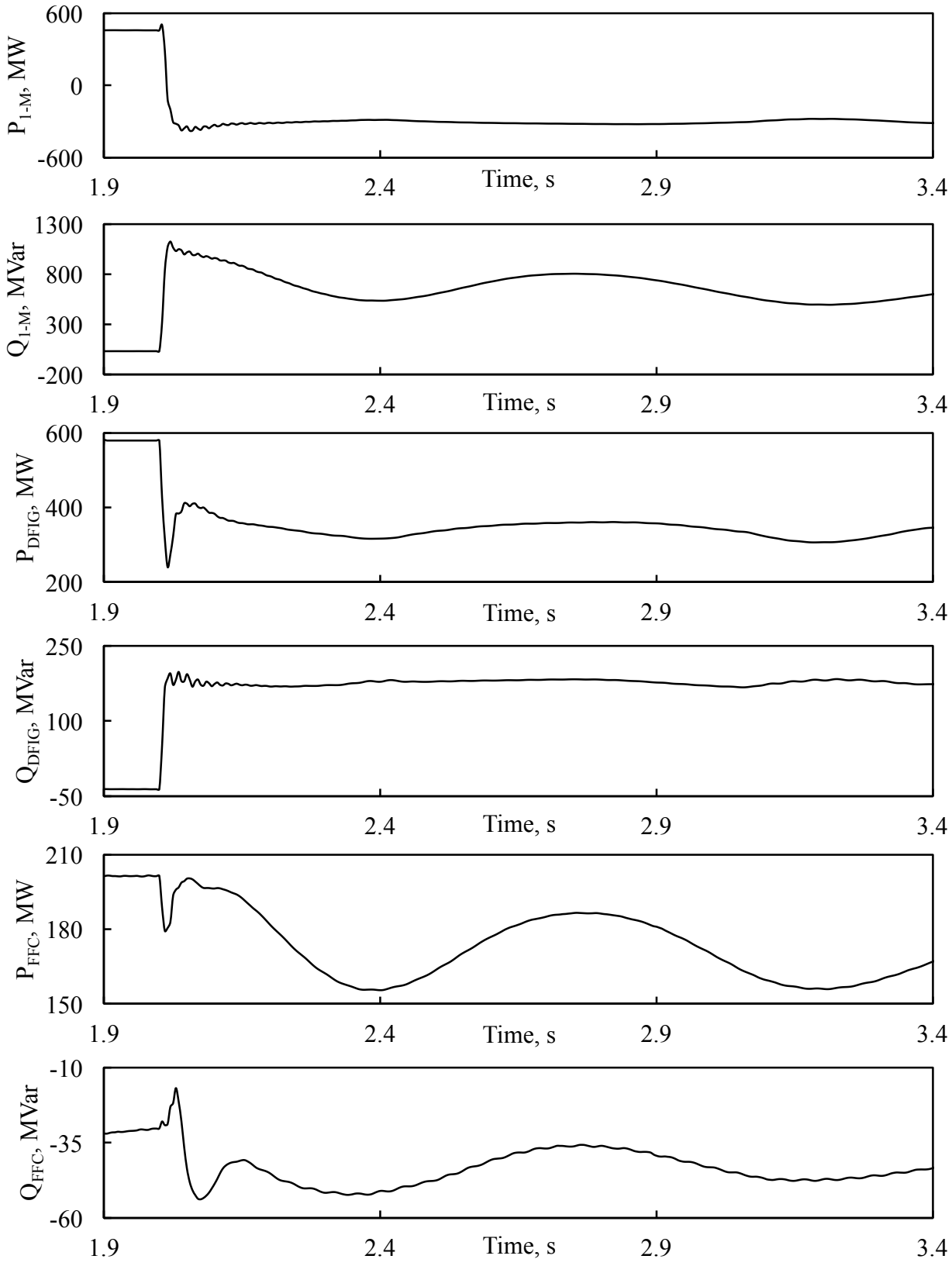

Figure 3.12: Continued.

3.5.4 Performance of Relay (21) during a line-to-line fault at F_2

Figure 3.13 illustrates Relay (21) tripping signal, the transient time responses of the generator active and reactive powers as well as the active and reactive power flows from bus 1 to bus M for the case of no wind farms in the system and 85% generator loading. Figure 3.14 depicts the same responses for the case of DFIG- and FFC-based wind farms at buses M and N in addition to the wind farm real and reactive powers and Relay (21) measured impedance trajectories. Unlike the case of the three-phase fault at F_2, the presence of the wind farms does not cause Relay (21) to misoperate as shown in Figure 3.14. However, a noticeable difference between the measured impedance trajectories can be seen. It is worth noting here again that Relay (21) behaves in the same way for 65% and 75% generator loadings.

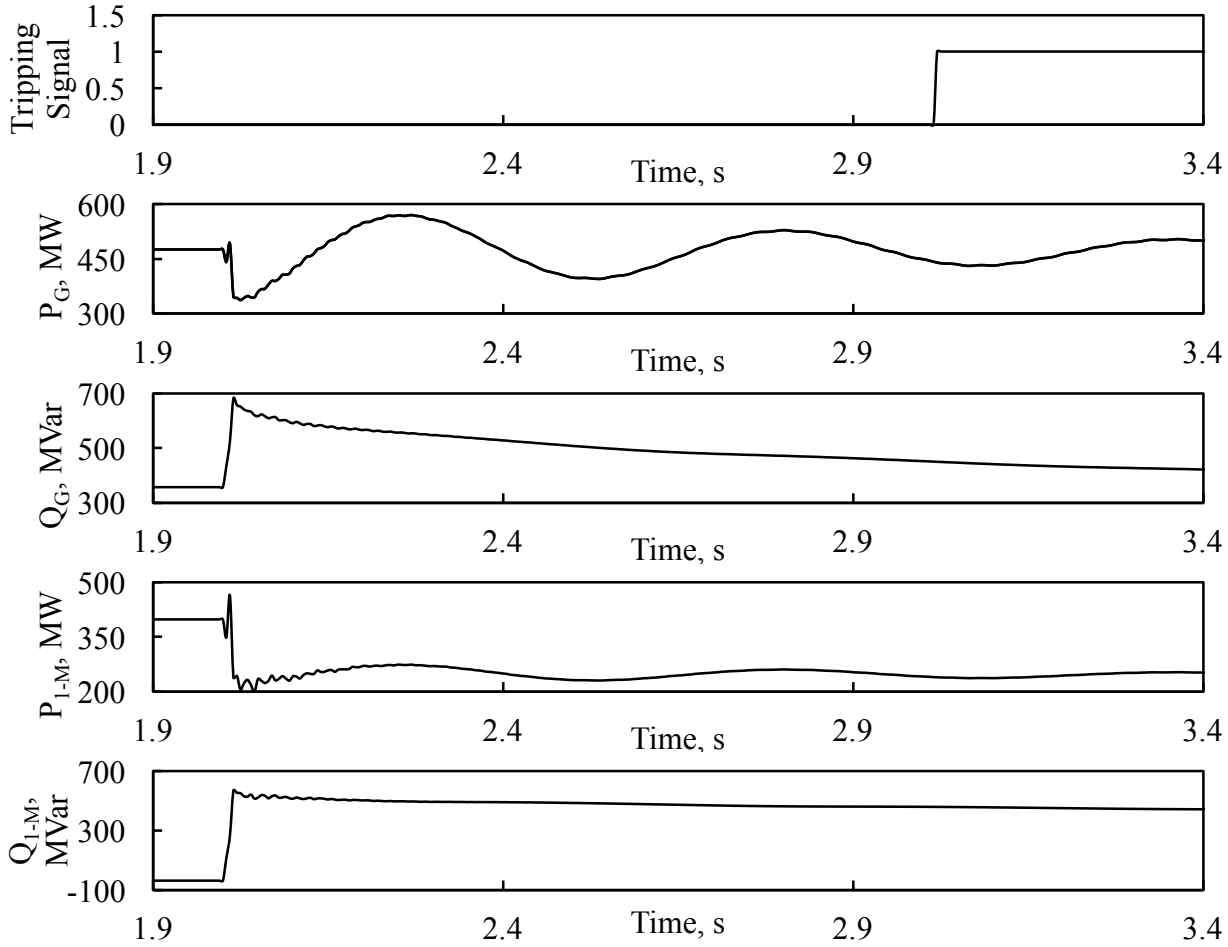

Figure 3.13: Relay (21) tripping signal, transient time responses of generator active and reactive powers, active and reactive power flows from bus 1 to bus M during a line-to-line fault at F_2 (no wind farm in the system, generator loading is 85%).

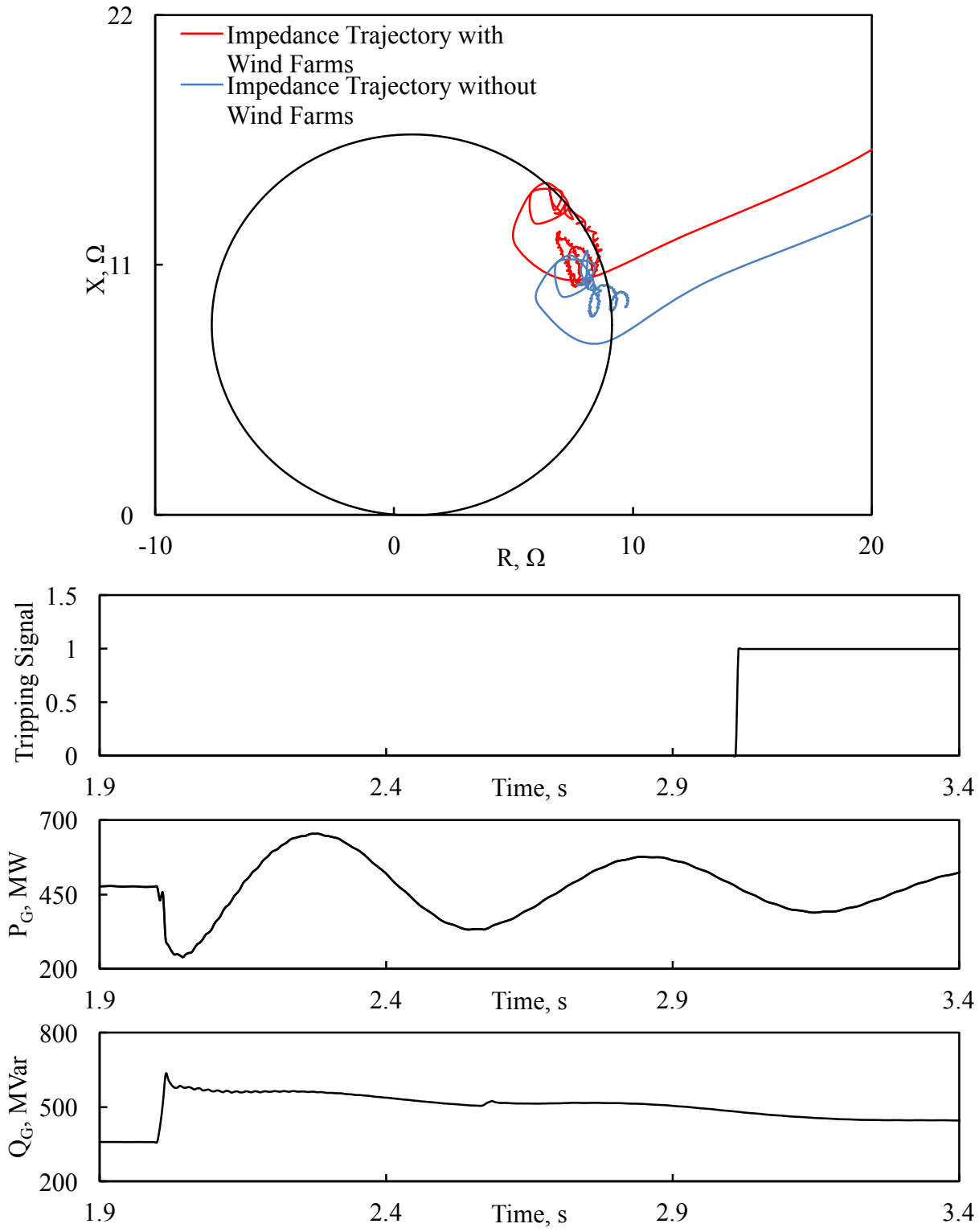

Figure 3.14: Relay (21) measured impedance trajectory and its tripping signal, transient time responses of generator active and reactive powers, active and reactive power flows from bus 1 to bus M, DFIG- and FFC-based wind farm active and reactive powers during a line-to-line fault at F_2 (generator loading is 85%).

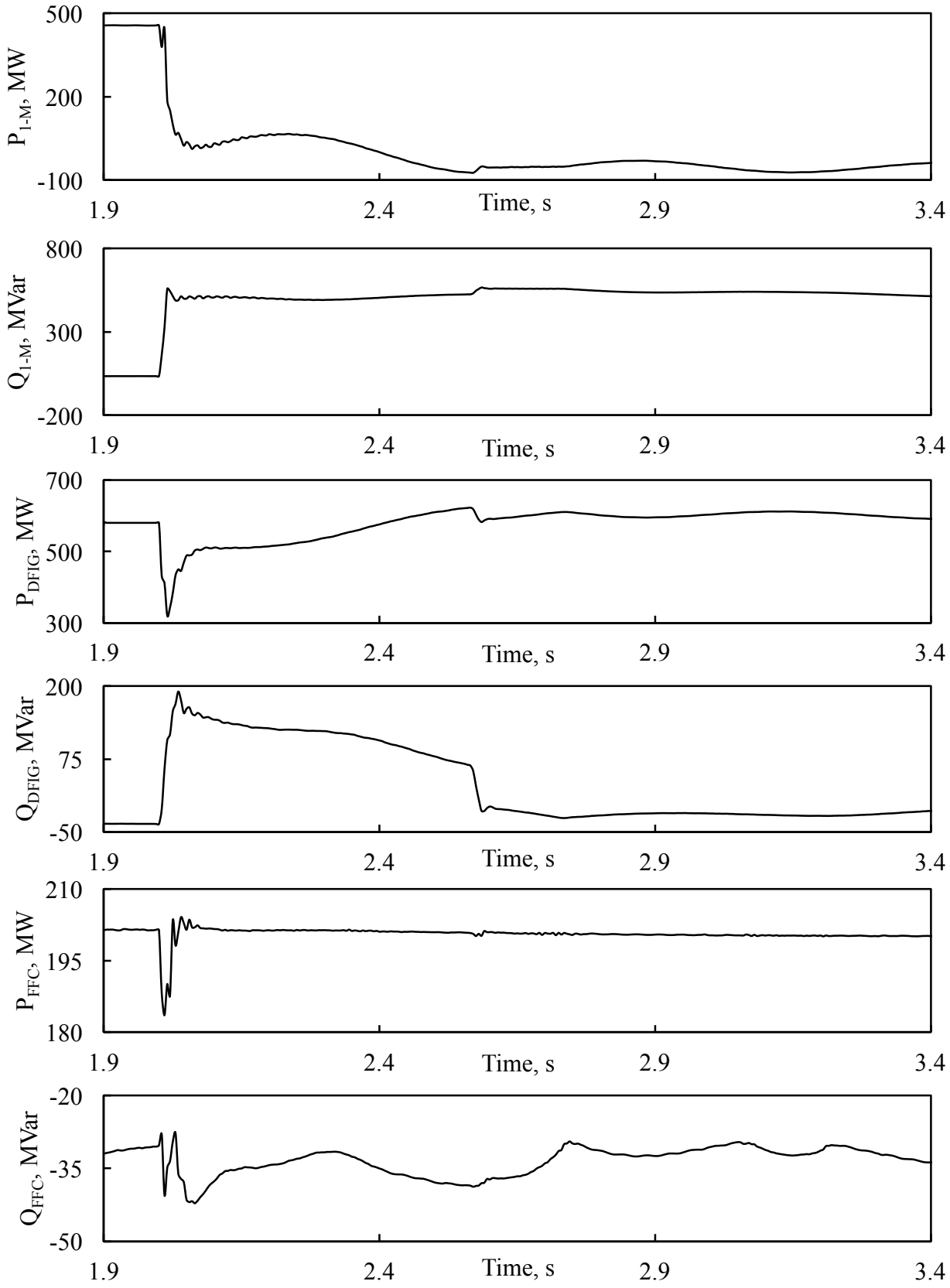

Figure 3.14: Continued

3.5.5 Performance of Relay (21) during a three-phase fault at F_3

Figures 3.15, 3.17 and 3.19 illustrate Relay (21) tripping signal (if applicable), the transient time responses of the generator active and reactive powers as well as the active and reactive power flows from bus 1 to bus M for the case of no wind farms in the system respectively for 65%, 75% and 85% generator loadings. Figures 3.16, 3.18 and 3.20 depict respectively the same responses for the case of DFIG- and FFC-based wind farms at buses M and N in addition to Relay (21) measured impedance trajectories and the wind farm real and reactive powers.

The effect of the generator loading on the system stability is clearly noticeable in these figures. At 65% generator loading, Figure 3.15 shows that the system is stable in the absence of the wind farms. Relay (21) issues a trip signal as its measured impedance trajectory, shown in Figure 3.16 enters the relay zone and stays inside it. With the presence of the wind farms, Figure 3.16 shows that despite the trip signal issued by Relay (21), the system exhibits instability which is clearly shown in the sustained oscillations in the FFC-based wind farm real and reactive powers. At 75% generator loadings, Relay (21) issues a trip signal for the cases without and with wind farms. The system, however, is unstable in both cases as shown in Figures 3.17 and 3.18. Severe system instability occurs at 85% generator loading in the absence and presence of the wind farm as shown in Figures 3.19 and 3.20. Relay (21) issues no trip signal in both cases. It is worth noting here that in the case of system instability, the generator out of step protection would disconnect the generator. The function of such a protection is disabled in the investigations conducted in this thesis.

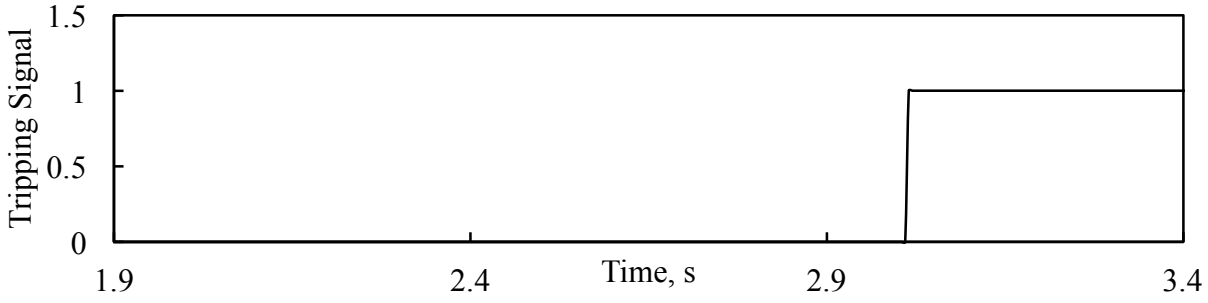

Figure 3.15: Relay (21) tripping signal, transient time responses of generator active and reactive powers, active and reactive power flows from bus 1 to bus M during a three-phase fault at F_3 (no wind farm in the system, generator loading is 65%).

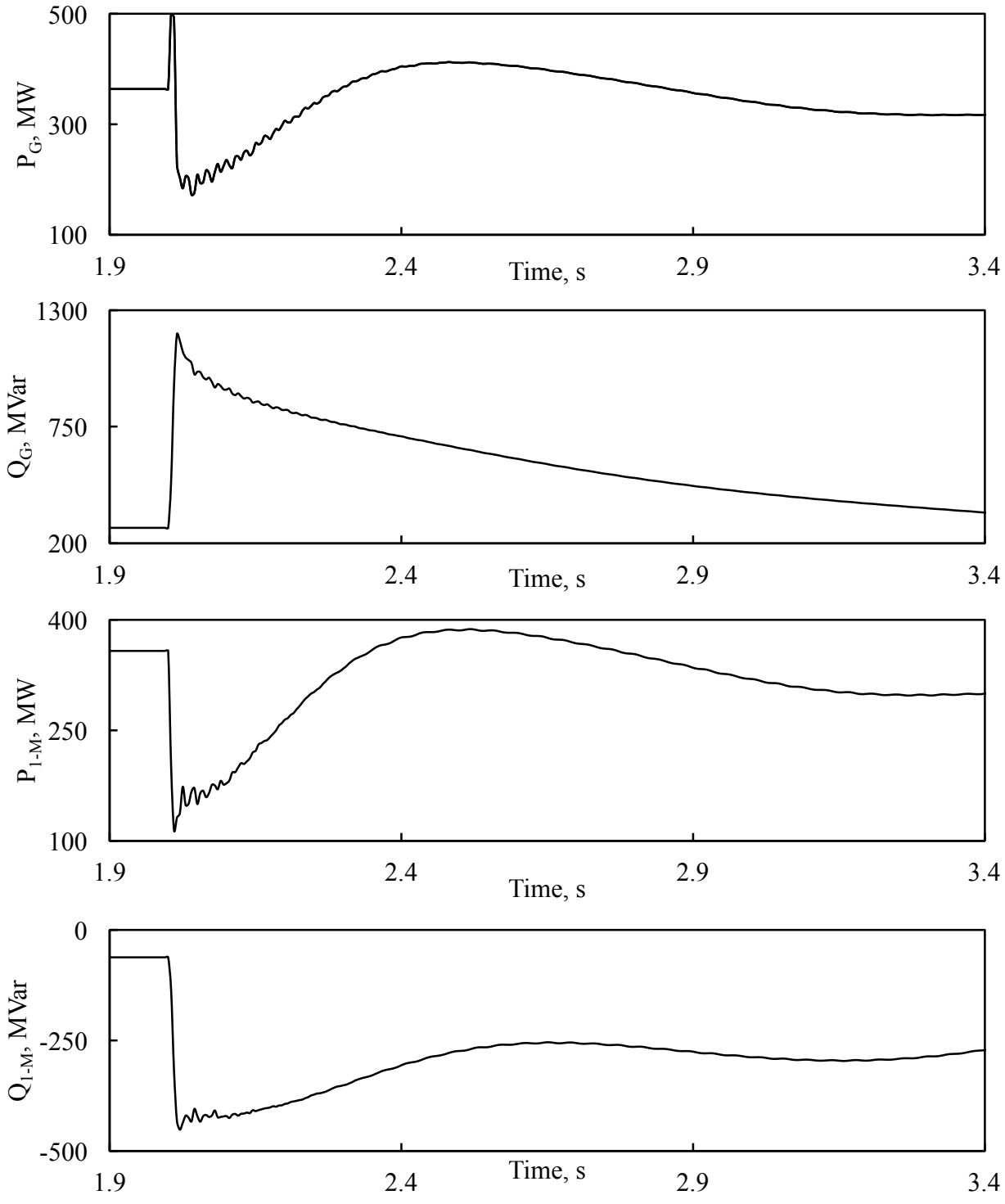

Figure 3.15: Continued.

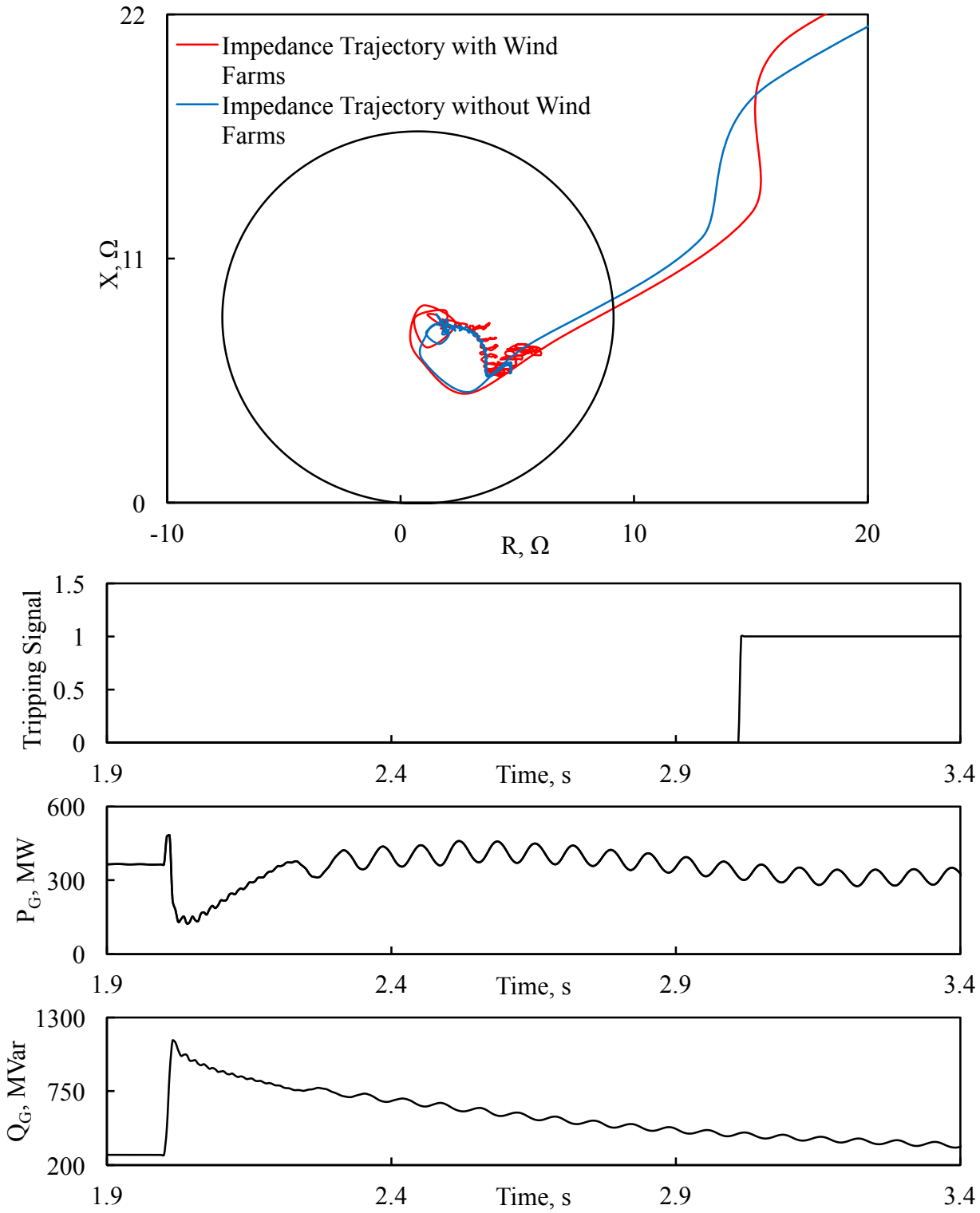

Figure 3.16: Relay (21) measured impedance trajectory and its tripping signal, transient time responses of generator active and reactive powers, active and reactive power flows from bus 1 to bus M, DFIG- and FFC-based wind farm active and reactive powers during a three-phase fault at F_3 (generator loading is 65%).

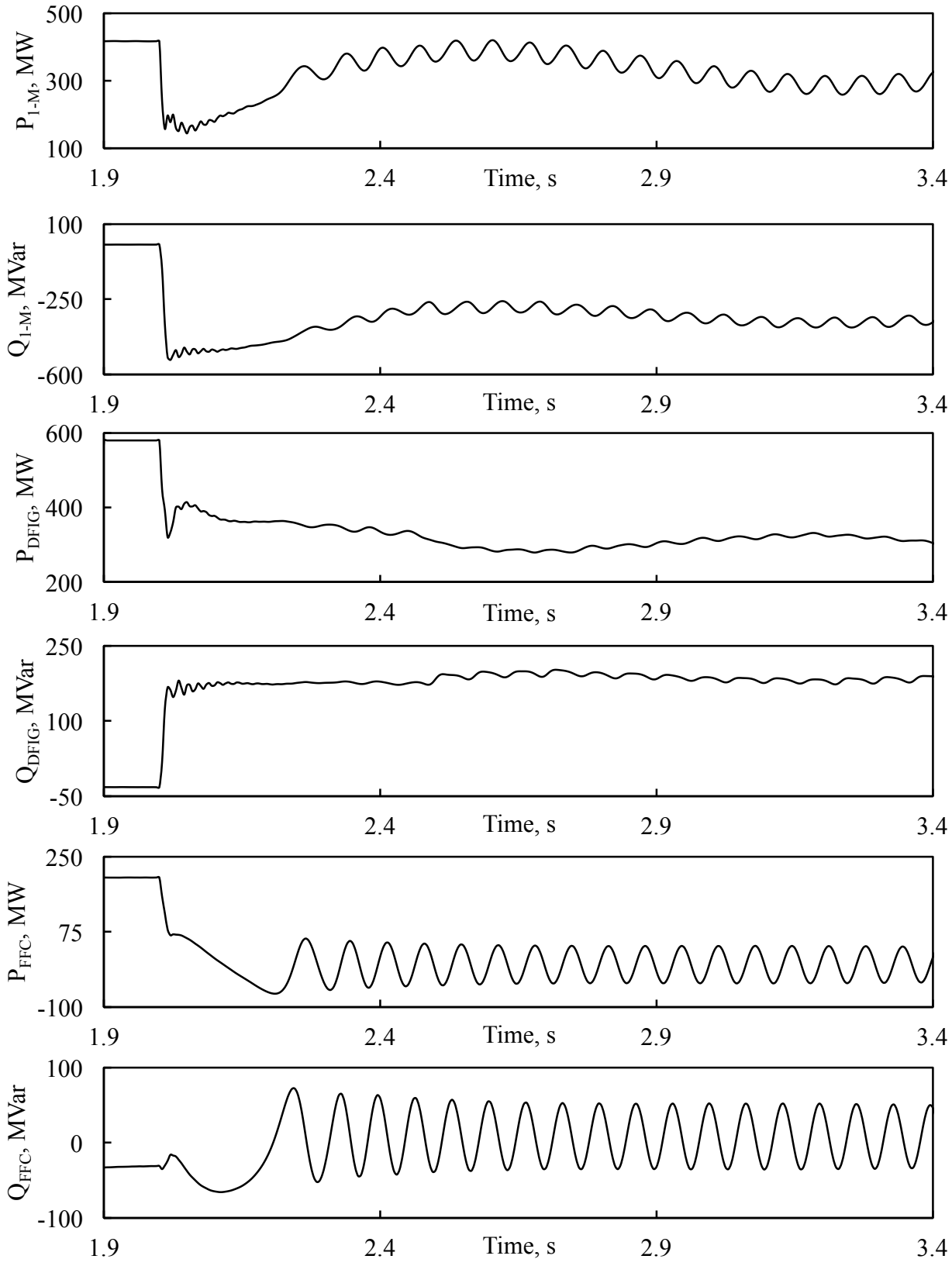

Figure 3.16: Continued.

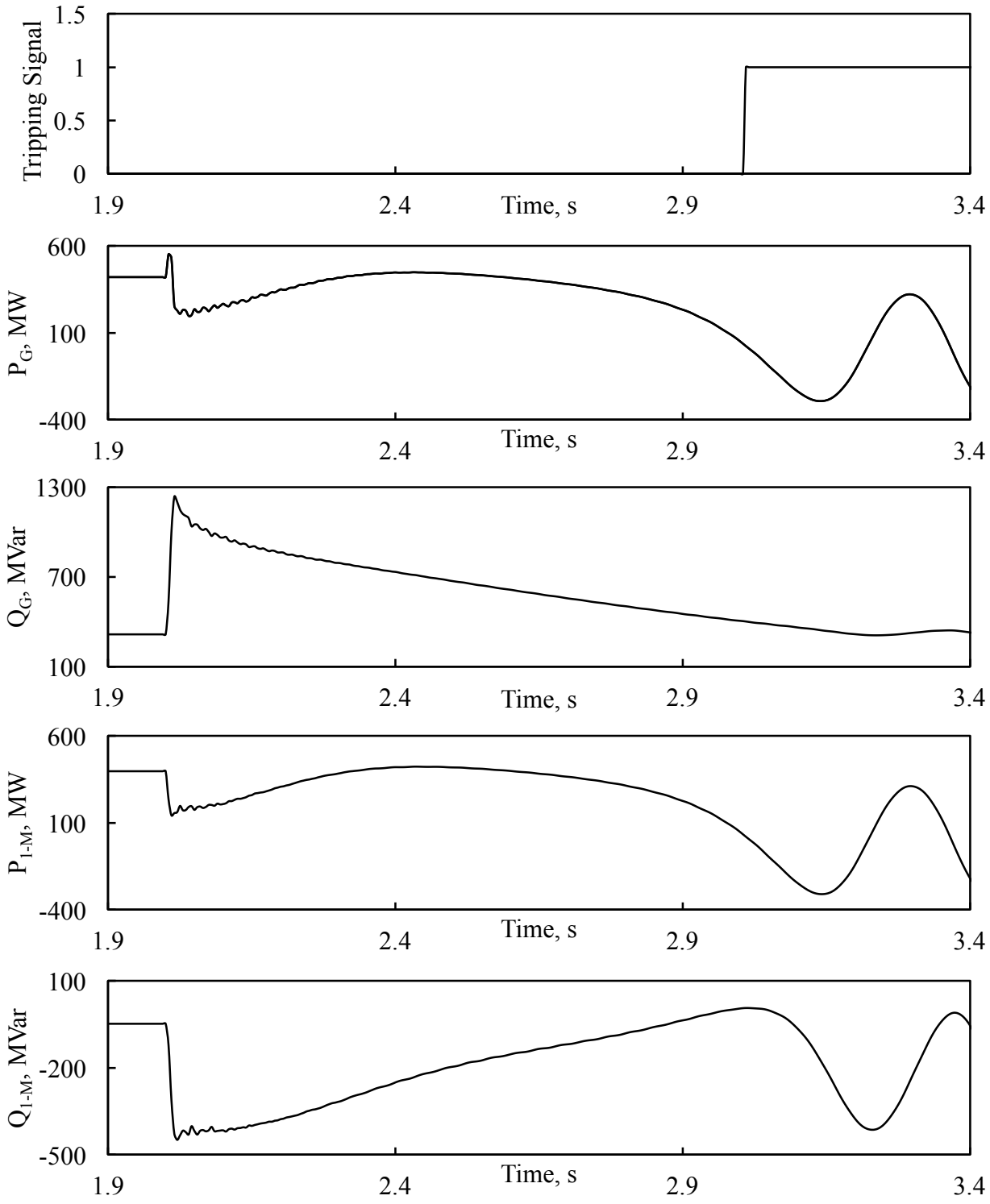

Figure 3.17: Relay (21) tripping signal, transient time responses of generator active and reactive powers, active and reactive power flows from bus 1 to bus M during a three-phase fault at F_3 (no wind farm in the system, generator loading is 75%).

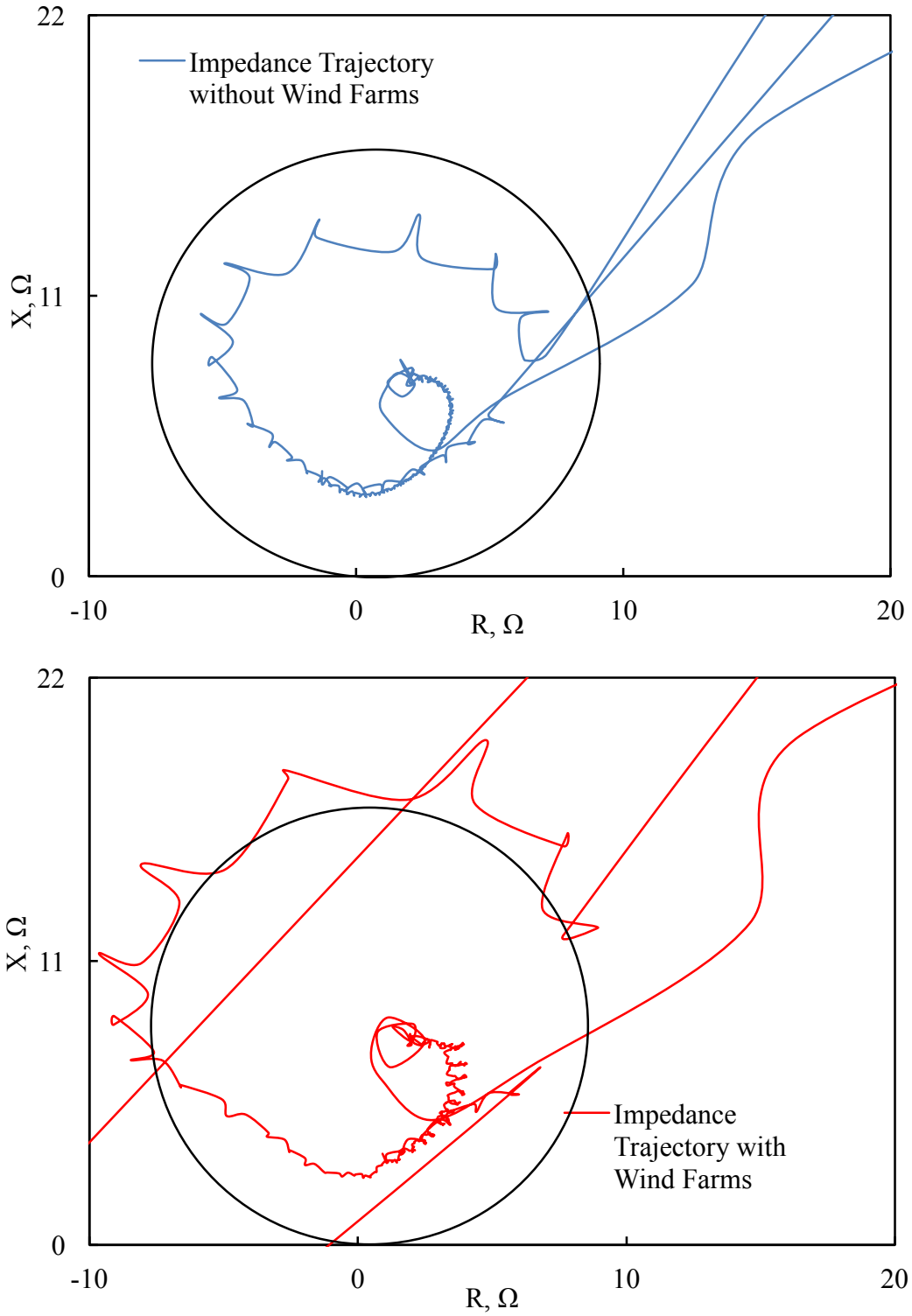

Figure 3.18: Relay (21) measured impedance trajectory and its tripping signal, transient time responses of generator active and reactive powers, active and reactive power flows from bus 1 to bus M, DFIG- and FFC-based wind farm active and reactive powers during a three-phase fault at F_3 (generator loading is 75%).

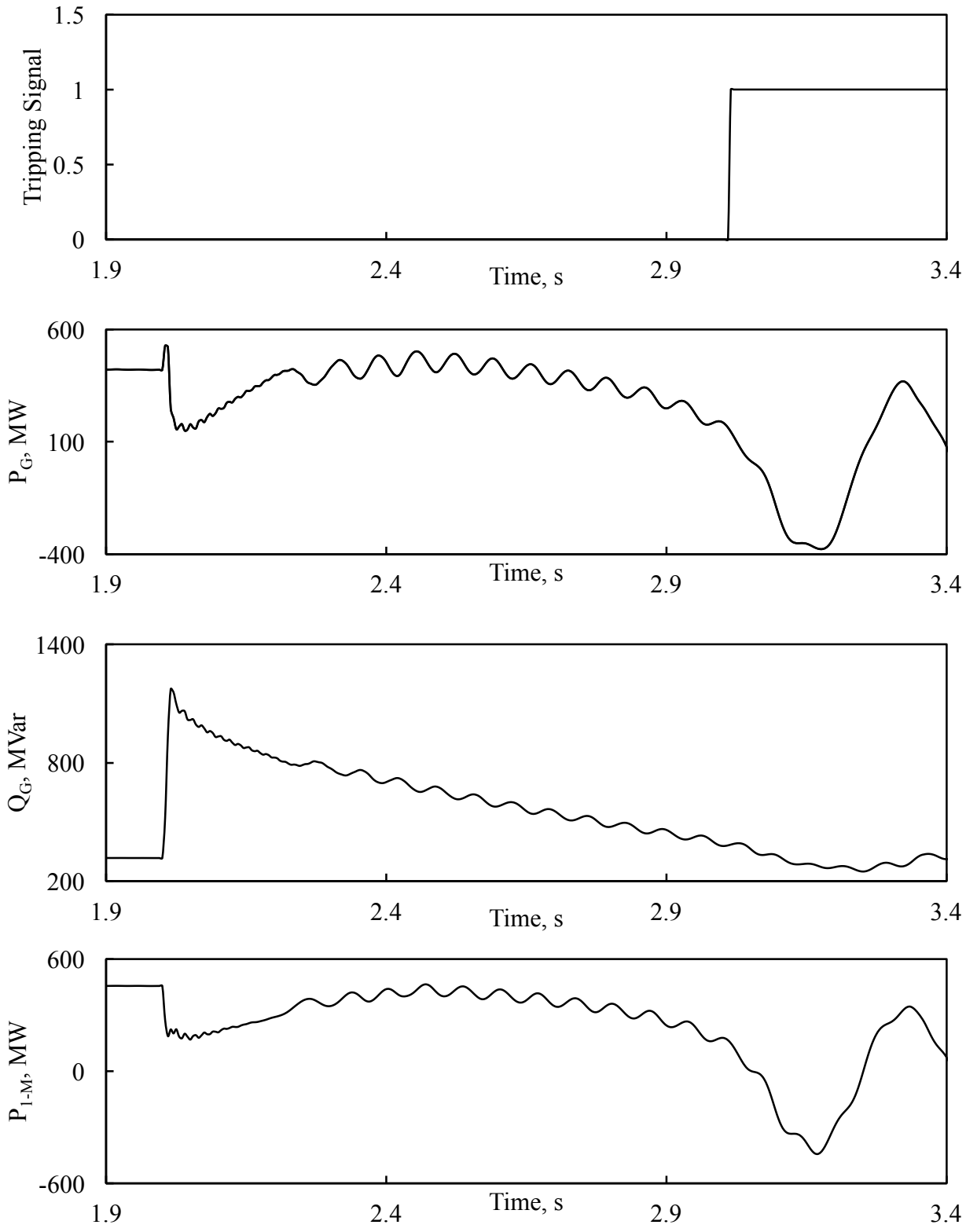

Figure 3.18: Continued.

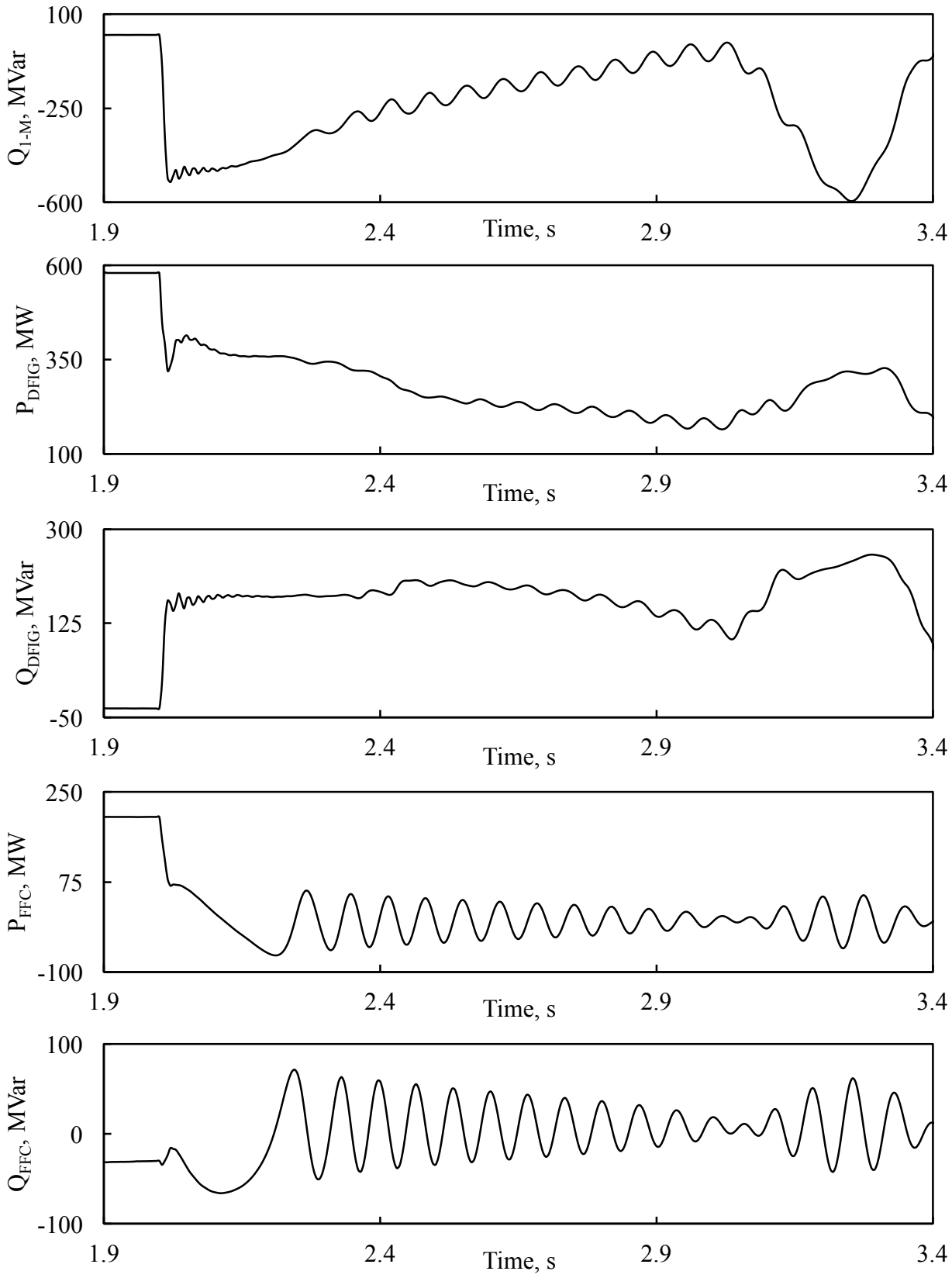

Figure 3.18: Continued.

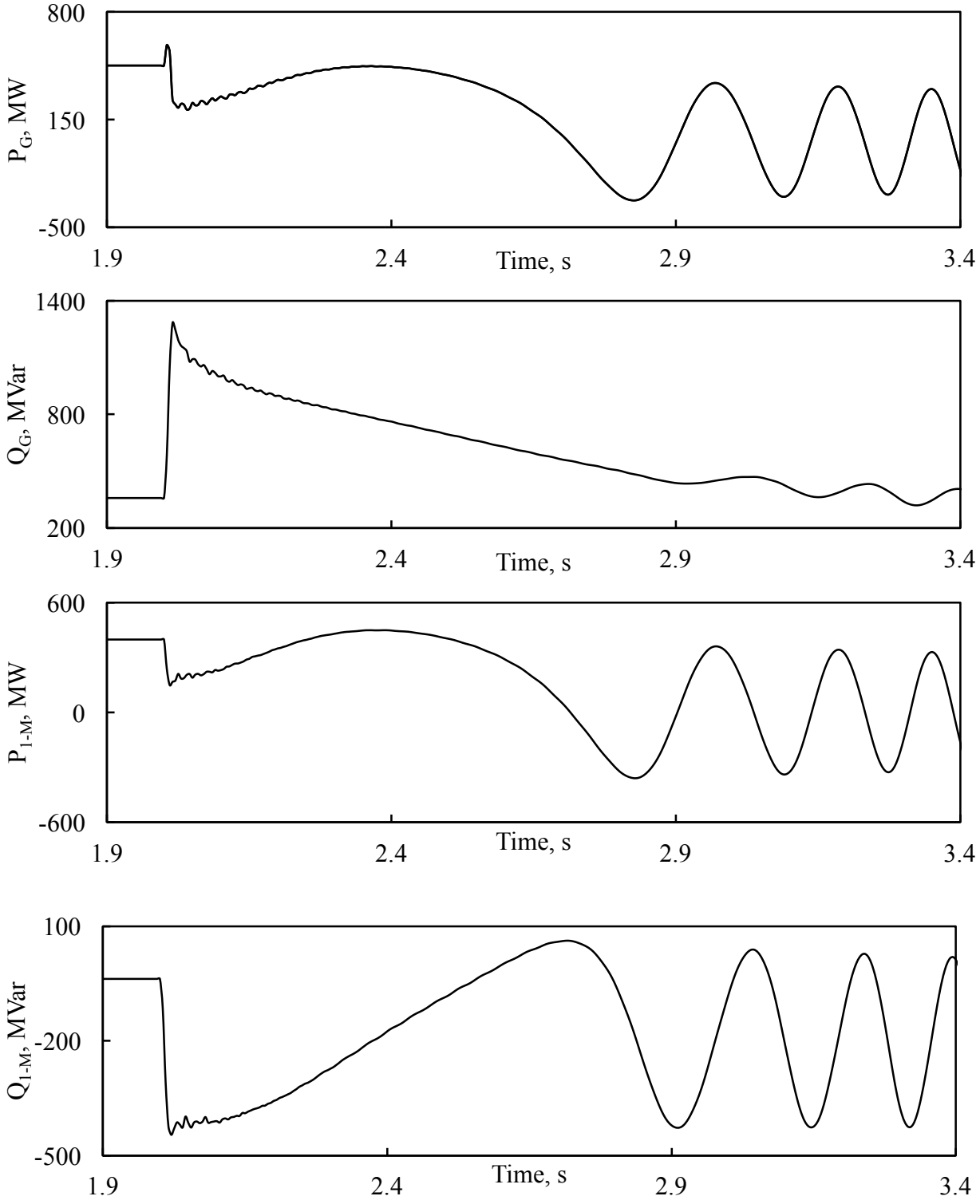

Figure 3.19: Transient time responses of generator active and reactive powers, active and reactive power flows from bus 1 to bus M during a three-phase fault at F_3 (no wind farm in the system, generator loading is 85%).

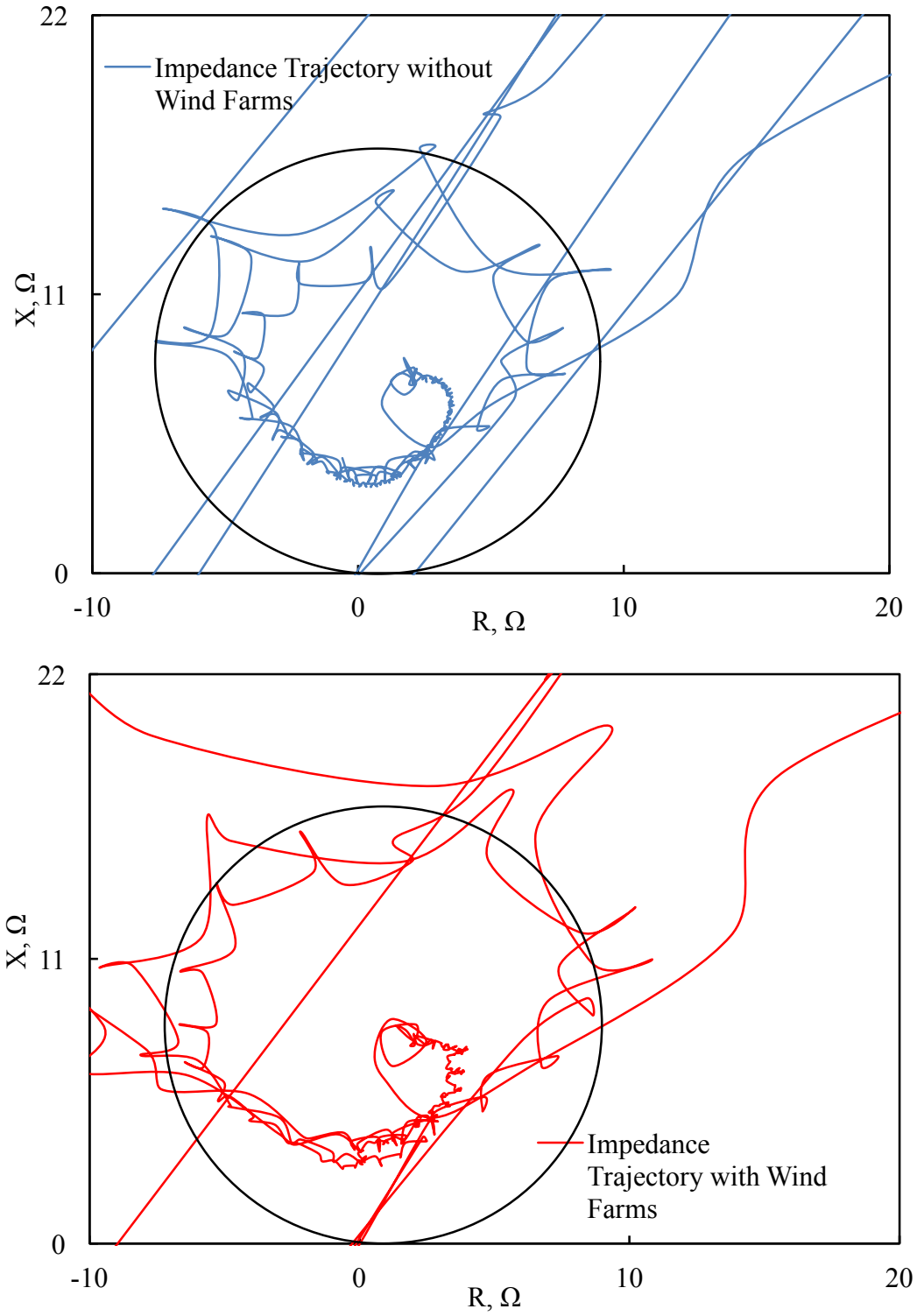

Figure 3.20: Relay (21) measured impedance trajectory, transient time responses of generator active and reactive powers, active and reactive power flows from bus 1 to bus M, DFIG- and FFC-based wind farm active and reactive powers during a three-phase fault at F_3 (generator loading is 85%).

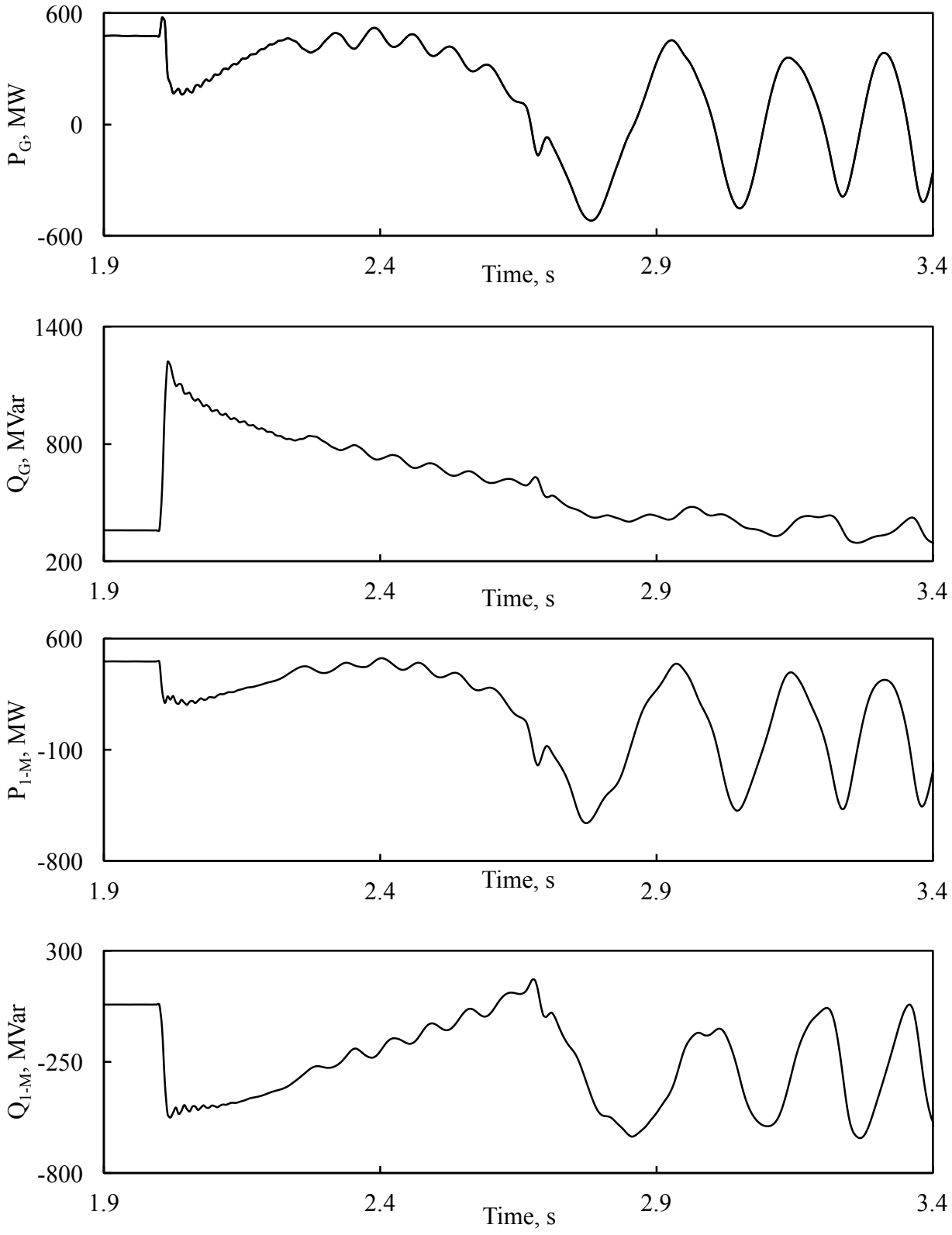

Figure 3.20: Continued.

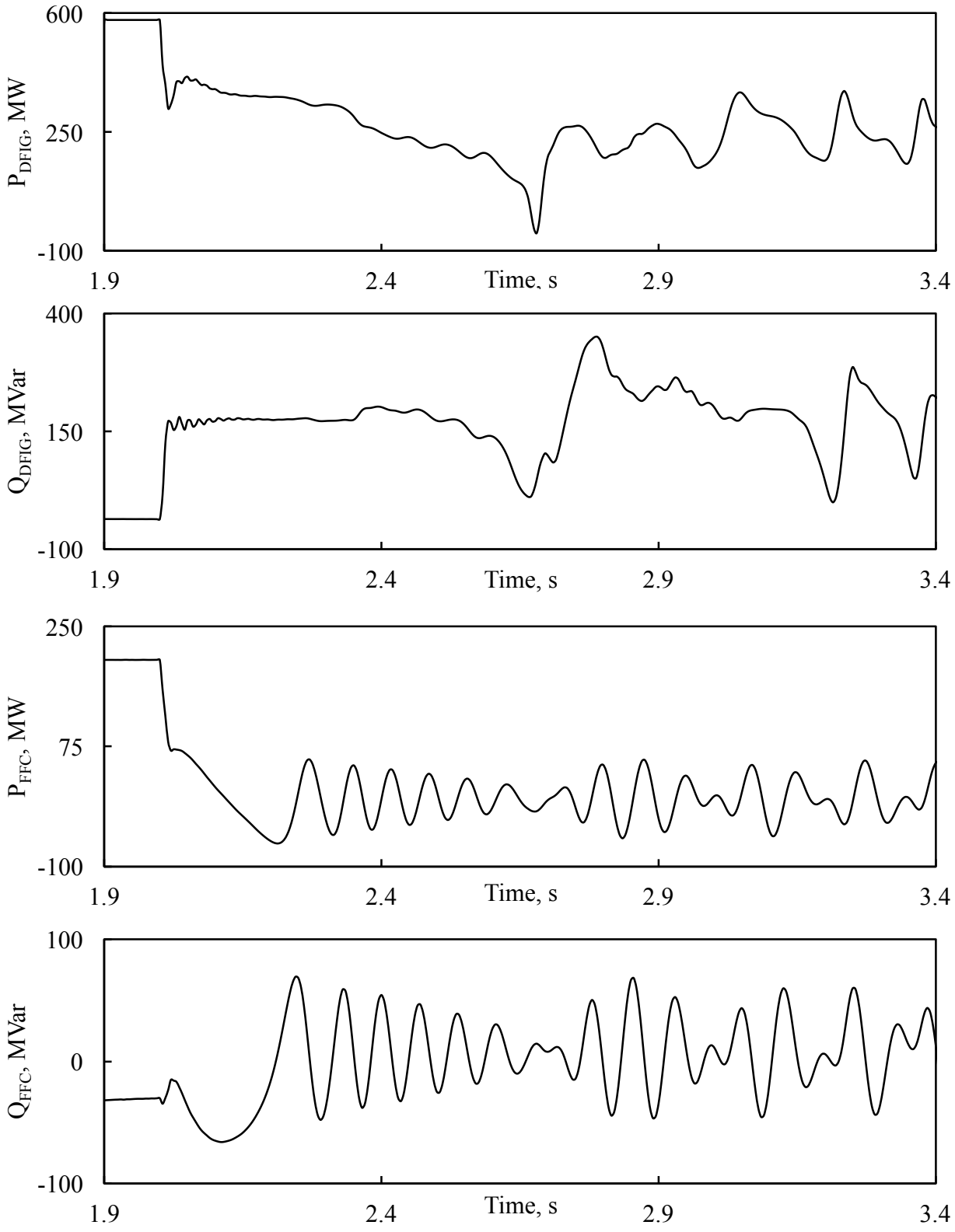

Figure 3.20: Continued.

3.5.6 Performance of Relay (21) during a line-to-line fault at F_3

Figure 3.21 illustrates Relay (21) tripping signal, the transient time responses of the generator active and reactive powers as well as the active and reactive power flows from bus 1 to bus M for the case of no wind farms in the system and 85% generator loading. Figure 3.22 depicts the same responses for the case of DFIG- and FFC-based wind farms at buses M and N in addition to the wind farm real and reactive powers and Relay (21) measured impedance trajectories. Unlike the severe cases of the three-phase fault at F_3, the presence of the wind farms does not cause Relay (21) to misoperate as shown in Figure 3.22. However, a noticeable difference between the measured impedance trajectories can be seen. It is worth noting here again that Relay (21) behaves in the same way for 65% and 75% generator loadings.

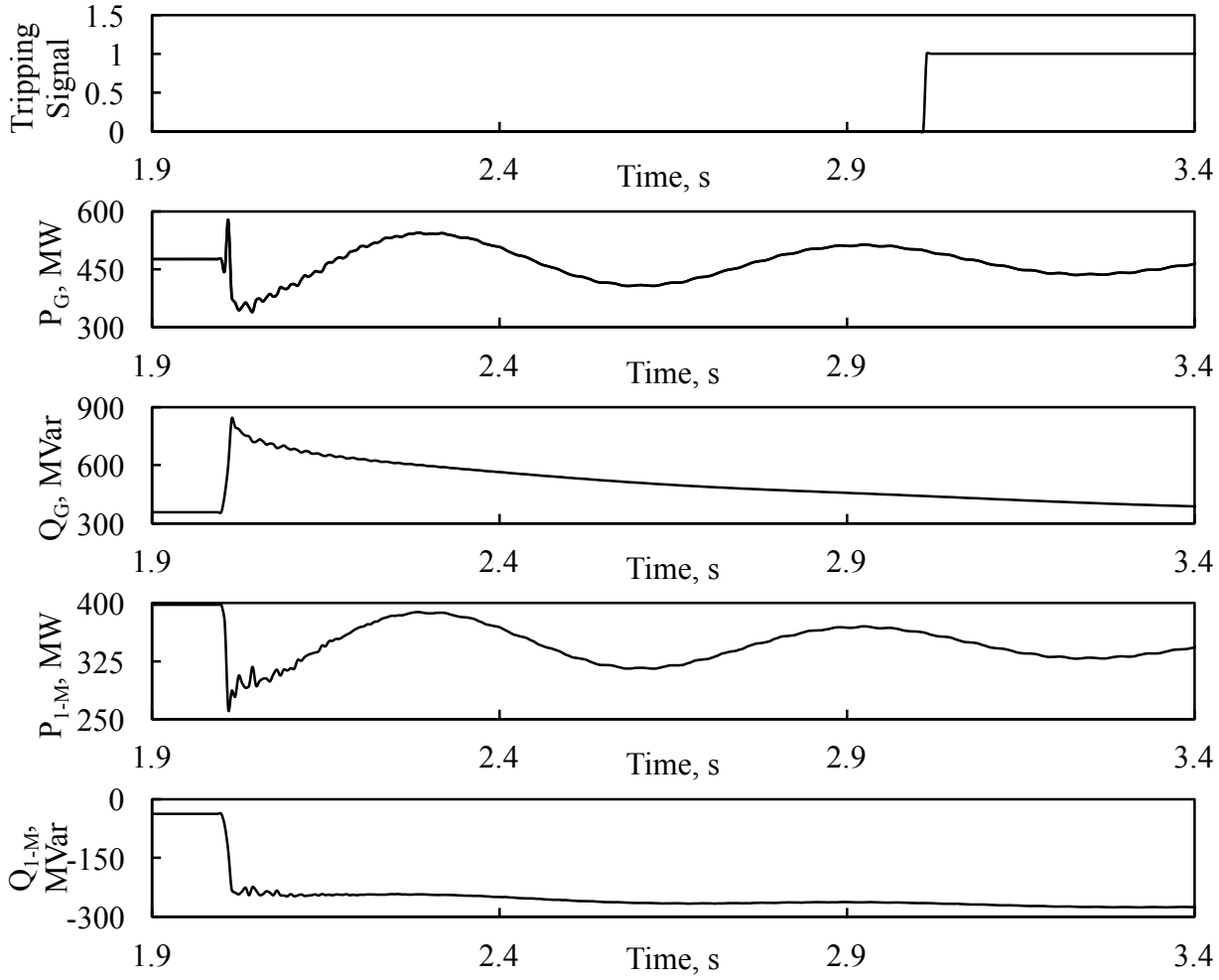

Figure 3.21: Relay (21) tripping signal, transient time responses of generator active and reactive powers, active and reactive power flows from bus 1 to bus M during a line-to-line fault at F_3 (no wind farm in the system, generator loading is 85%).

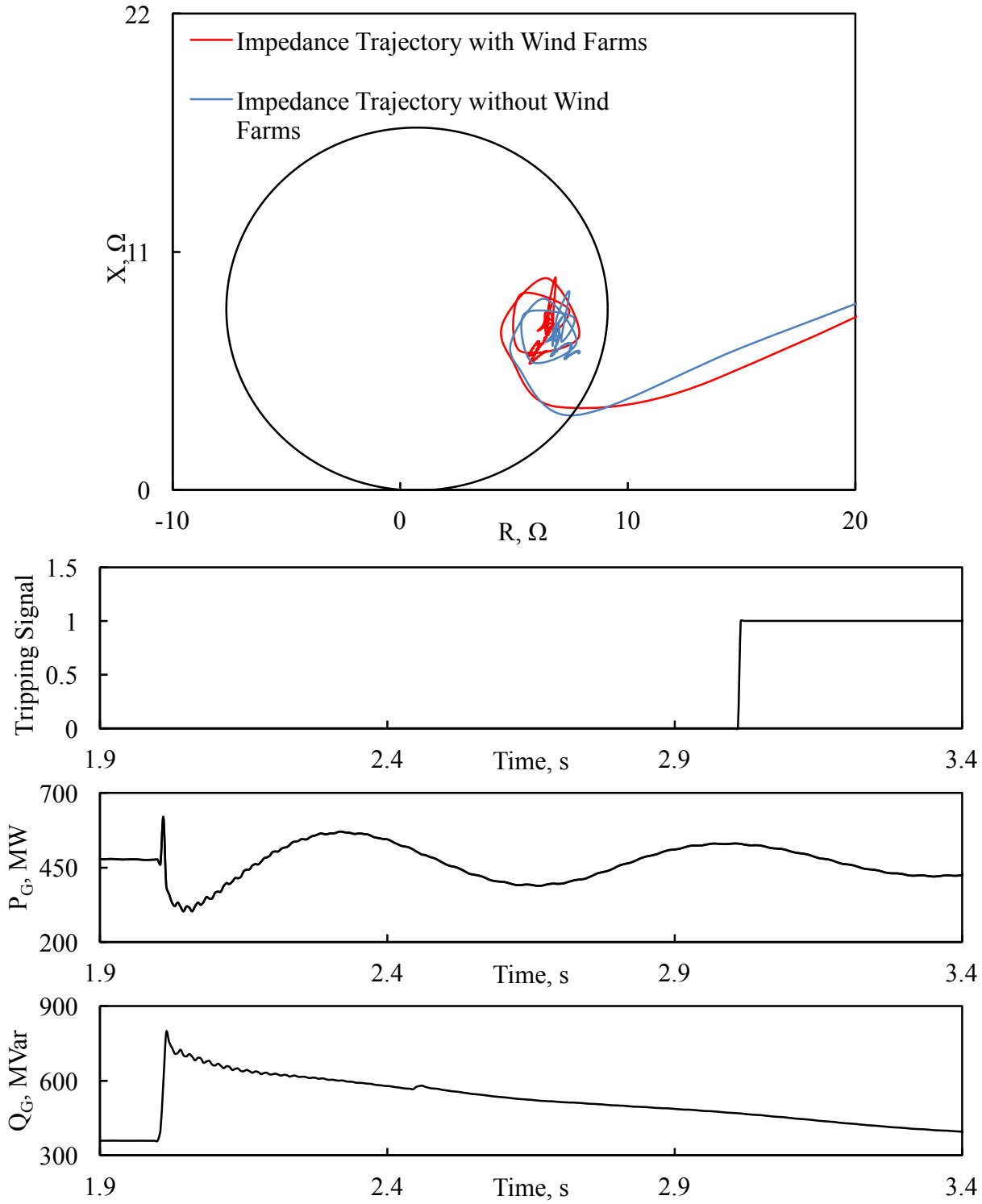

Figure 3.22: Relay (21) measured impedance trajectory and its tripping signal, transient time responses of generator active and reactive powers, active and reactive power flows from bus 1 to bus M, DFIG- and FFC-based wind farm active and reactive powers during a line-to-line fault at F_3 (generator loading is 85%).

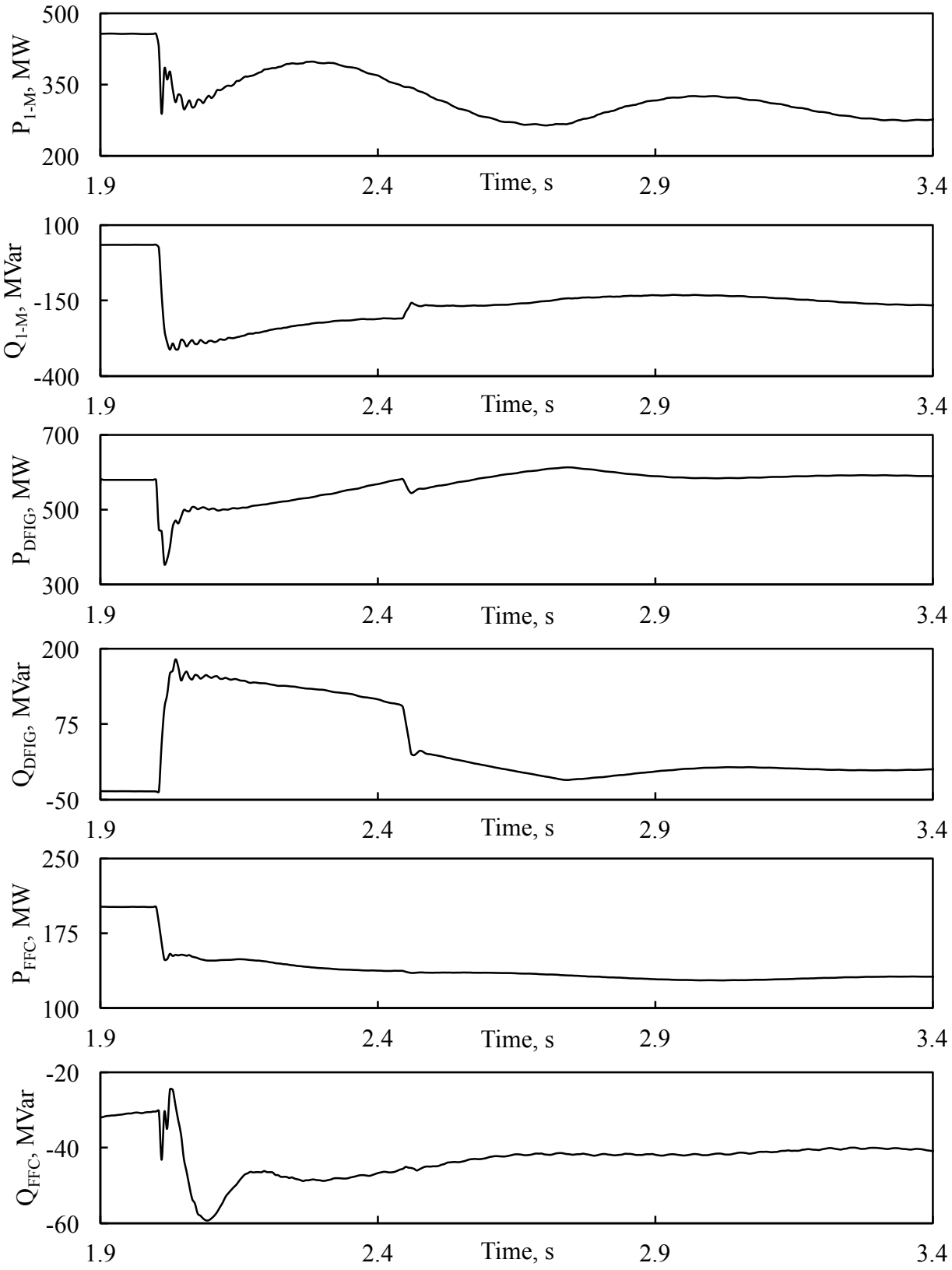

Figure 3.22: Continued.

Table 3.2 summarizes Relay (21) performance for the different case studies considered in the investigations of this thesis. The system transient time responses and Relay (21) measured impedance trajectories for those cases that are not presented in this chapter are given in Appendix C.

Table 3.2: Summary of Relay (21) performance for the case studies

Generator loading	Fault location	Fault type	Without wind farms	With wind farms
65%	F_1	L-L	Trip	Trip
		L-L-L	Trip	Trip
	F_2	L-L	Trip	Trip
		L-L-L	Trip	No Trip (under-reach)
	F_3	L-L	Trip	Trip
		L-L-L	Trip	Trip
75%	F_1	L-L	Trip	Trip
		L-L-L	Trip	Trip
	F_2	L-L	Trip	Trip
		L-L-L	Trip	No Trip (under-reach)
	F_3	L-L	Trip	Trip
		L-L-L	Trip	Trip
85%	F_1	L-L	Trip	Trip
		L-L-L	Trip	No Trip (under-reach)
	F_2	L-L	Trip	Trip
		L-L-L	Trip	No Trip (under-reach)
	F_3	L-L	Trip	Trip
		L-L-L	No Trip (under-reach)	No Trip (under-reach)

3.6 Impact of the DFIG- and FFC-Based Wind Farms on the Coordination between Relay (21) and GCC

The coordination between Relay (21) and the generator capability curve is maintained as long as the measured impedance by Relay (21) is inside the circle of Z_{GCC}. In order to examine the impact of the wind farm on such coordination, a coordination index is defined as

$$CI = \frac{\overline{o\,Z_W}}{J_{ZGCC}} \tag{3.32}$$

CI is illustrated graphically in Figure 3.23 where RW is the real part of measured impedance by Relay (21) and J_{ZGCC} is the radius of the circle of Z_{GCC}. The coordination is lost if CI is greater than 1.

Figure 3.25 is a zoom-in of Figure 3.24 which illustrates Relay (21) measured impedance trajectories during a three-phase fault at F_2 for an 85% generator loading. Figure 3.26 illustrates the same trajectories for the same fault type and location for a 65% generator loading. A zoom-in on these trajectories is shown in Figure 3.27. A case of loss of coordination is clearly shown in Figure 3.27 as Relay (21) measured impedance trajectory in the presence of the wind farm is entirely outside the circle of Z_{GCC}. Obviously, loss of coordination would also occur at other generator loadings less than 65%. The CI for these two cases are: $CI_{85\%}$=1.5511, $CI_{65\%}$=1.8030.

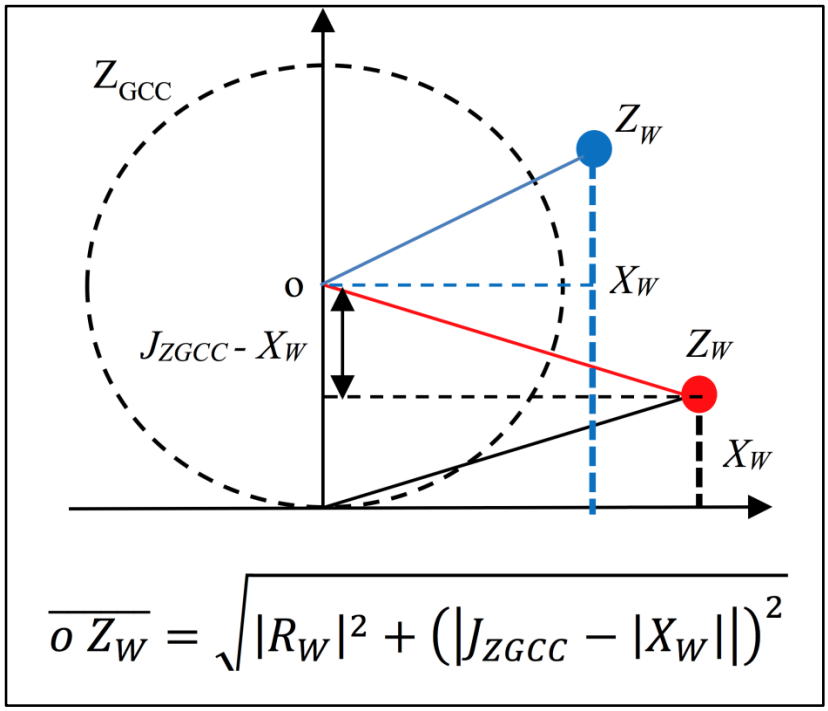

Figure 3.23: Calculation of the coordination index CI.

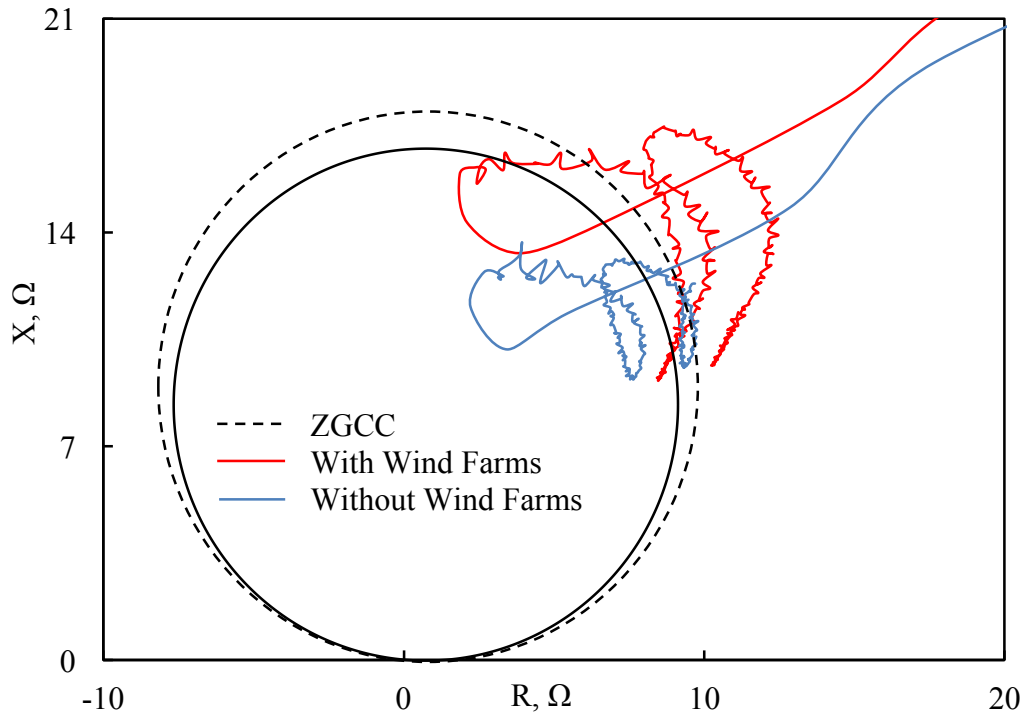

Figure 3.24: Relay (21) measured impedance trajectories during a three-phase fault at F_2 (85% generator loading).

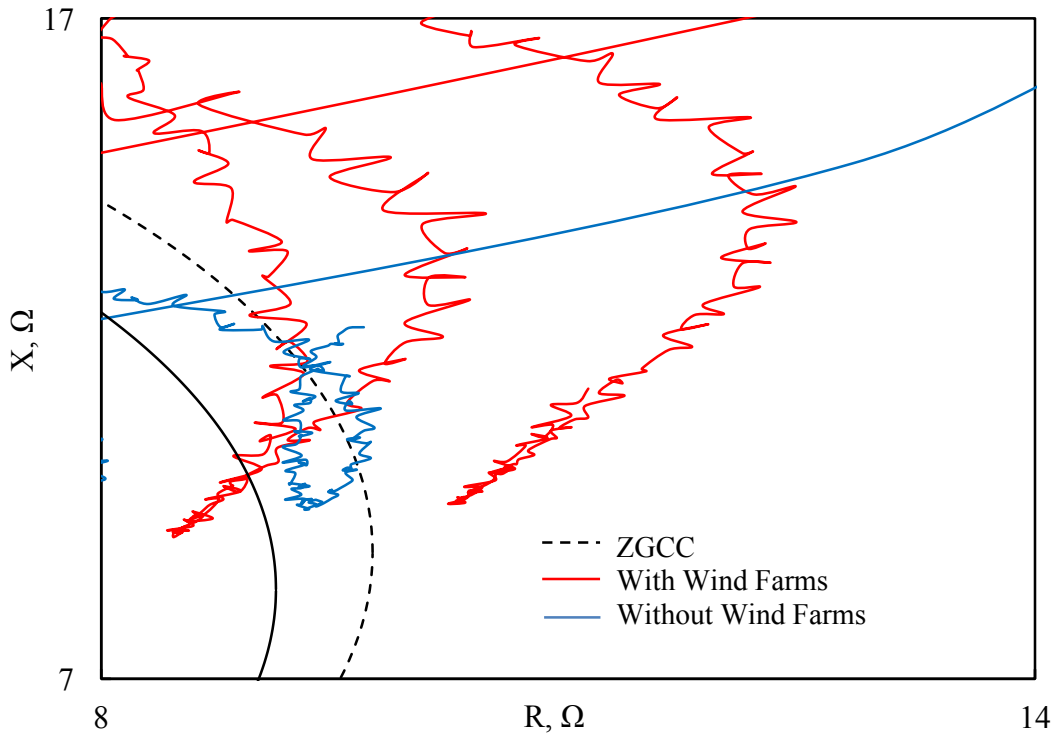

Figure 3.25: Zoom in of Relay (21) measured impedance trajectories during a three-phase fault at F_2 (85% generator loading).

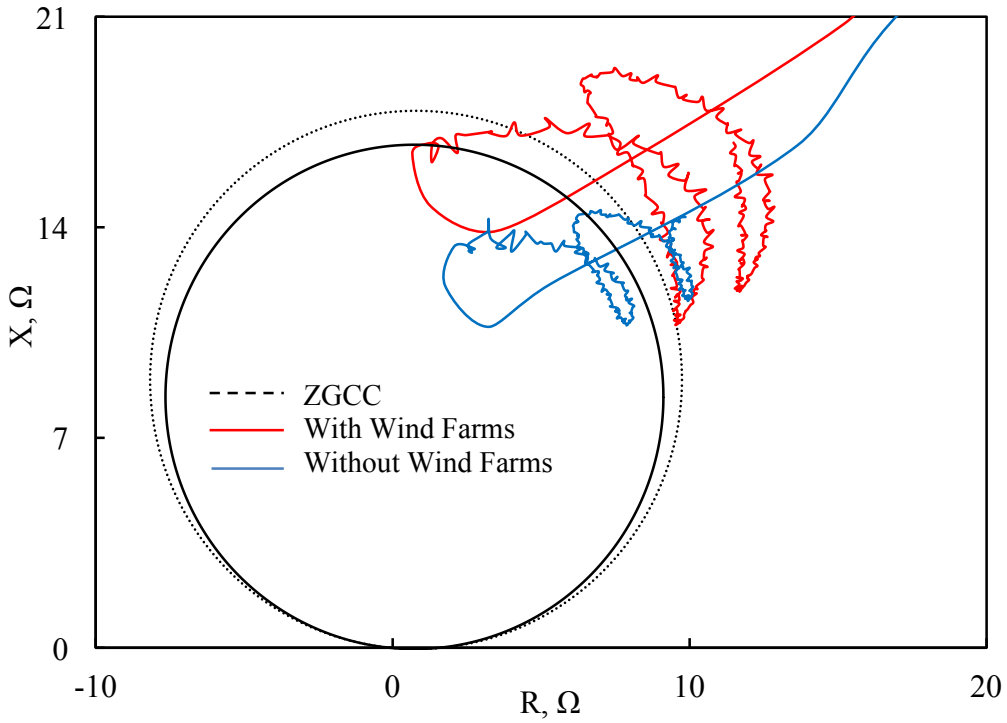

Figure 3.26: Relay (21) measured impedance trajectories during a three-phase fault at F_2 (65% generator loading).

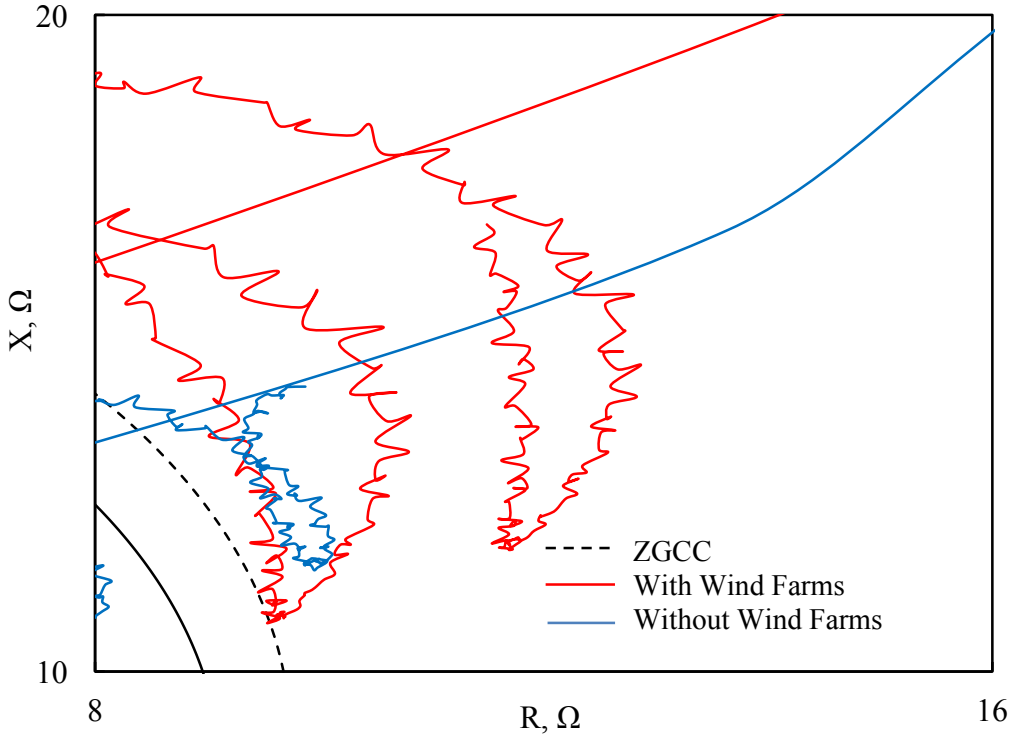

Figure 3.27: Zoom in of Relay (21) measured impedance trajectories during a three-phase fault at F_2 (65% generator loading).

4. SUMMARY AND CONCLUSIONS

4.1 Summary

Worldwide concern about the environmental pollution and a possible energy crisis has led to increasing interest in technologies for generation of clean and renewable electrical energy. Among various renewable energy sources, wind power is the most rapidly growing one. Wind power is one of the most cost-effective sources of electricity available, capable of generating power at prices competitive with new natural gas plants and cheaper than new coal and nuclear plants. And compared with fossil fuels, wind power offers substantial public health, economic, and environmental benefits.

Integration of large wind farms into bulk power systems presents, however, multiple challenges to system operation and security. One particular challenge to system security is the malfunction of system protective relays during transmission system faults. This is due to the fact that high wind energy penetration levels can significantly affect the steady-state as well as the transient stability of the systems due to their distinct characteristics that differ from conventional generation.

This thesis investigates the impact of Doubly-Fed Induction Generator and Full-Frequency Converter based wind farms on the performance of the generator distance phase backup protection element (Relay (21)). In this context, investigations are conducted in a sample power system incorporating two wind farms tapped to the transmission system. Attention is focused on the performance of Relay (21) during line-to-line and three-phase faults at different locations. The thesis investigates also the impact of the wind farms on the coordination between Relay (21) and the generator capability curves.

The benefits of wind energy are presented in Chapter 1. A brief introduction on distance relaying and generator protection is also included. The objective of the research is drawn from the literature review on the impact of large wind farms on the performance of distance protection of transmission lines.

In Chapter 2, the system used in the studies conducted in this thesis is introduced and the mathematical models of its components are presented. The results of digital time-domain

simulations of a case study for the system in the absence of the wind farms during line-to-line and three-phase faults are also presented in this chapter.

Chapter 3 explores the impact of DFIG- and FFC-based wind farms on the performance of generator distance phase backup protection (Relay (21)) through comprehensive time-domain simulations of case studies of line-to-line and three-phase faults at different locations and different generator loadings.

4.2 Conclusions

The studies conducted in this thesis yield the following conclusions for the system under study:

1. Both the DFIG- and FFC-based wind farms have an adverse effect on the generator distance phase backup protection. This impact varies according to the fault type, fault location and generator loading.
2. The under-reach cases of Relay (21) has occurred only during three-phase faults at the end of the longest transmission line L_1 at all considered generator loadings, namely 65%, 75% and 85% of rated MVA.
3. The adverse effect of the wind farms on Relay (21) performance extends to affect the coordination between generator distance phase backup protection and the GOEC limit. Such an impact varies also according to the fault type, fault location and generator loading. In this regard, it has been found that the maximum setting of Relay (21), which can keep the coordination with the GOEC limits, is 17.91 Ω at MTA of 85°. With the presence of the wind farms, it has been shown that this limit has been exceeded at all generator loadings during three-phase fault at the end of the longest transmission line L_1.
4. For systems with a large penetration of wind energy where multiple wind farms are tapped to various transmission lines, it is essential to include, if possible, all wind farms near Relay (21) in nearby generating station in the assessment of the relay performance. The reason is that while attention might be focused on the impact of a large wind farm near Relay (21) (as the primary source of the problem), another wind farm (secondary) might have a significant influence on the relay performance. As an example, such a wind farm might be altering the “in-feed” current from the line that is tapped to it.

REFERENCES

[1] https://en.wikipedia.org/wiki/Renewable_energy

[2] https://www.canadahydro.ca

[3] https://en.wikipedia.org/wiki/Wind_power_in_Canada

[4] https://en.wikipedia.org/wiki/Wind_power

[5] W. Elmore, *Protective Relaying Theory and Applications*, CRC Press, second edition, 2004.

[6] D. Reimert, *Protective Relaying for Power Generation Systems*, CRC Press, 2006.

[7] P.M. Anderson, *Power System Protection*, IEEE Press-McGraw-Hill, 1999.

[8] G. Ziegler, *Numerical distance Protection principle and Applications*, Publics Corporate Publishing, Erlangen, Germany, Publicis Corporate Publishing, Erlangen, third edition, 2008.

[9] https://en.wikipedia.org/wiki/Wind_turbine

[10] O. Anaya-Lara, N. Jenkins, J. Ekanayake, P. Cartwright, and M. Hughes, Wind Energy Generation: Modelling and Control, Wiley, 2009, John Wiley & Sons, Ltd.

[11] B. Babak, S. Mandhir, Z. Yi, M. Dharshana and G. Aniruddha, "General Methodology for Analysis of Sub-Synchronous Interaction in Wind Power Plants," *IEEE Transactions on Power Systems*, Vol. 28, No. 2, May 2013, pp. 1858-1869.

[12] L. Fan, R. Kavasseri, Z. Lee Miao and C. Zhu, "Modeling of DFIG-Based Wind Farms for SSR Analysis," *IEEE Transactions on Power Delivery*, Vol. 25, No. 4, October 2010, pp. 2073-2082.

[13] A.R. Kashyap, "Direct-Drive Permanent Magnet Synchronous Generator Design for Hydrokinetic Energy Extraction", a thesis for master of science in electrical engineering, Missouri University of Science and Technology, Rolla, Missouri, United States, 2013.

[14] A.D. Hansen and G. Michalke, "Multi-pole permanent magnet synchronous generator wind turbines' grid support capability in uninterrupted operation during grid faults," *IET Renewable Power Generation*, Vol. 3, Issue 3,September 2009.

[15] B. Chen, A. Shrestha, F.A. Ituzaro, and N. Fischer, "Addressing Protection Challenges Associated with Type 3 and Type 4 Wind Turbine Generators", in *68th Annual Conference for Protective Relay Engineers*, Texas, USA, March 30 - April 2, 2015.

[16] L. He, C. Liu, "Impact of LVRT Capability of Wind Turbines on Distance Protection of AC Grids", in *Innovative Smart Grid Technologies (ISGT) Conference*, Washington, DC, USA, February 24 – February 27, 2013.

[17] C. Pannell, D.J. Atkinson, and B. Zahawi, "Minimum-threshold crowbar for a fault-ride-through grid-code-compliant DFIG wind turbine," *IEEE Trans. on Energy Convers.*, vol. 22, no. 3, pp. 976-984, Aug. 2007.

[18] J. Morren, and S.W. Haan, "Ride through of wind turbines with doubly- fed induction generator during a voltage dip,"*IEEE Trans. on Energy Convers.*, vol. 20, no. 2, pp. 435-441, June 2005.

[19] M. Elsamahy, S.O. Faried and G. Ramakrishna, "Impact of Midpoint STATCOM on the Coordination between Generator Distance Phase Backup Protection and Generator Capability Curves," paper No. 2010GM1138, *IEEE Power and Energy Society General meeting*, Minneapolis, Minnesota, July 25 - 29, 2010.

[20] M. Elsamahy, S.O. Faried, T.S. Sidhu, R. Gokaraju, "Enhancement of the Coordination between Generator Phase Backup Protection and Generator Capability Curves in the Presence of a Midpoint STATCOM using Support Vector Machines," *IEEE Transactions on Power Delivery*, Vol. 26, No. 3, July 2011, pp. 1841-1853.

[21] P. Kundur, *Power System Stability and Control,* New York, McGraw-Hill, 1994.

[22] Y. Yu, *Electric Power System Dynamics,* New York, Academic Press, 1983.

[23] A.D. Hansen, G. Michalke, P. Sorensen, T. Lund and Florin Iov, "Co-ordinated Voltage Control of DFIG Wind Turbines in Uninterrupted Operation during Grid Faults," *Wind Energy*, Vol. 10, No. 1, January/February 2007, pp. 51-68, published online, DOI: 10.1002/we.207.

[24] J. Morren, S. W. H. de Haan, P. Bauer, J. Pierik, and J. Bozelie, "Comparison of Complete and Reduced Models of a Wind Turbine with Doubly-fed Induction Generator," in *Proc. 10th European Conference on Power Electronics and Applications*., Toulouse, France, September 2-4, 2003, pp. 1–10.

[25] J. G. Slootweg, H. Polinder, and W. L. Kling, "Representing Wind Turbine Electrical Generating Systems in Fundamental Frequency Simulations," *IEEE Transactions on Energy Conversion*, Vol. 18, No. 4, December 2003, pp. 516–524.

[26] http://www.emtp-software.com/

[27] IEEE Std. C37.102, "IEEE Guide for AC Generator Protection," 2006.

[28] C.J. Mozina, M. Reichard, Z. Bukhala, "Coordination of Generator Protection with Generator Excitation Control and Generator Capability," Working Group J-5 of the Rotating Machinery Subcommittee of the Power System Relay Committee, in *Proc. IEEE Power Engineering Society General Meeting*, Tampa, USA, June 2007, pp. 1-17.

APPENDIX A

DATA OF THE SYSTEM UNDER STUDY

A.1 Synchronous Generator

Table A.1: Synchronous generator data.

Rating, MVA	700
Rated voltage, kV	22
Armature resistance, r_a, p.u.	0.0045
Leakage reactance, x_l, p.u.	0.12
Direct-axis synchronous reactance, x_d, p.u.	1.54
Quadrature-axis synchronous reactance, x_q, p.u.	1.50
Direct-axis transient reactance, x'_d, p.u.	0.23
Quadrature-axis transient reactance, x'_q, p.u.	0.42
Direct-axis subtransient reactance, x''_d, p.u.	0.18
Quadrature-axis subtransient reactance, x''_q, p.u.	0.18
Direct-axis transient open-circuit time constant, T'_{do}, s	3.70
Quadrature-axis transient open-circuit time constant, T'_{qo},s	0.43
Direct-axis subtransient open-circuit time constant, T''_{do}, s	0.04
Quadrature-axis subtransient open-circuit time constant, T''_{qo},s	0.06
Zero-sequence reactance, x_o, p.u.	0.36
Inertia constant, M, p.u.	2625.22013

A.2 DFIG-based Wind Farm

Table A.2: Wind farm parameters.

Number of wind turbine generators	400
System frequency, Hz	60
Rated capacity of each wind farm generator, MVA	1.67
Rated capacity of turbine, MW	1.5
Generator rated voltage, kV	0.575
DC nominal voltage, V	1150
Number of poles	6
Average wind speed, m/s	11.24

A.3 FFC-based Wind Farm

Table A.3: Wind farm parameters.

Number of wind turbine generators	100
System frequency, Hz	60
Rated capacity of each wind farm generator, MVA	2.222
Rated capacity of turbine, MW	2.0
Generator rated voltage, kV	0.575
DC nominal voltage, V	1150
Number of poles	6
Average wind speed, m/s	15

A.4 Transformers

Table A.4: Transformer data.

	T_1(Generator)	T_2(DFIG-based Wind Farm)	T_3(FFC-based Wind Farm)
Rating, MVA	700	750	225
Rated voltage, kV	22/500	34.5/500	34.5/500
Resistance, r_T, p.u.	0.0012	0.005	0.005
Leakage reactance, x_T, p.u.	0.12	0.15	0.125

A.5 Transmission Lines

All transmission lines have the same series impedance and shunt admittance per unit length.

$Z_{T.L.series} = (0.0118 + j0.3244)\Omega/km$

$Y_{T.L.shunt} = 5.0512\ \mu S/km$

Transmission voltage = 500 kV

A.6 Excitation System

Table A.5: Excitation system data.

$K_A = 2$	$K_E = 1.0$
$K_{FE} = 0.03$	$T_A = 0.04$ s
$T_{FE} = 1.0$ s	$T_E = 0.01$s
Lim_max= 4.75 p.u.	*Lim_min*= -4.75 p.u.

APPENDIX B

CALCULATIONS OF RELAY (21) REACH

1. 120% of the longest line with system infeed currents:

The equivalent circuit of the system under study with infeed current is shown in Figure B.1.

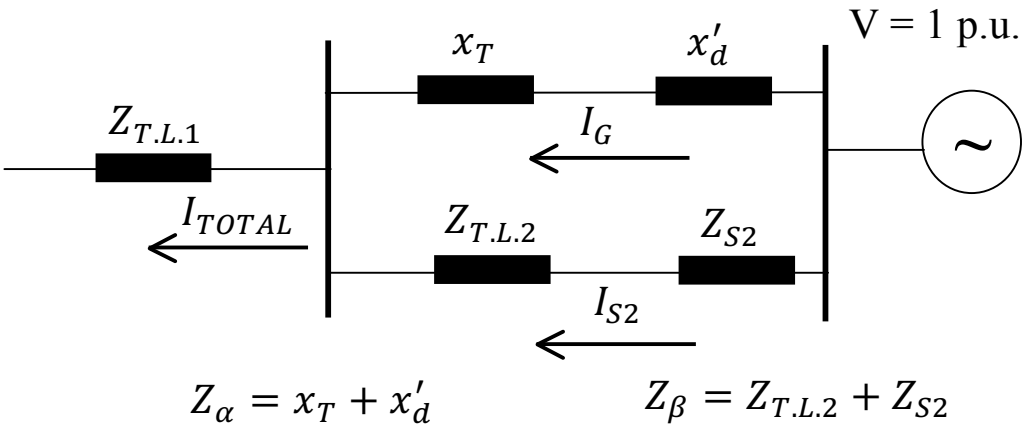

Figure B.1: Calculation of the infeed current for the study system.

Transmission lines: 500 kV, $Z_{T.L.1}$= 0.32461 ∠87.917°Ω/km (B.1)

L_1: 400 km, $Z_{T.L.1}$= 129.844 ∠87.917°Ω (B.2)

$$Z_{S_2} = 5 + j35\ \Omega = 35.3553\angle 81.8699^\circ\ \Omega \quad \text{(B.3)}$$

$$Z_{T.L.2} = 64.922\angle 87.917^\circ\ \Omega \quad \text{(B.4)}$$

$$Z_{T.L.BASE} = \frac{(500)^2}{700} = 357.1429\ \Omega \quad \text{(B.5)}$$

$$Z_{T.L.1} = 0.3636\angle 87.917^\circ\ \text{p.u.} \quad \text{(B.6)}$$

$$Z_{T.L.2} = 0.1818\angle 87.917^\circ\ \text{p.u.} \quad \text{(B.7)}$$

$$Z_{S2} = 0.099\angle 81.8699^\circ\ \text{p.u.} \quad \text{(B.8)}$$

$$Z_\alpha = x_T + x'_d = 0.37\angle 90^\circ\ \text{p.u.} \quad \text{(B.9)}$$

$$Z_\beta = Z_{T.L.2} + Z_{S2} = 0.2804\angle 85.7858^\circ\ \text{p.u.} \quad \text{(B.10)}$$

$$Z_{TOTAL} = 0.5232\angle 87.8211^\circ\ \text{p.u.} \quad \text{(B.11)}$$

$$I_{TOTAL} = 1.9112\angle -87.8211^\circ\ \text{p.u.} \quad \text{(B.12)}$$

$$I_{S2} = I_{TOTAL}\frac{Z_\alpha}{Z_\alpha + Z_\beta} \tag{B.13}$$

$$I_G = I_{TOTAL}\frac{Z_\beta}{Z_\alpha + Z_\beta} \tag{B.14}$$

$$\frac{I_{S2} + I_G}{I_G} = \frac{Z_\alpha + Z_\beta}{Z_\beta} = 2.318\angle 2.3975^\circ \tag{B.15}$$

$$\left|\frac{I_{S2} + I_G}{I_G}\right| = 2.318 \tag{B.16}$$

$$I_{Generator\_base} = \frac{700\times10^6}{\sqrt{3}\times22\times10^3} = 18370\ A \tag{B.17}$$

$$R_C = \frac{18370\times1.25}{5} = 4592 \tag{B.18}$$

$$V_{Ph\_GEN} = \frac{22\times10^3}{\sqrt{3}} = 12702.7059\ V \tag{B.19}$$

$$R_v = \frac{12702.7059}{67} = 190 \tag{B.20}$$

$$Z_{base\_relay} = \frac{(kV_{Gen-Base})^2}{700}\times\frac{R_C}{R_v} = \frac{22^2}{700}\times\frac{4592}{190} = 16.7128\ \Omega \tag{B.21}$$

$$Z_{21} = [0.12 + (1.2\times2.3228\times0.36357)]\times16.7128 = 18.9425\ \Omega \tag{B.22}$$

2. 50% to 67% of the generator load impedance (Z_{load}) at the rated power factor angle (RPFA) of the generator:

$$Z_{Max\_loading\_at\_RPF} = \frac{22^2}{700}\times\frac{4592}{190} = 16.71\ \Omega \tag{B.23}$$

At 67% :

$$Z_{21\_67\%} = 0.67\times\frac{16.71}{\cos(85^\circ - 36.8699^\circ)} = 16.77\ \Omega \tag{B.24}$$

3. 90% of the generator load impedance at the maximum torque angle:

$$Z_{21} = 0.9\times Z_{GCC_{MTA}} = 0.9\times\frac{22^2}{587.54}\times\frac{4592}{190} = 17.918\ \Omega \tag{B.25}$$

APPENDIX C

SETTING RELAY (21) ACCORDING TO 67% OF THE GENERATOR LOAD IMPEDANCE AT THE RATED POWER FACTOR ANGLE OF THE GENERATOR

C.1 Performance of Relay (21) during a three-phase fault at F_1

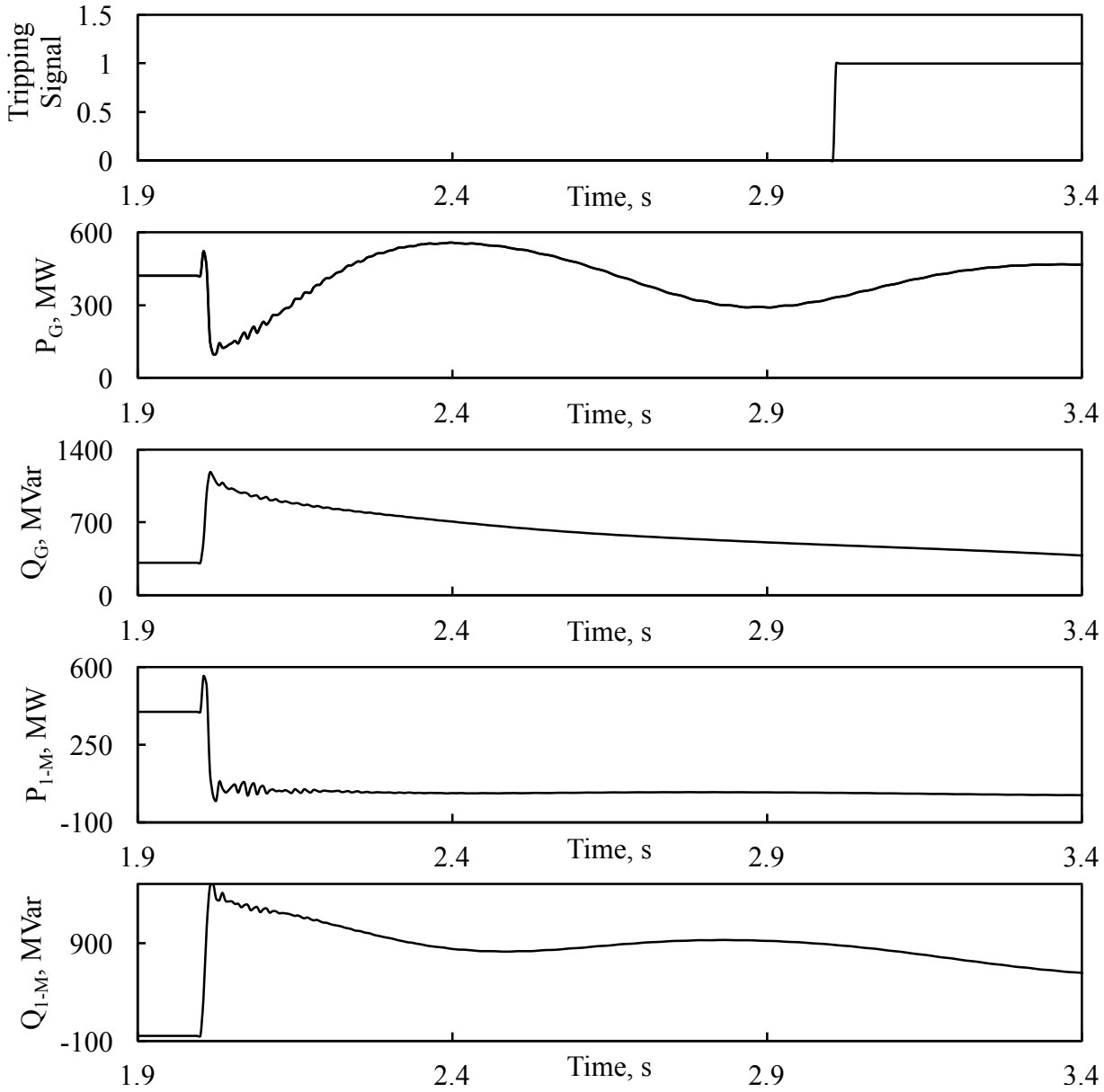

Figure C.1: Relay (21) tripping signal, transient time responses of generator active and reactive powers, active and reactive power flows from bus 1 to bus M during a three-phase fault at F_1 (no wind farm in the system, generator loading is 75%).

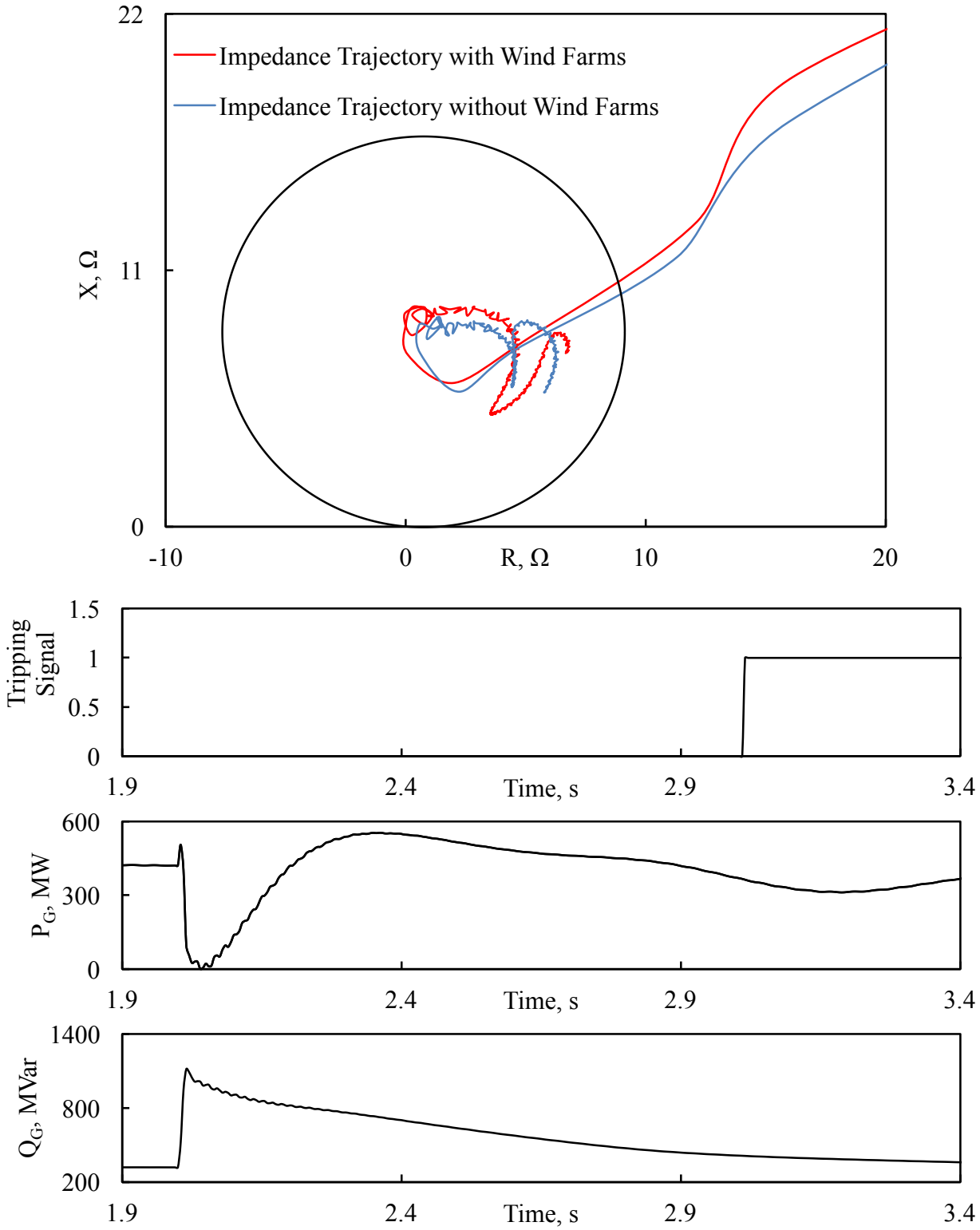

Figure C.2: Relay (21) measured impedance trajectory and its tripping signal, transient time responses of generator active and reactive powers, active and reactive power flows from bus 1 to bus M, DFIG- and FFC-based wind farm active and reactive powers during a three-phase fault at F_1 (generator loading is 75%).

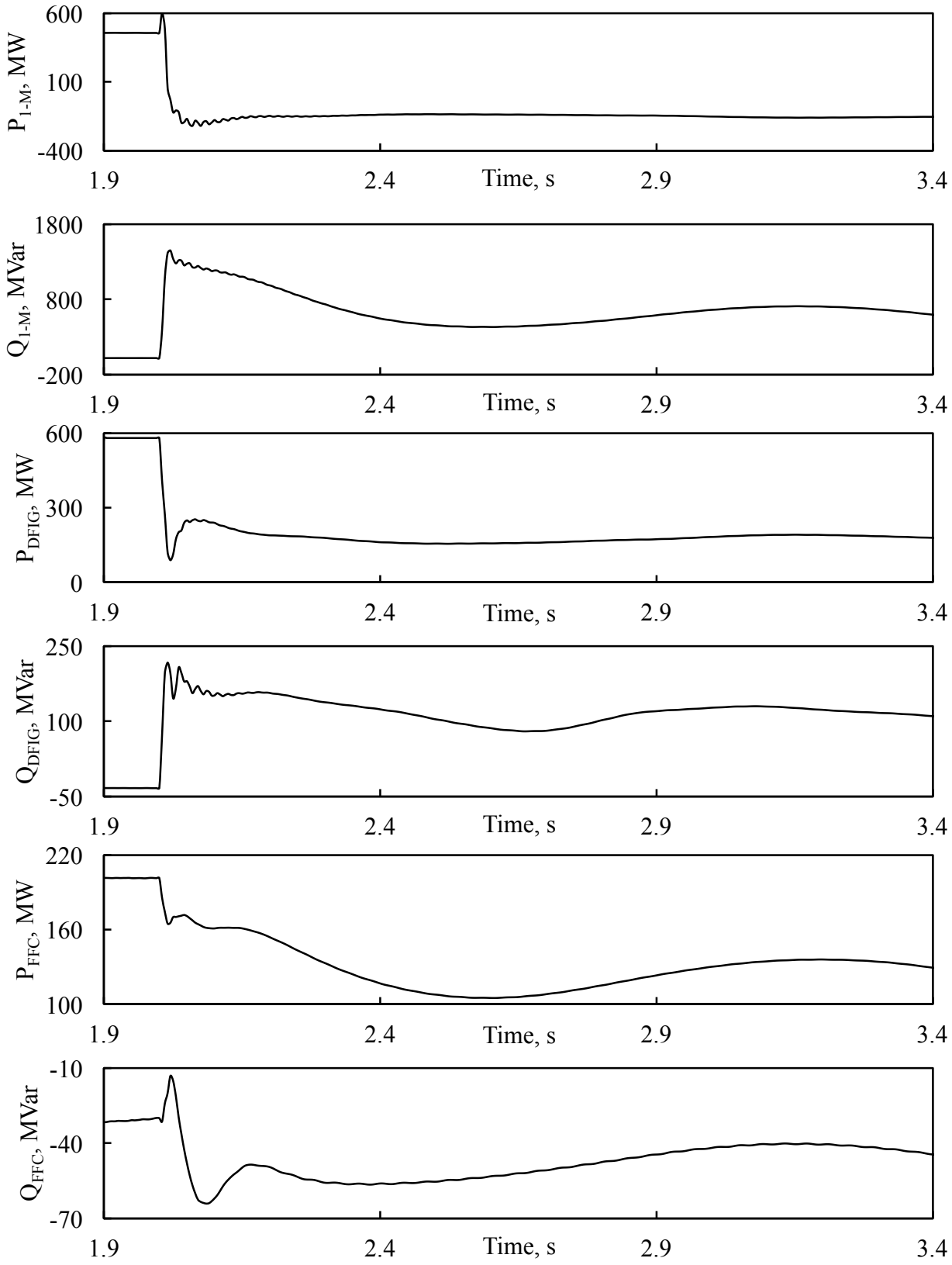

Figure C.2: Continued.

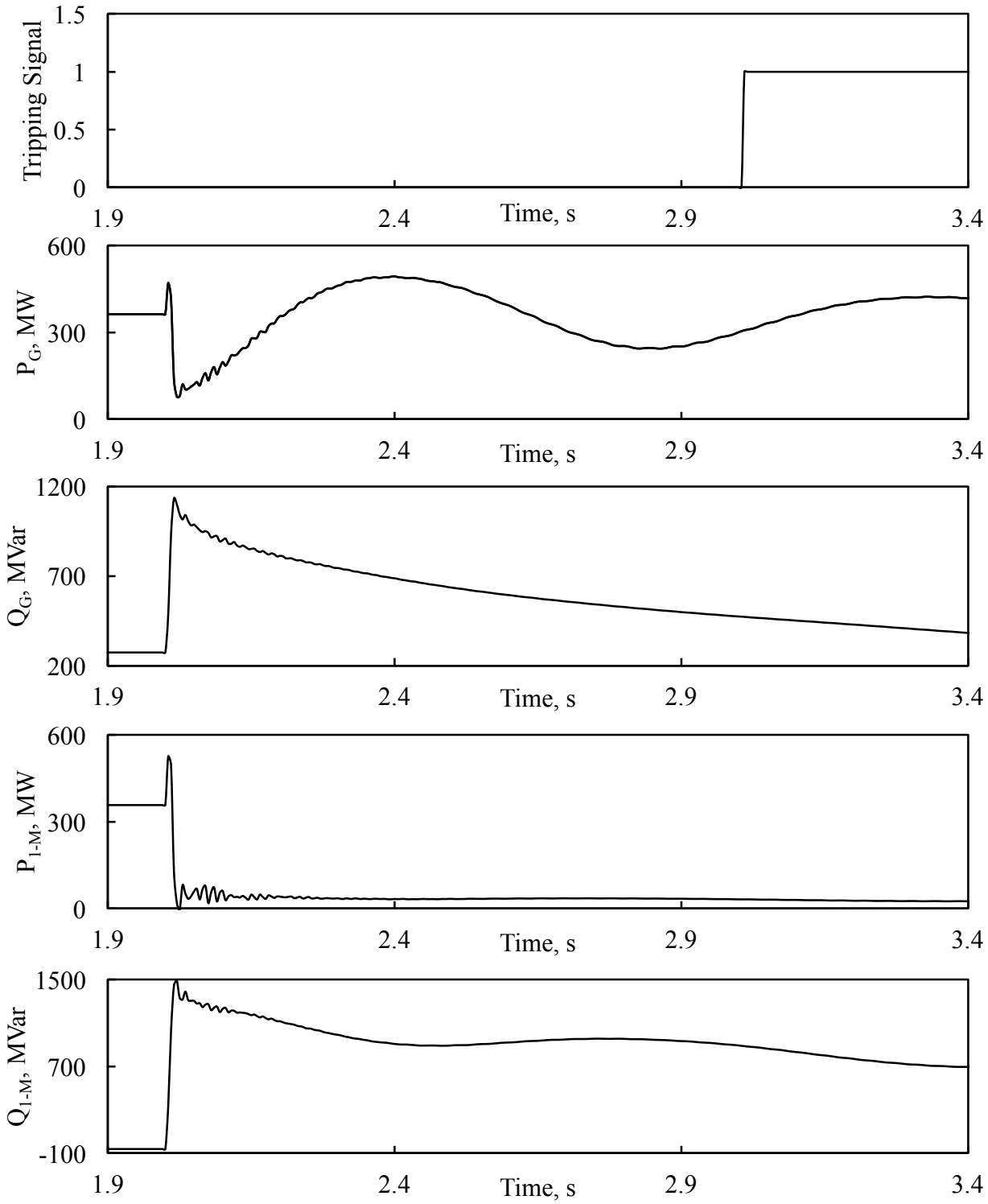

Figure C.3: Relay (21) tripping signal, transient time responses of generator active and reactive powers, active and reactive power flows from bus 1 to bus M during a three-phase fault at F_1 (no wind farm in the system, generator loading is 65%).

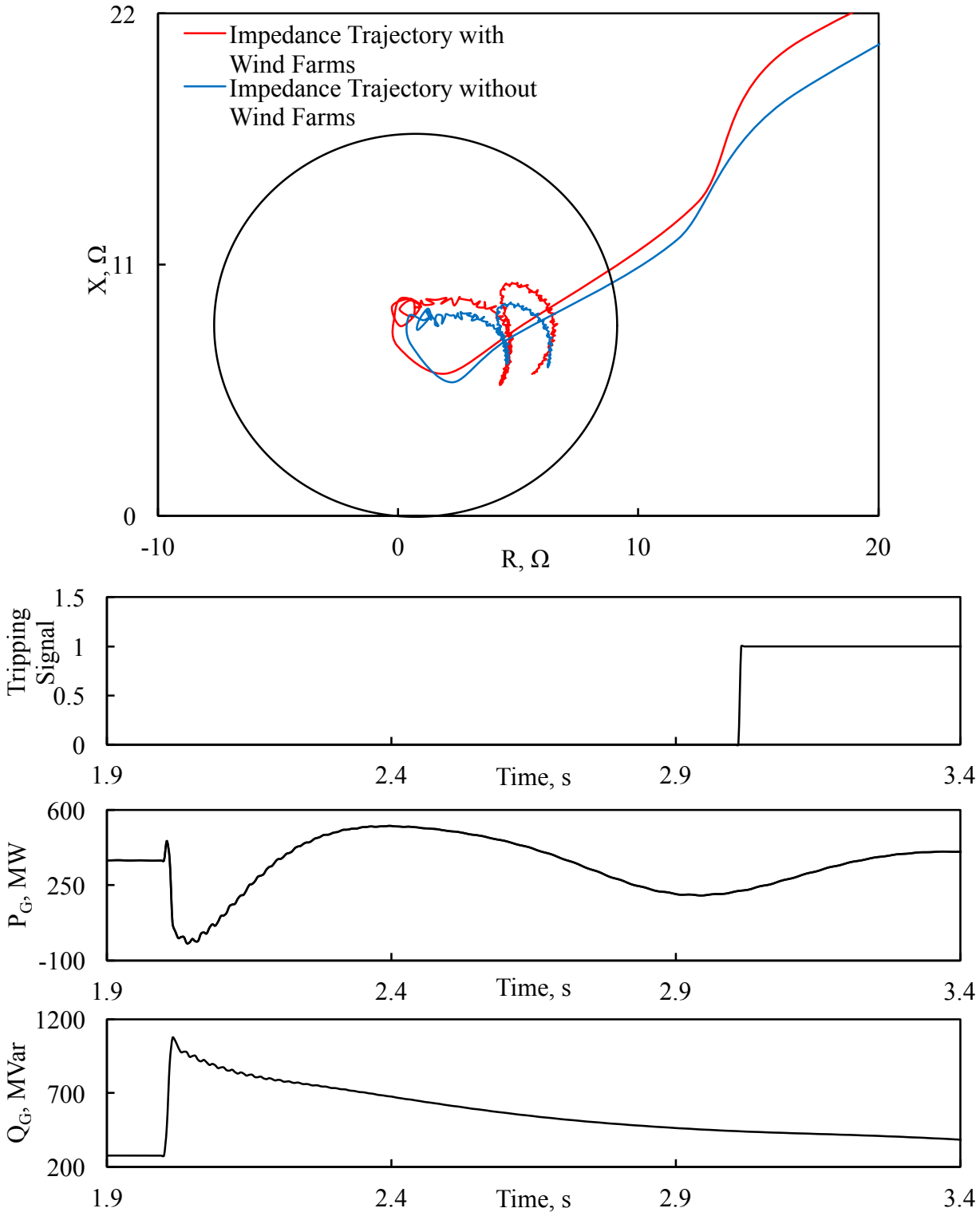

Figure C.4: Relay (21) measured impedance trajectory and its tripping signal, transient time responses of generator active and reactive powers, active and reactive power flows from bus 1 to bus M, DFIG- and FFC-based wind farm active and reactive powers during a three-phase fault at F_1 (generator loading is 65%).

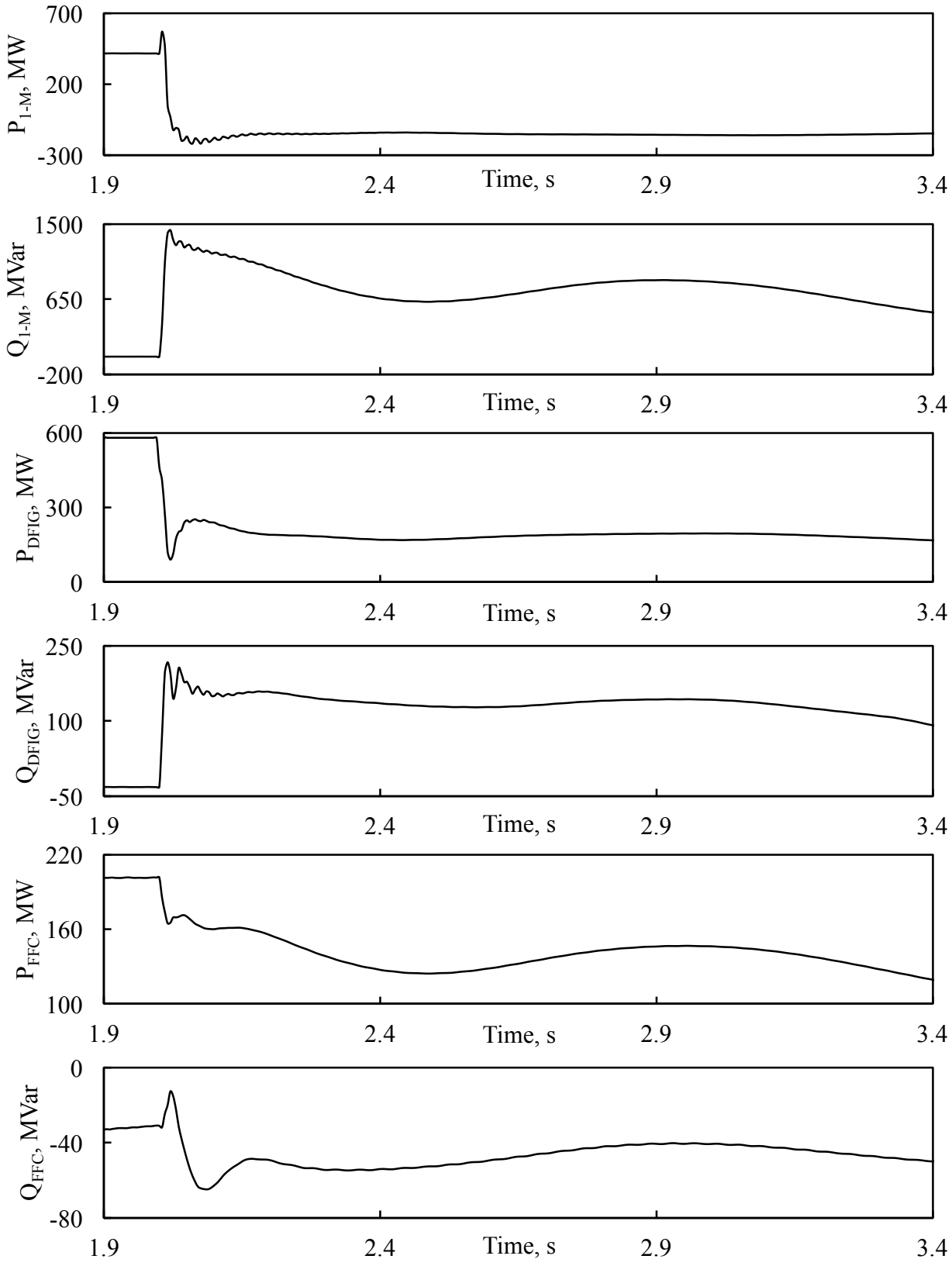

Figure C.4: Continued.

C.2 Performance of Relay (21) during a line-to-line fault at F_1

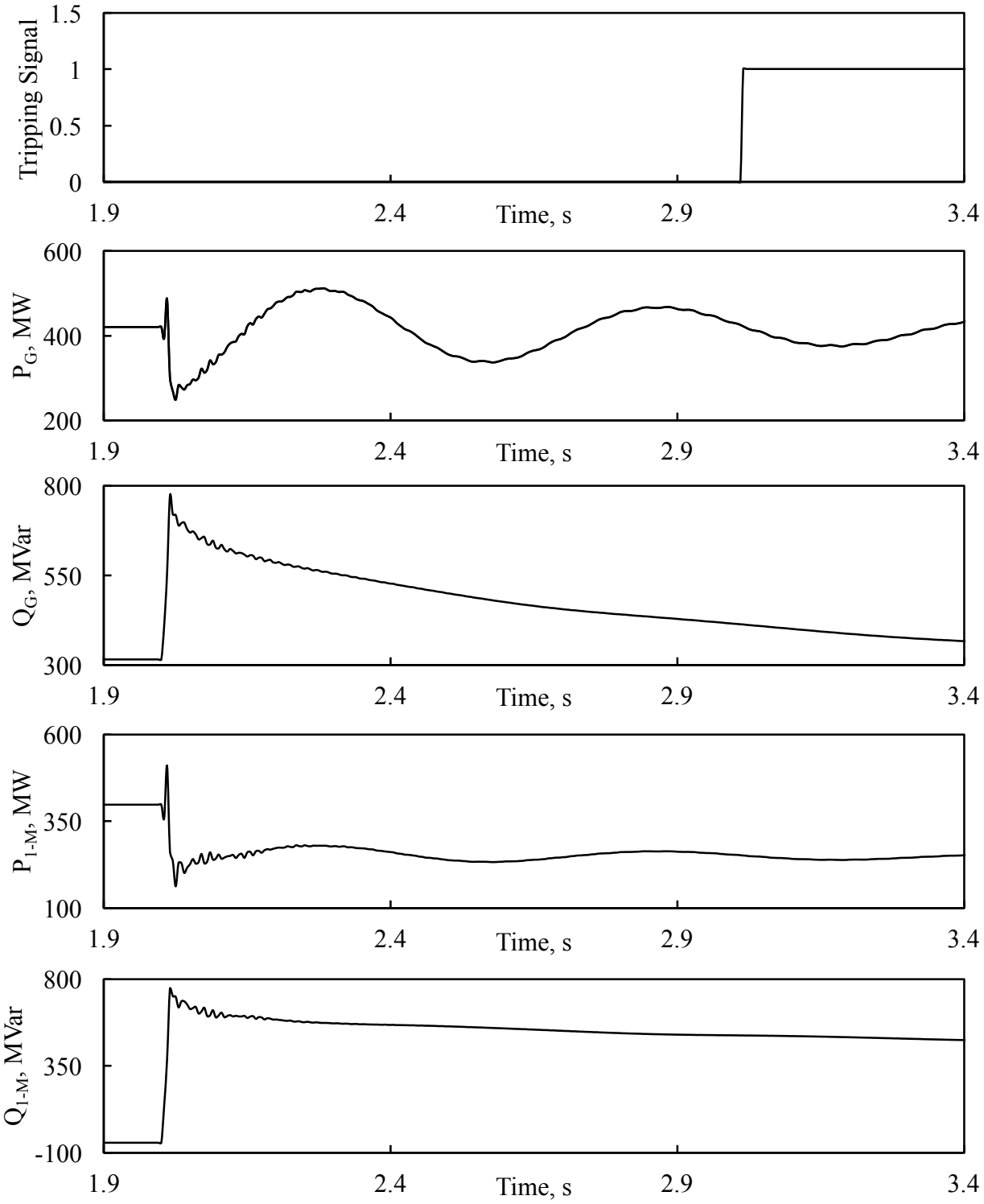

Figure C.5: Relay (21) tripping signal, transient time responses of generator active and reactive powers, active and reactive power flows from bus 1 to bus M during a line-to-line fault at F_1 (no wind farm in the system, generator loading is 75%).

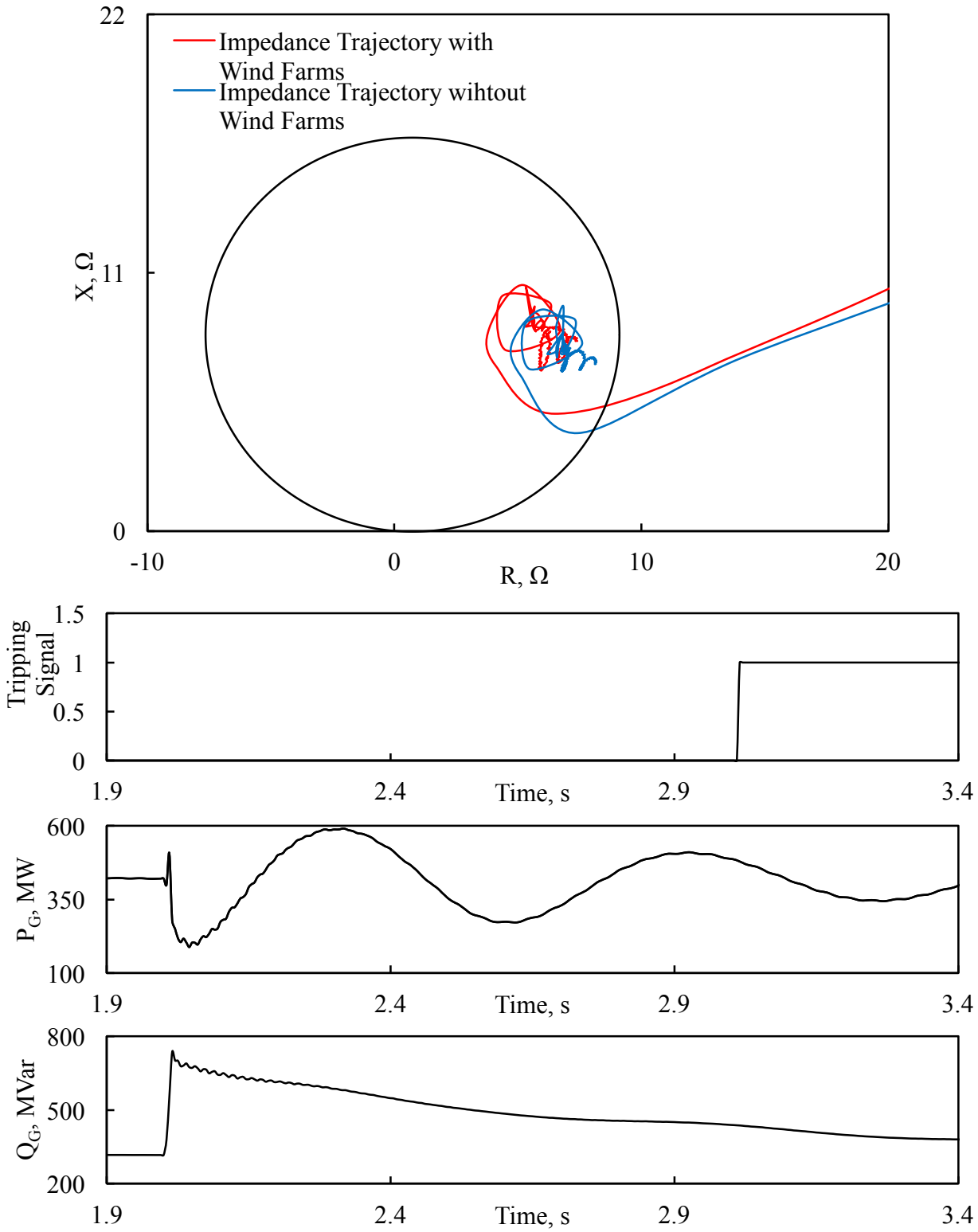

Figure C.6: Relay (21) measured impedance trajectory and its tripping signal, transient time responses of generator active and reactive powers, active and reactive power flows from bus 1 to bus M, DFIG- and FFC-based wind farm active and reactive powers during a line-to-line fault at F_1 (generator loading is 75%).

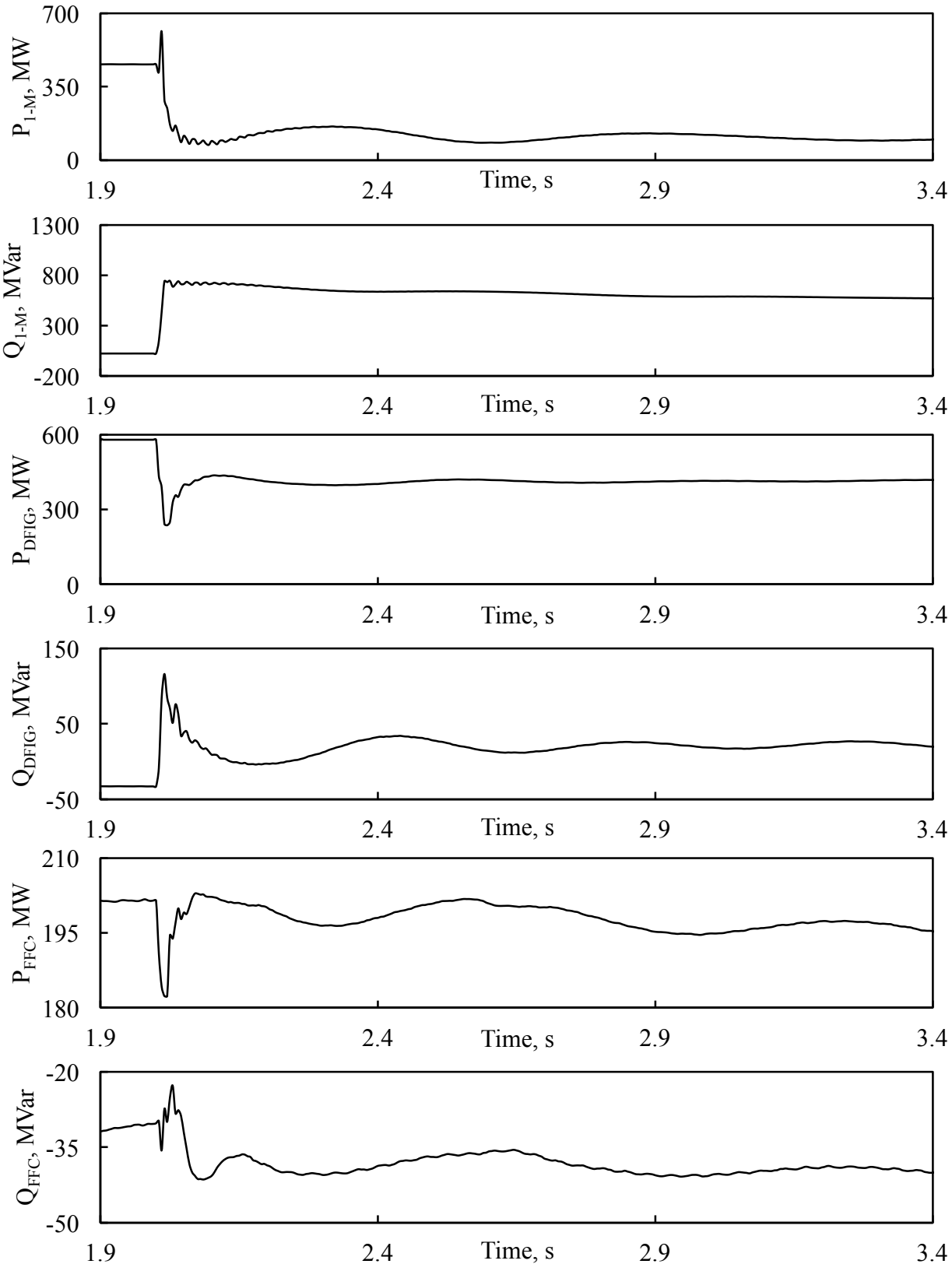

Figure C.6: Continued.

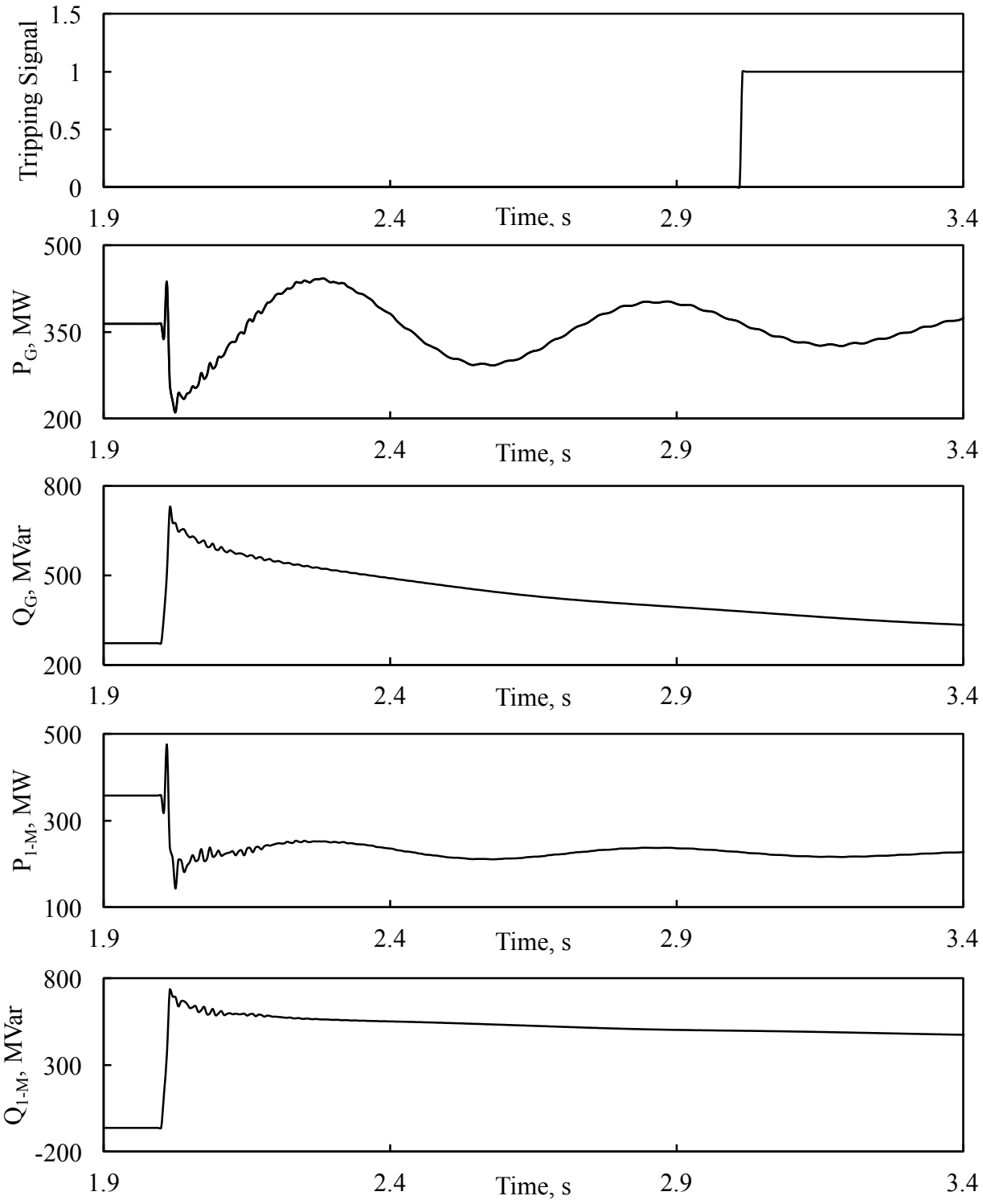

Figure C.7: Relay (21) tripping signal, transient time responses of generator active and reactive powers, active and reactive power flows from bus 1 to bus M during a line-to-line fault at F_1 (no wind farm in the system, generator loading is 65%).

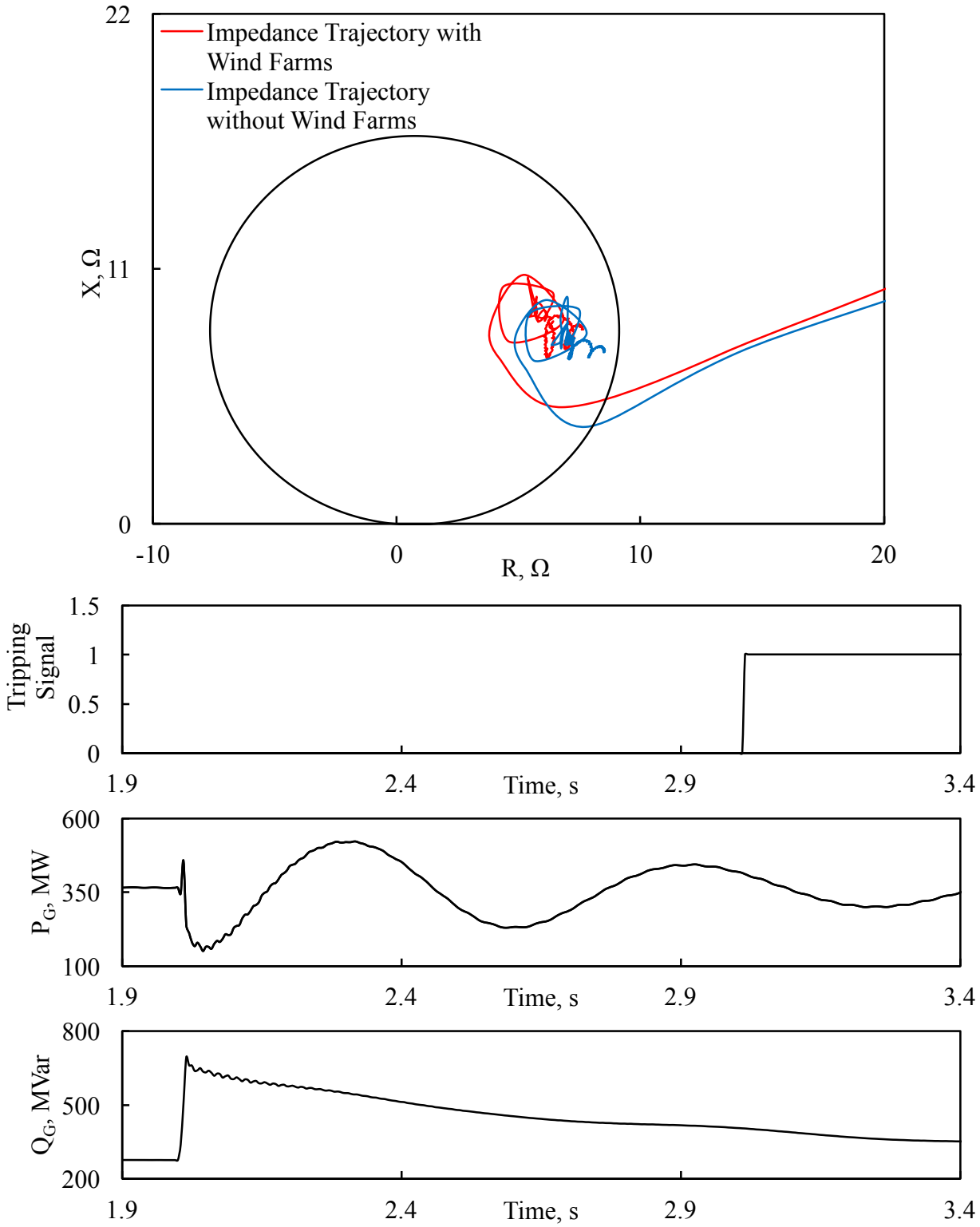

Figure C.8: Relay (21) measured impedance trajectory and its tripping signal, transient time responses of generator active and reactive powers, active and reactive power flows from bus 1 to bus M, DFIG- and FFC-based wind farm active and reactive powers during a line-to-line fault at F_1 (generator loading is 65%).

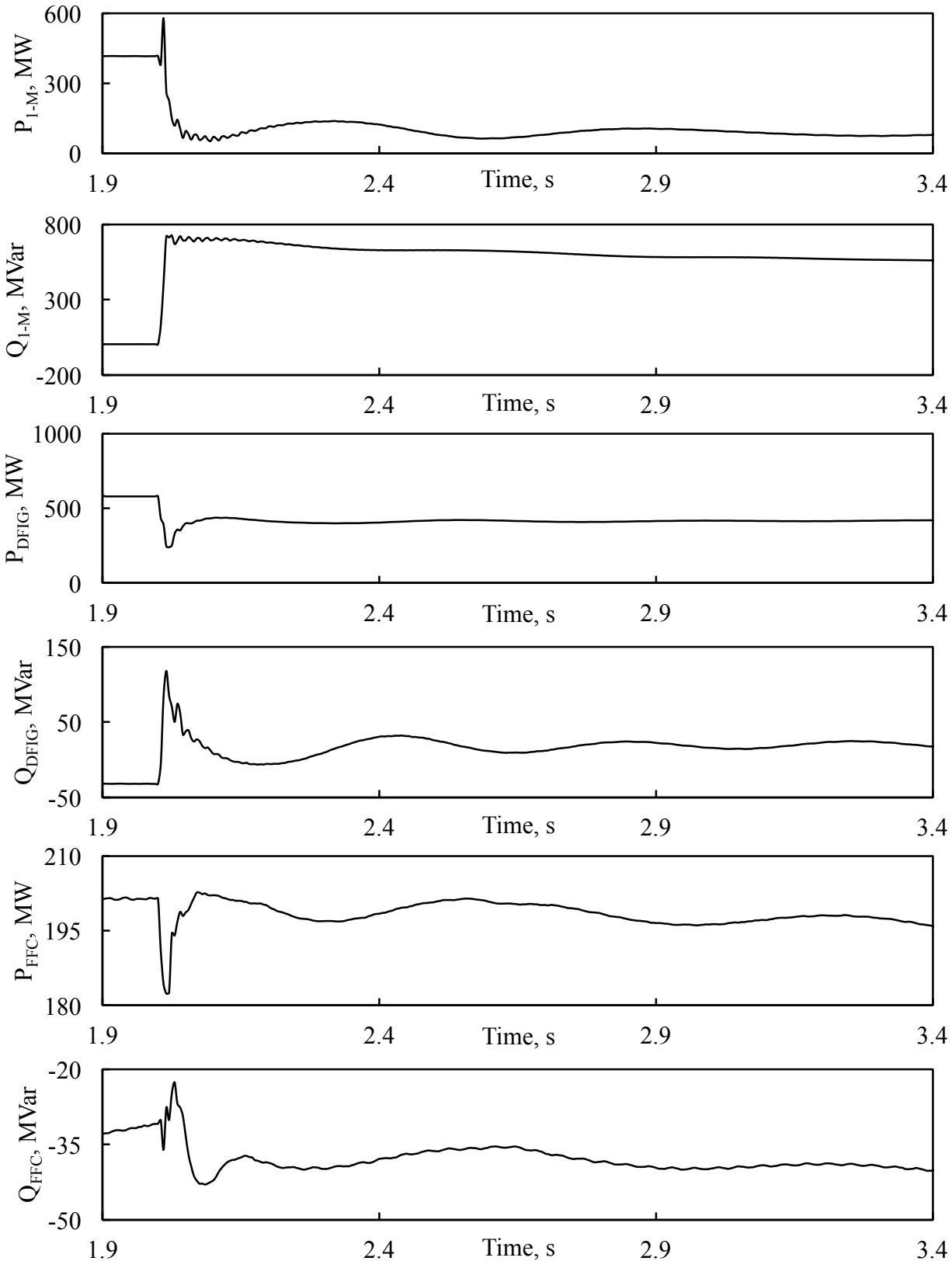

Figure C.8: Continued.

C.3 Performance of Relay (21) during a three-phase fault at F_2

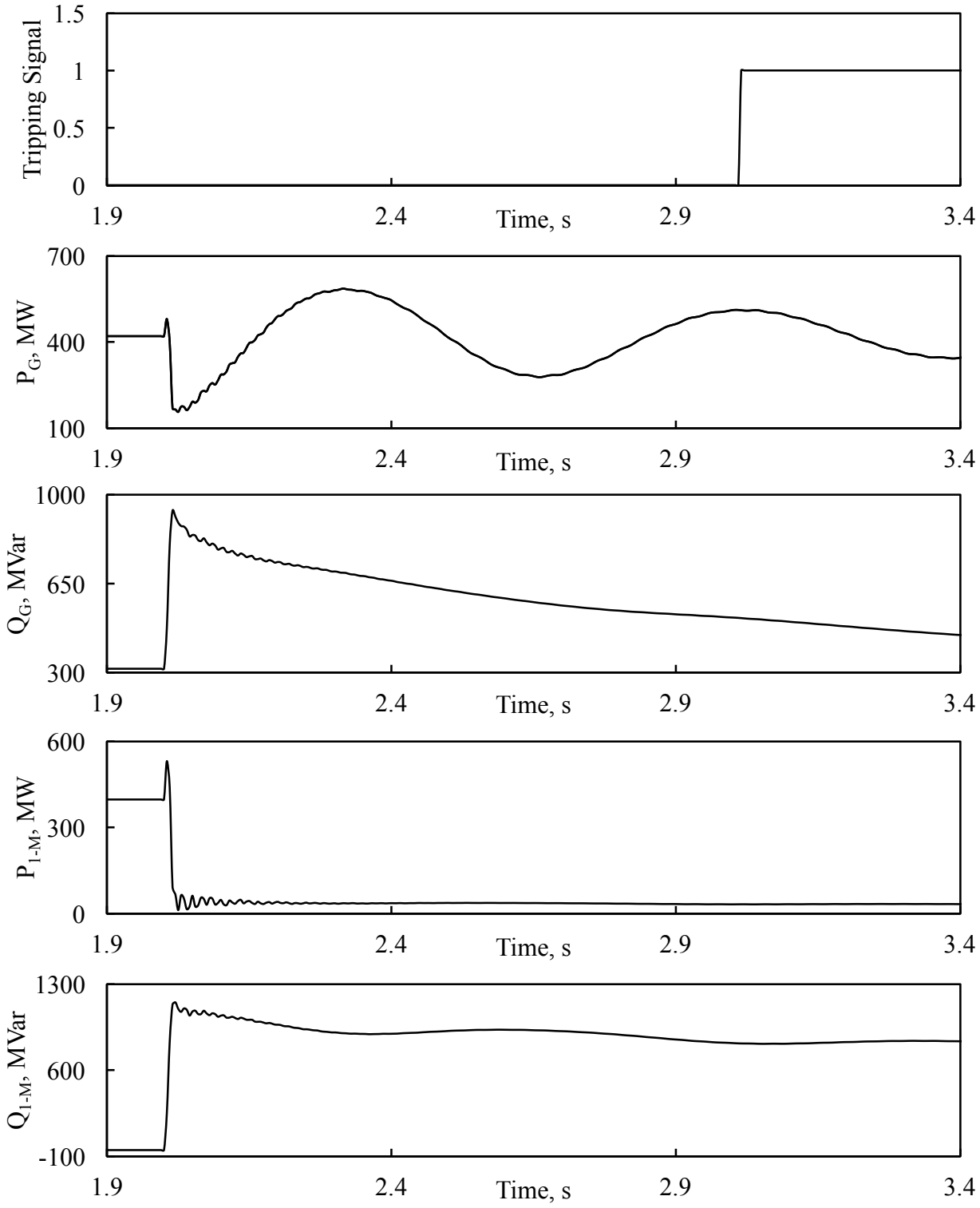

Figure C.9: Relay (21) tripping signal, transient time responses of generator active and reactive powers, active and reactive power flows from bus 1 to bus M during a three-phase fault at F_2 (no wind farm in the system, generator loading is 75%).

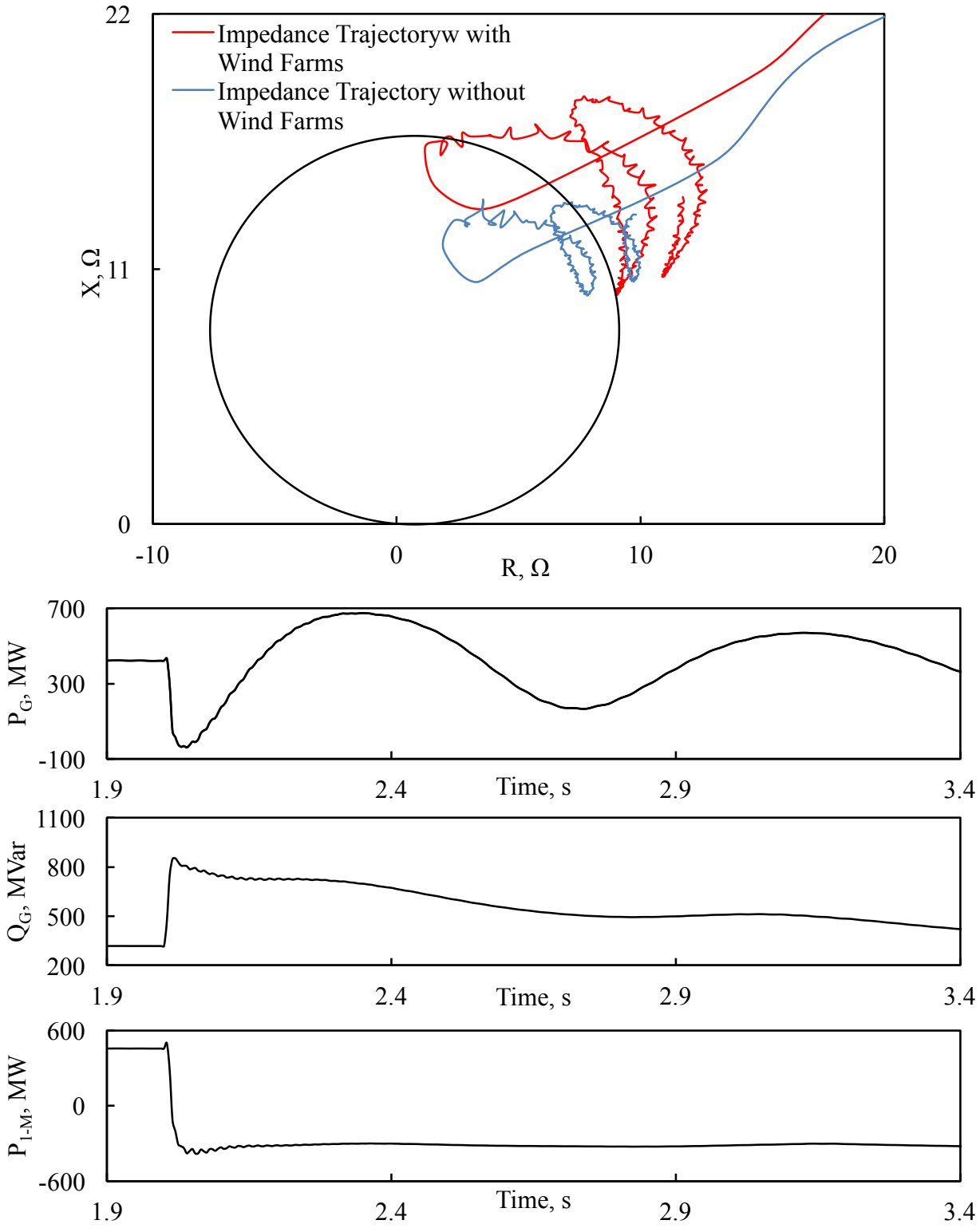

Figure C.10: Relay (21) measured impedance trajectory and its tripping signal, transient time responses of generator active and reactive powers, active and reactive power flows from bus 1 to bus M, DFIG- and FFC-based wind farm active and reactive powers during a three-phase fault at F_2 (generator loading is 75%).

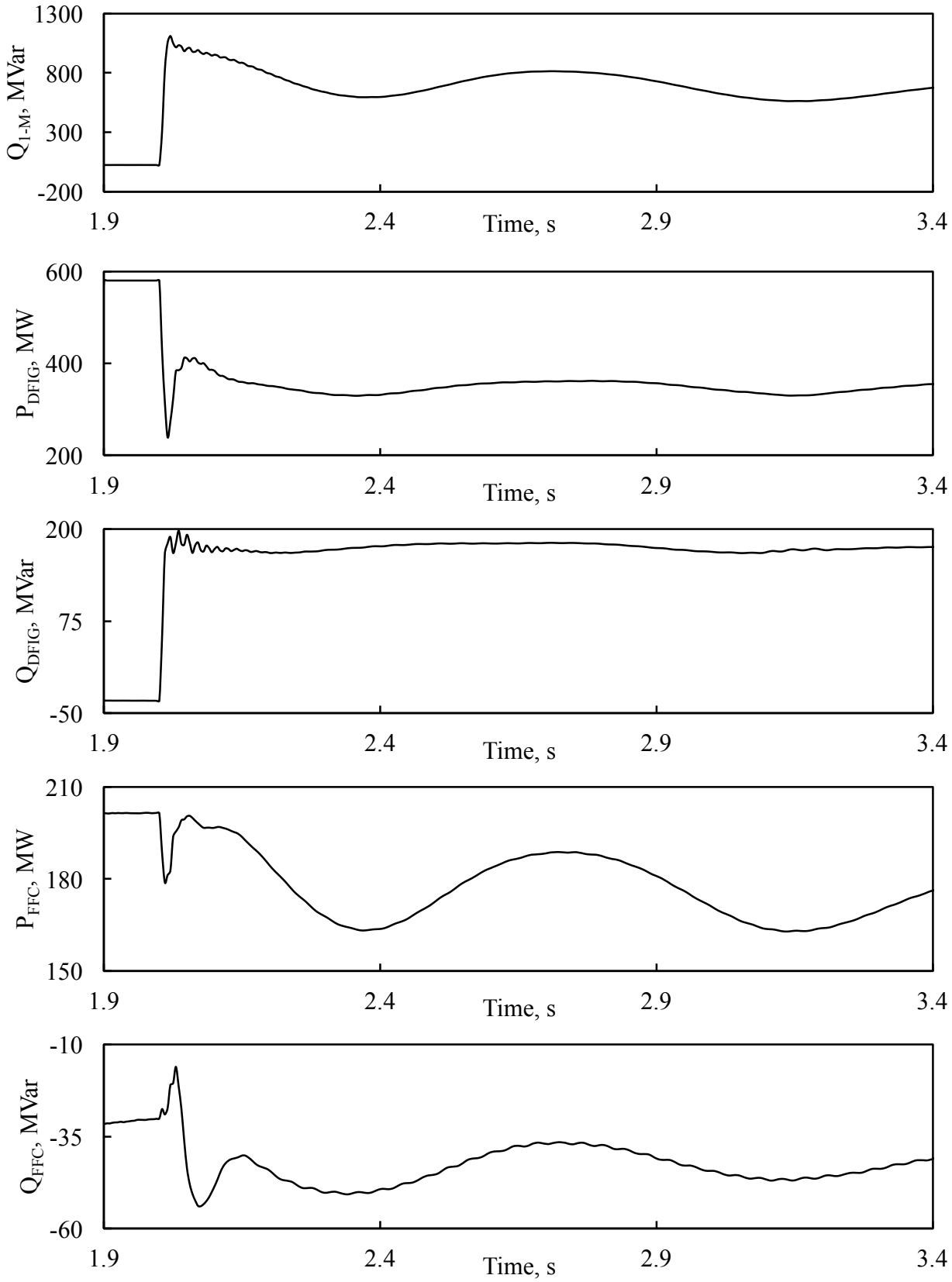

Figure C.10: Continued.

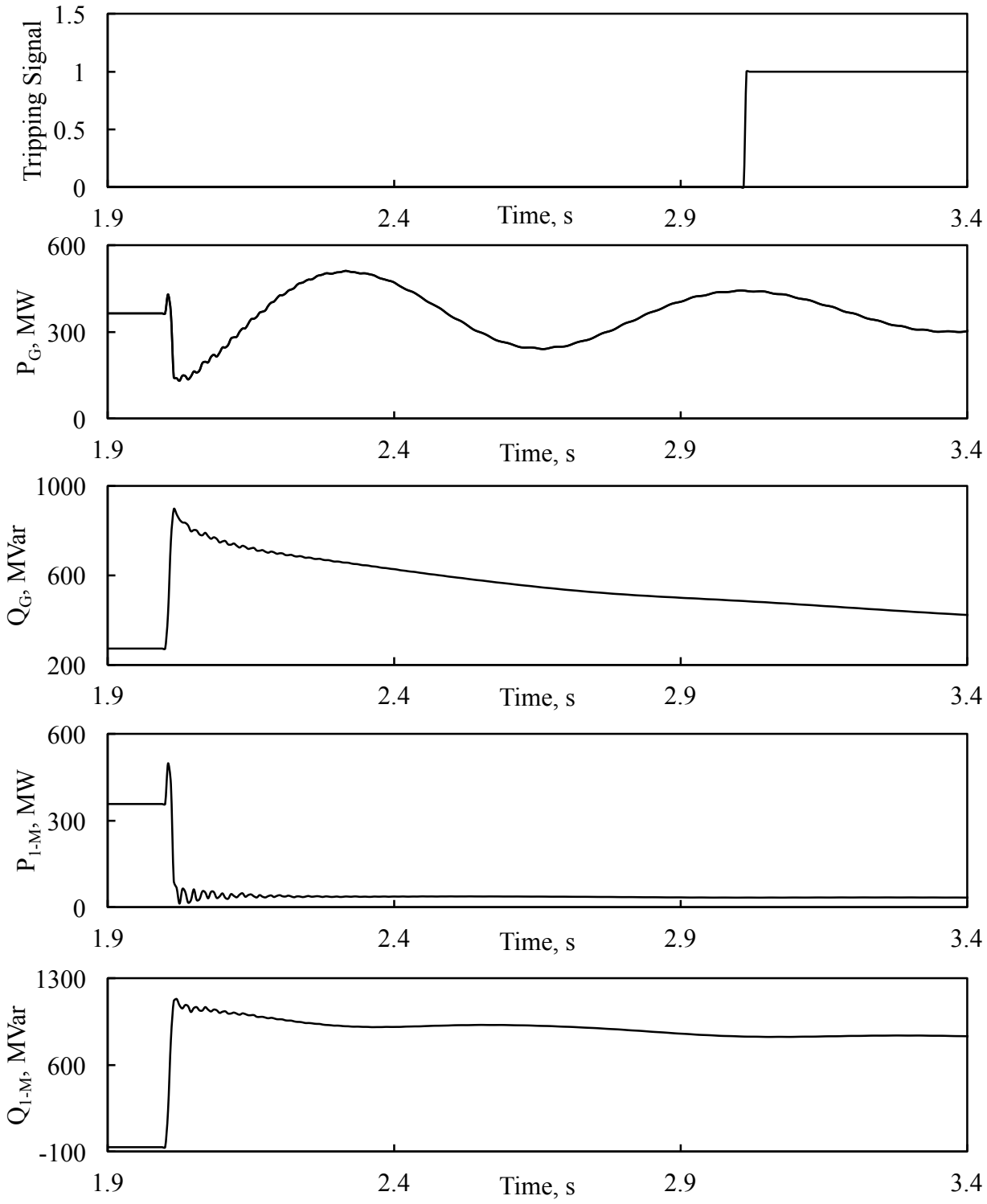

Figure C.11: Relay (21) tripping signal, transient time responses of generator active and reactive powers, active and reactive power flows from bus 1 to bus M during a three-phase fault at F_2 (no wind farm in the system, generator loading is 65%).

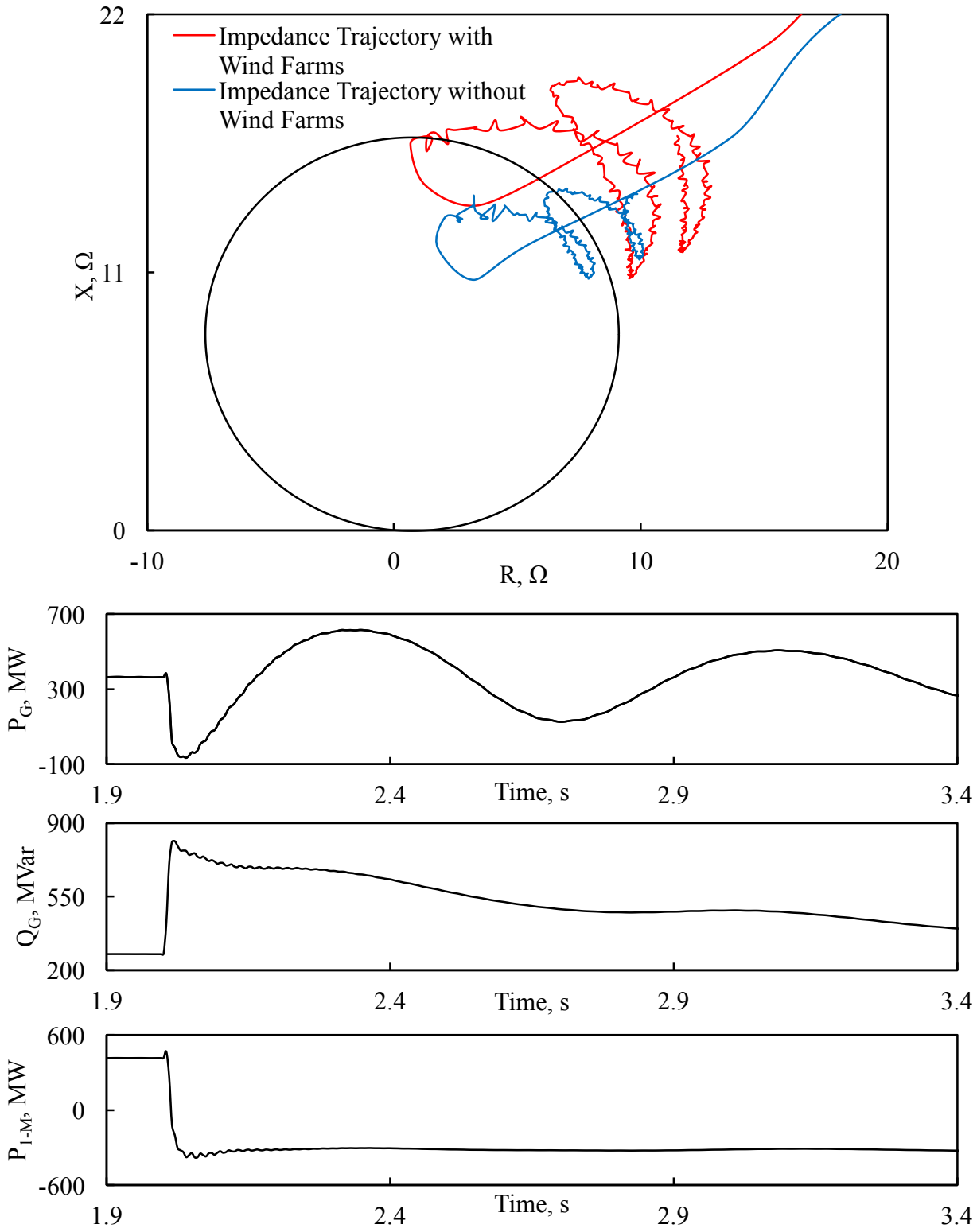

Figure C.12: Relay (21) measured impedance trajectory and its tripping signal, transient time responses of generator active and reactive powers, active and reactive power flows from bus 1 to bus M, DFIG- and FFC-based wind farm active and reactive powers during a three-phase fault at F_2 (generator loading is 65%).

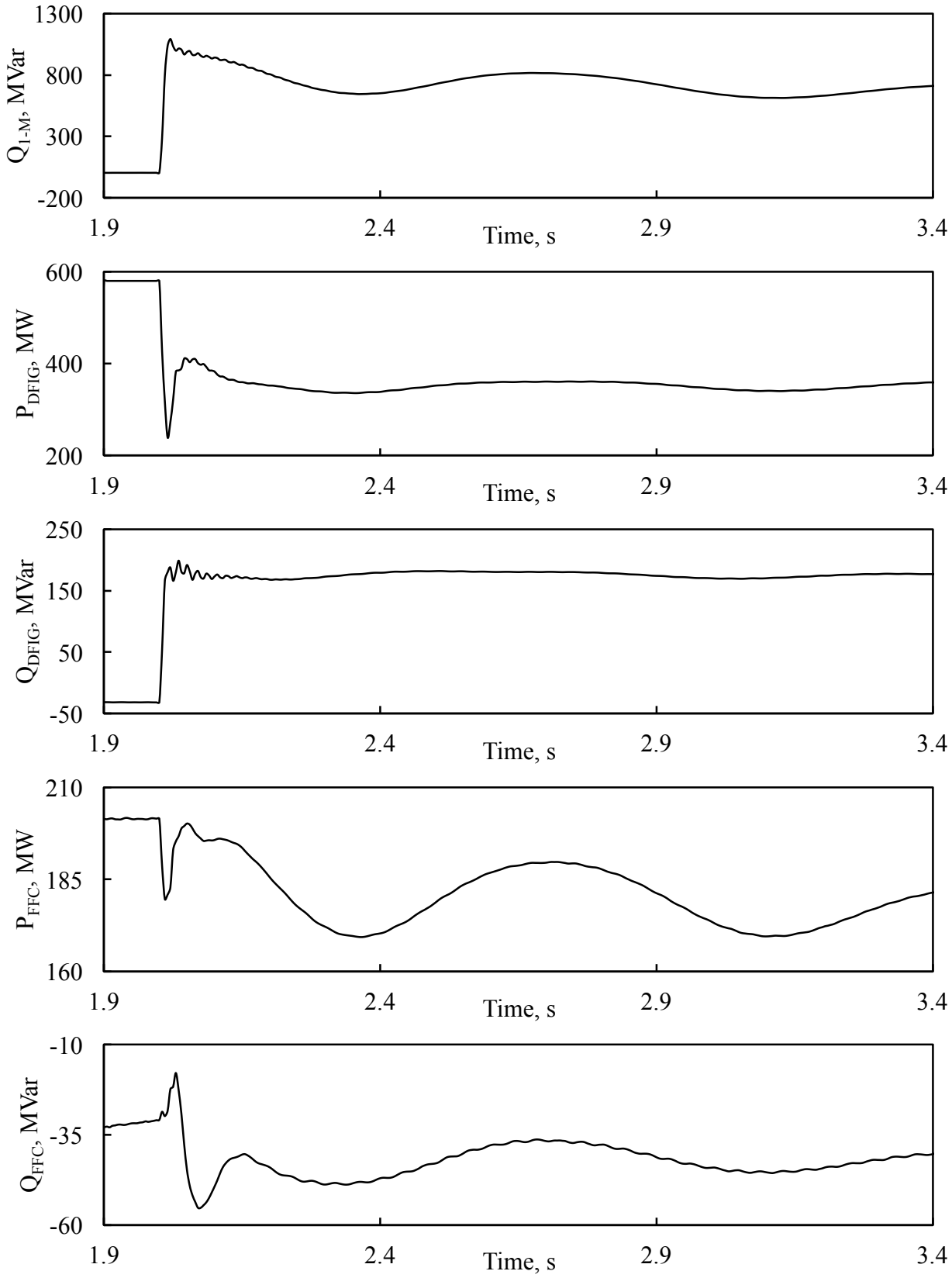

Figure C.12: Continued.

C.4 Performance of Relay (21) during a line-to-line fault at F_2

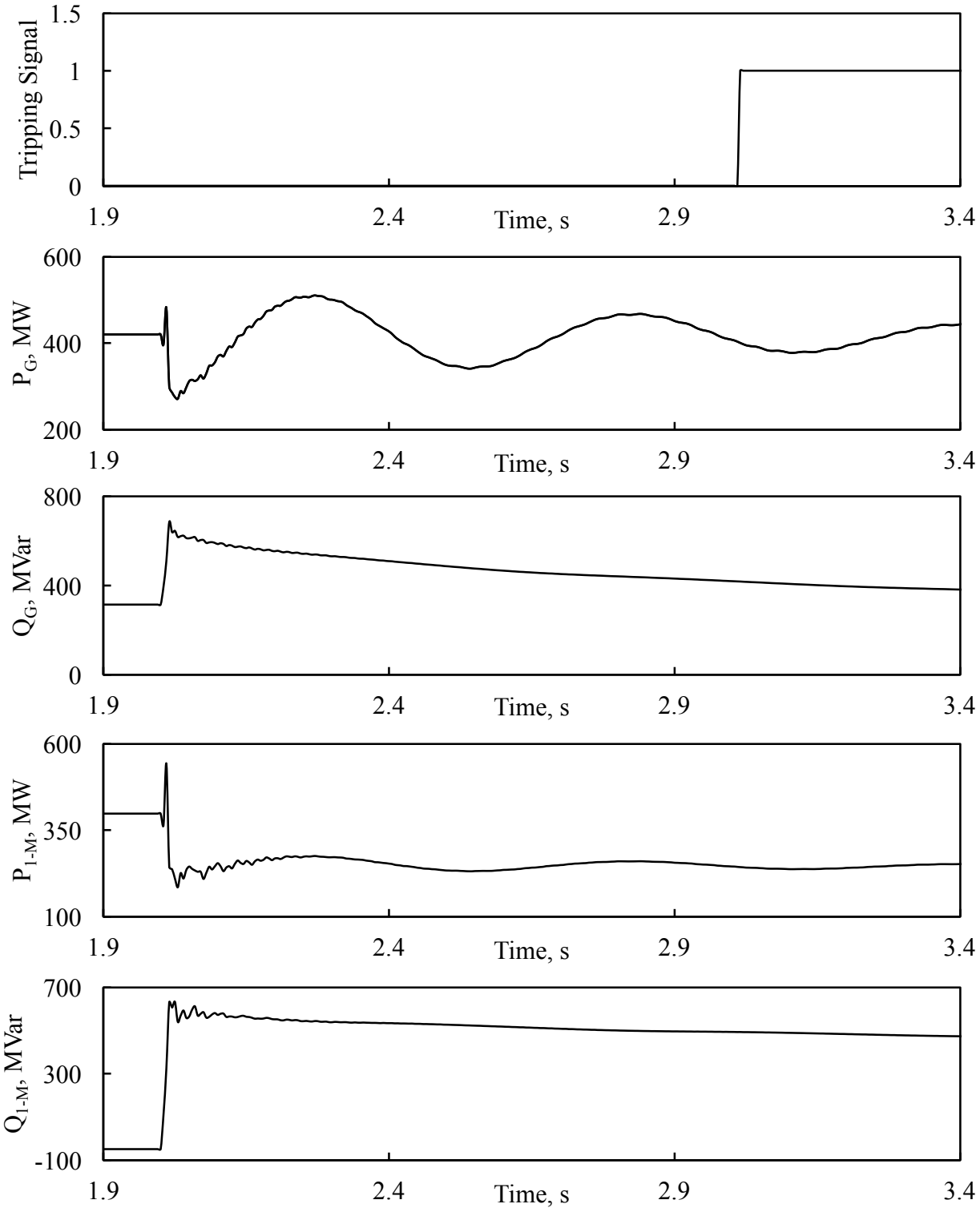

Figure C.13: Relay (21) tripping signal, transient time responses of generator active and reactive powers, active and reactive power flows from bus 1 to bus M during a line-to-line fault at F_2 (no wind farm in the system, generator loading is 75%).

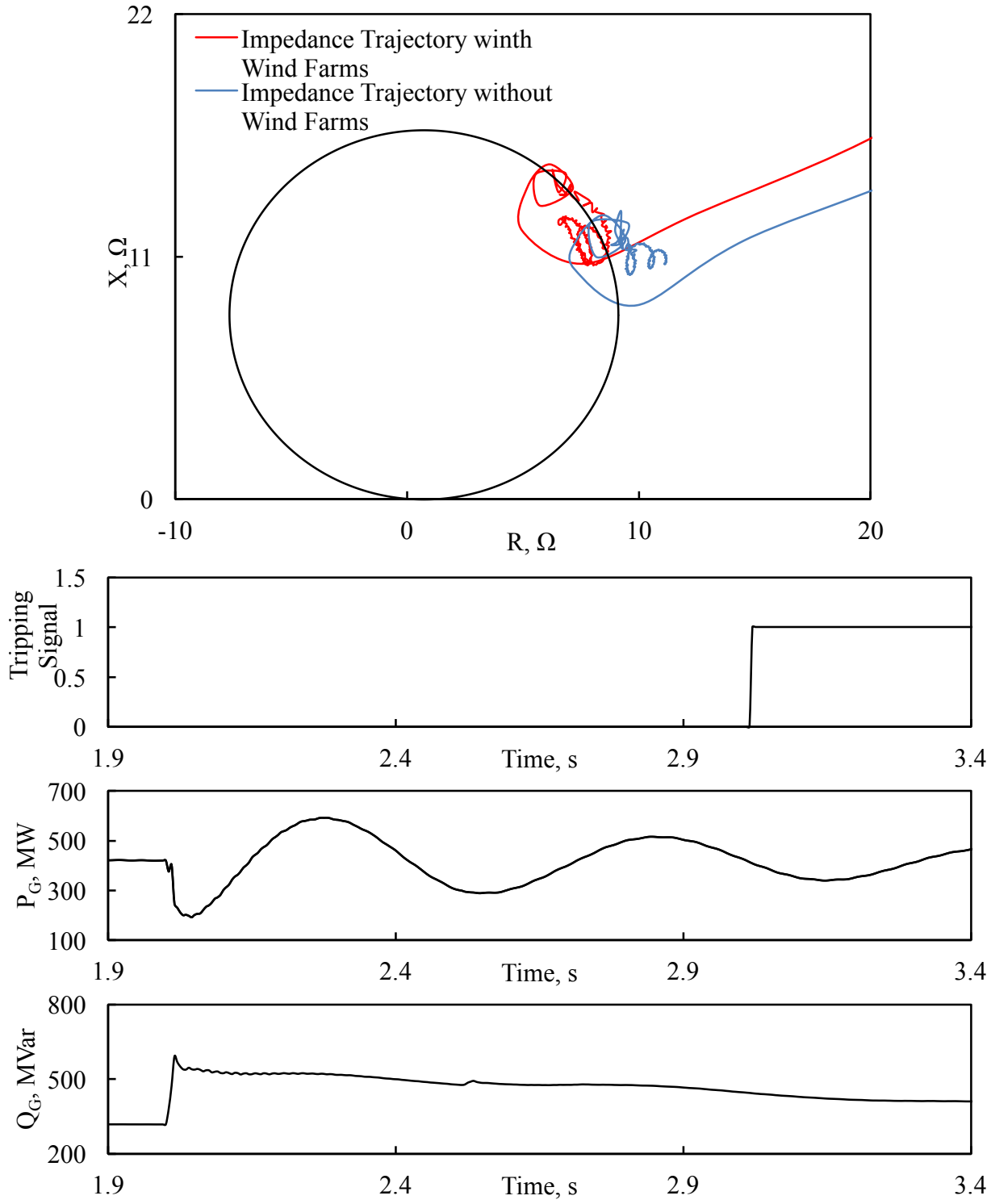

Figure C.14: Relay (21) measured impedance trajectory and its tripping signal, transient time responses of generator active and reactive powers, active and reactive power flows from bus 1 to bus M, DFIG- and FFC-based wind farm active and reactive powers during a line-to-line fault at F_2 (generator loading is 75%).

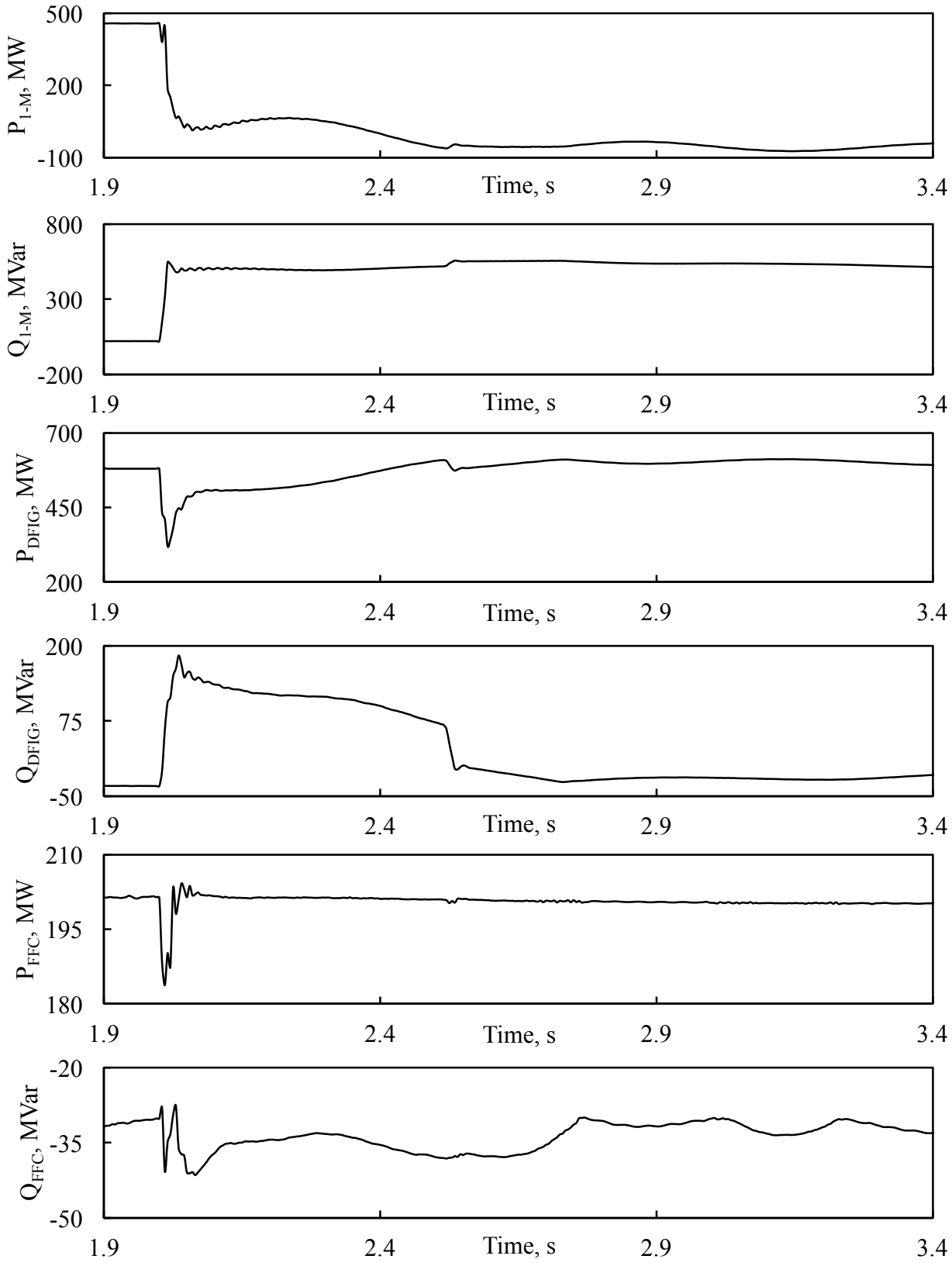

Figure C.14: Continued.

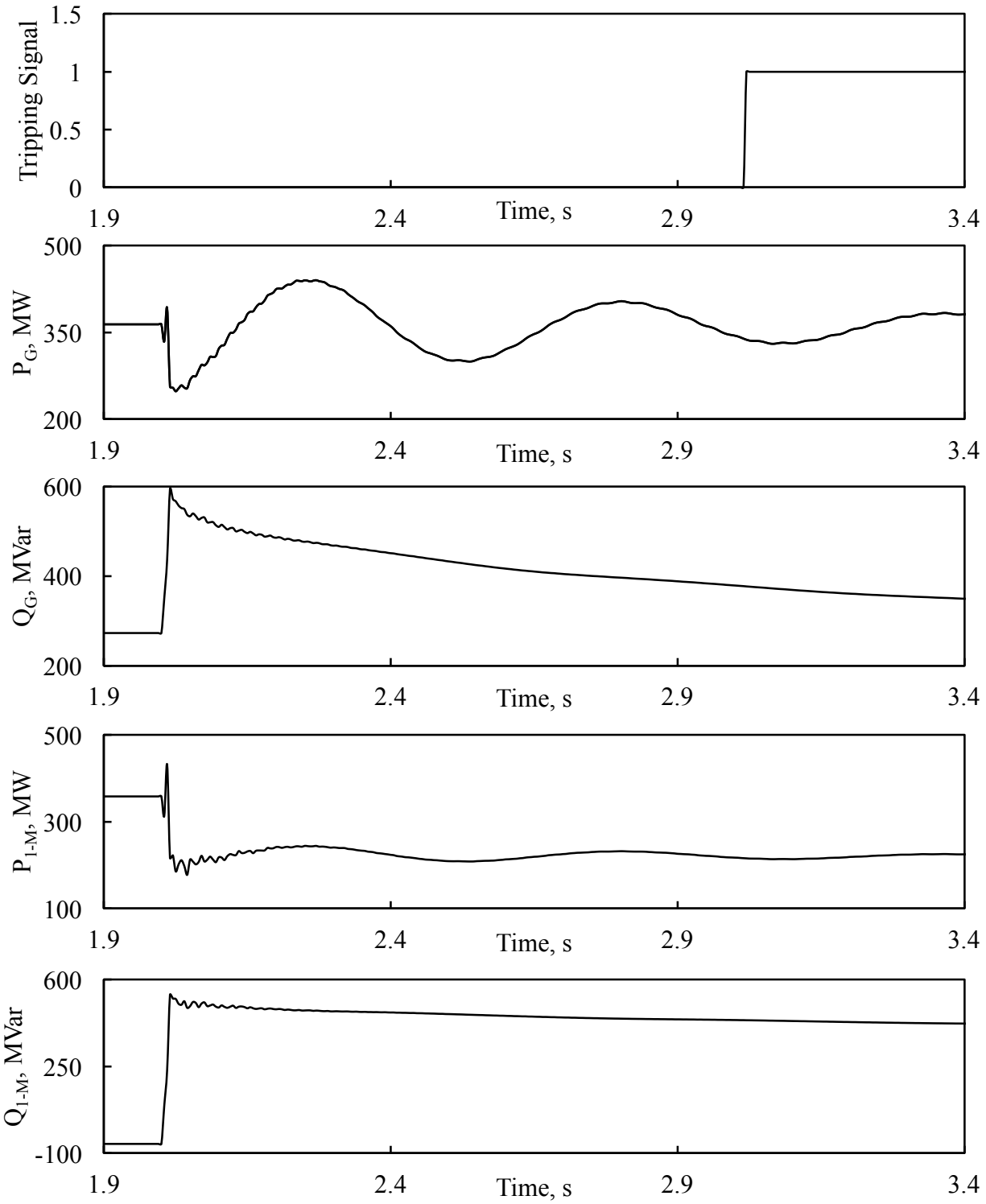

Figure C.15: Relay (21) tripping signal, transient time responses of generator active and reactive powers, active and reactive power flows from bus 1 to bus M during a line-to-line fault at F_2 (no wind farm in the system, generator loading is 65%).

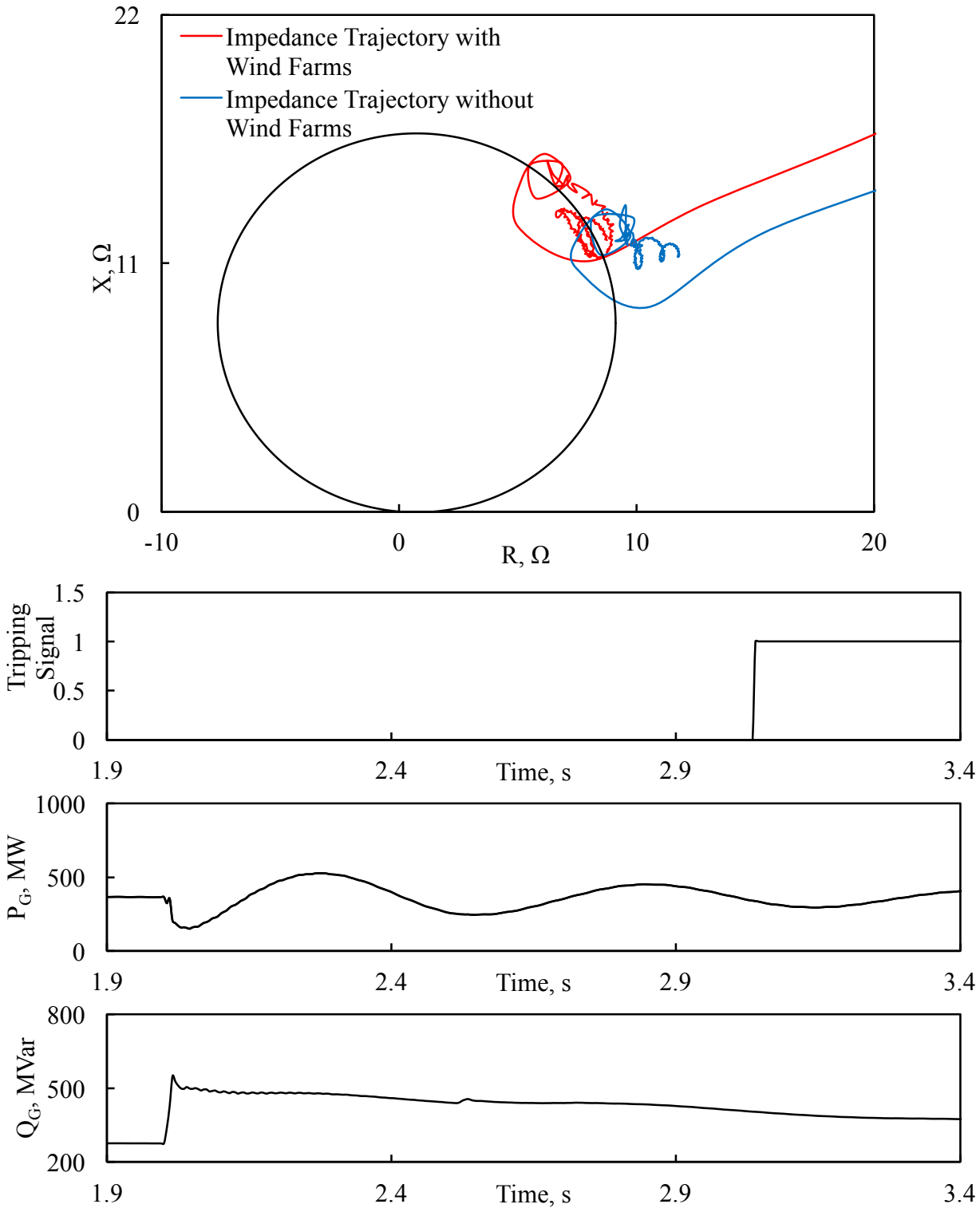

Figure C.16: Relay (21) measured impedance trajectory and its tripping signal, transient time responses of generator active and reactive powers, active and reactive power flows from bus 1 to bus M, DFIG- and FFC-based wind farm active and reactive powers during a line-to-line fault at F_2(generator loading is 65%).

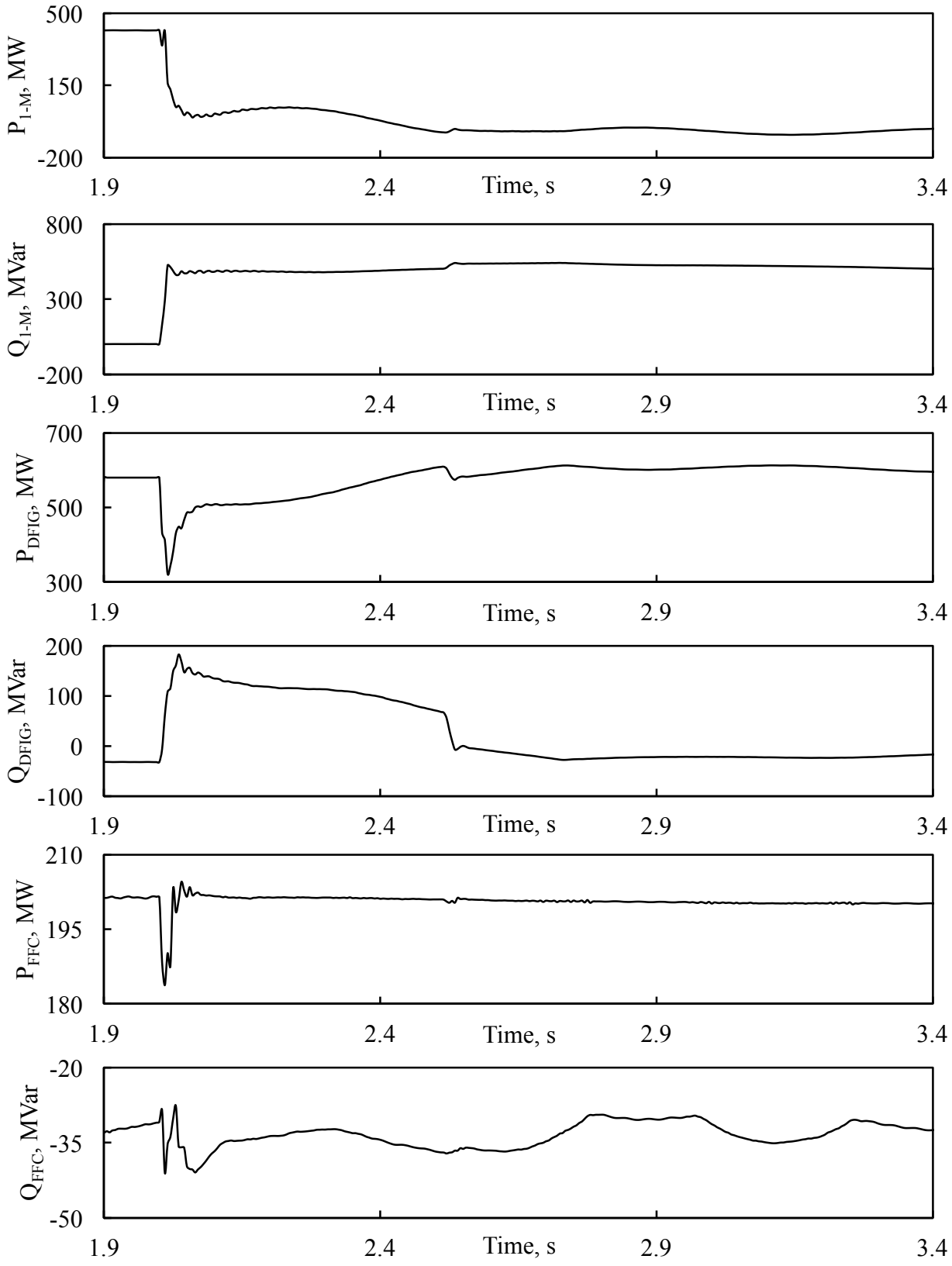

Figure C.16: Continued.

C.5 Performance of Relay (21) during a line-to-line fault at F_3

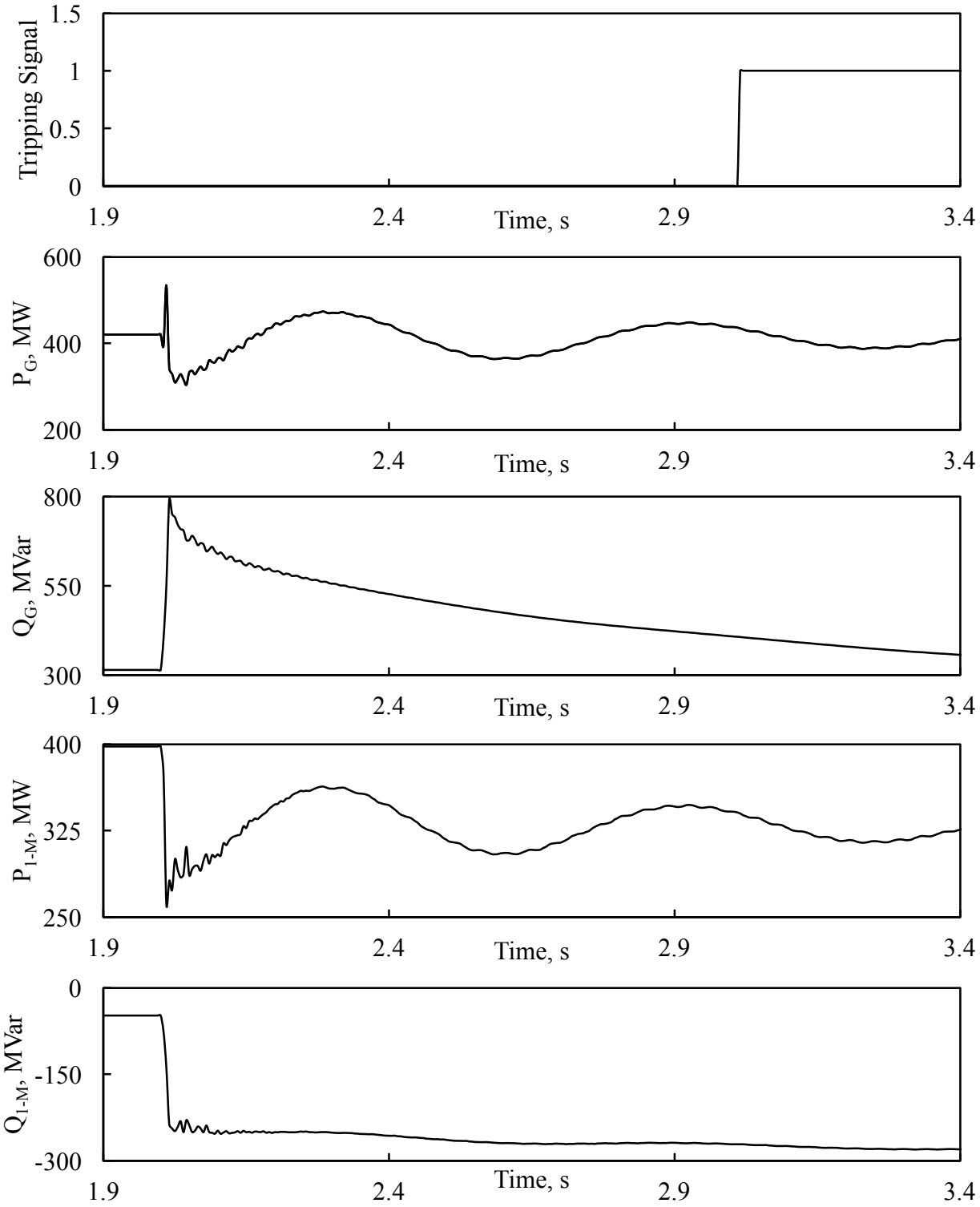

Figure C.17: Relay (21) tripping signal, transient time responses of generator active and reactive powers, active and reactive power flows from bus 1 to bus M during a line-to-line fault at F_3 (no wind farm in the system, generator loading is 75%).

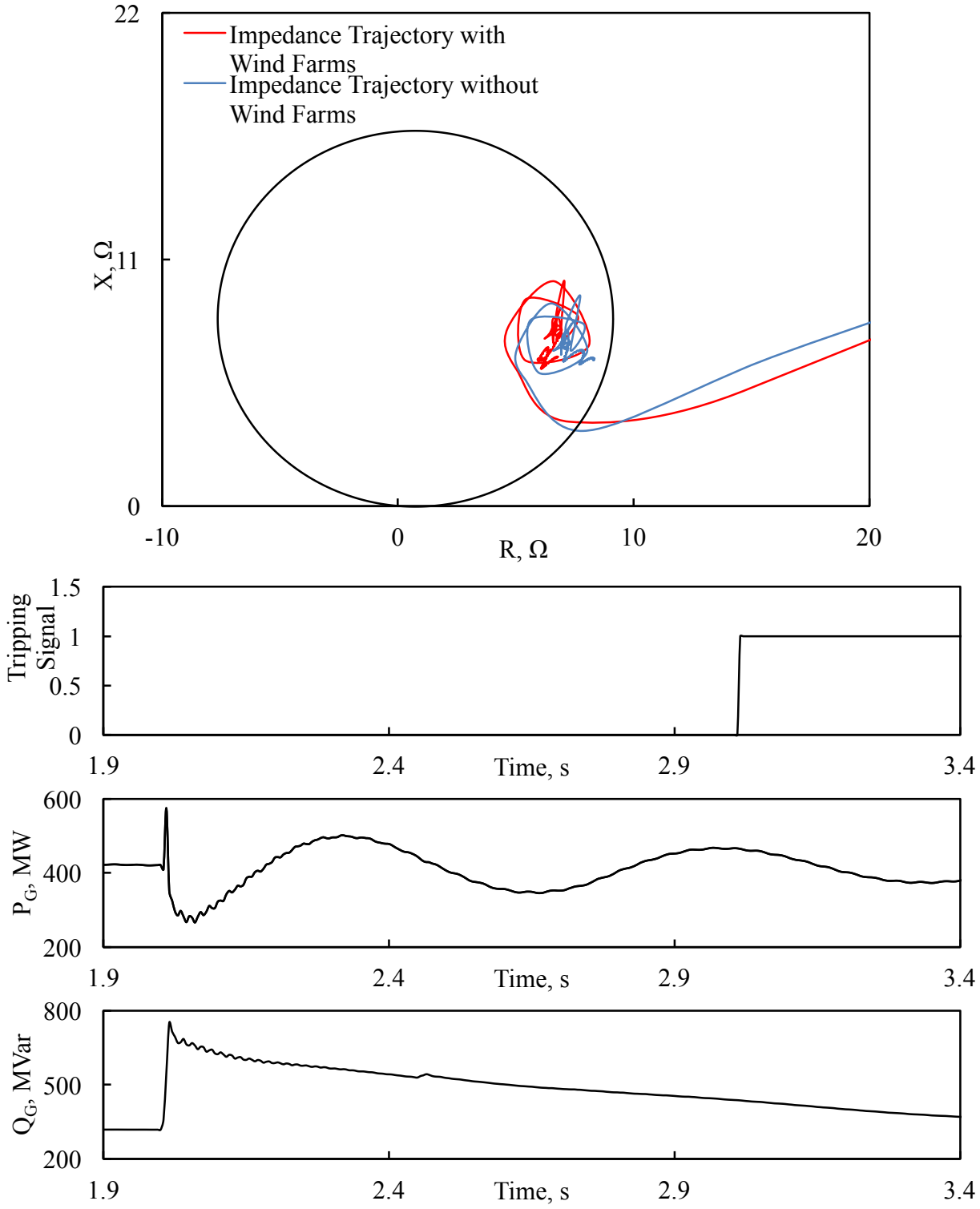

Figure C.18: Relay (21) measured impedance trajectory and its tripping signal, transient time responses of generator active and reactive powers, active and reactive power flows from bus 1 to bus M, DFIG- and FFC-based wind farm active and reactive powers during a line-to-line fault at F_3 (generator loading is 75%).

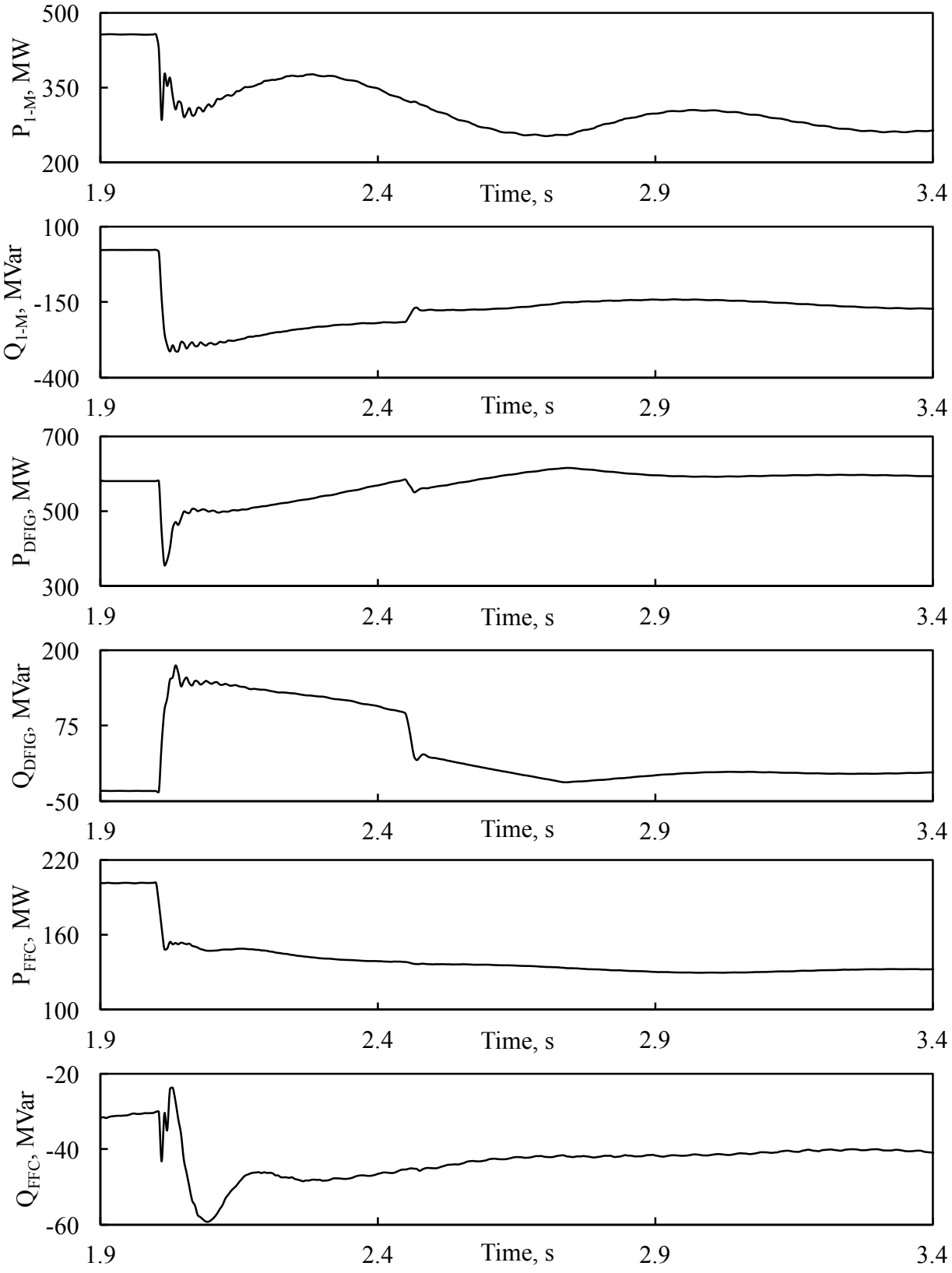

Figure C.18: Continued.

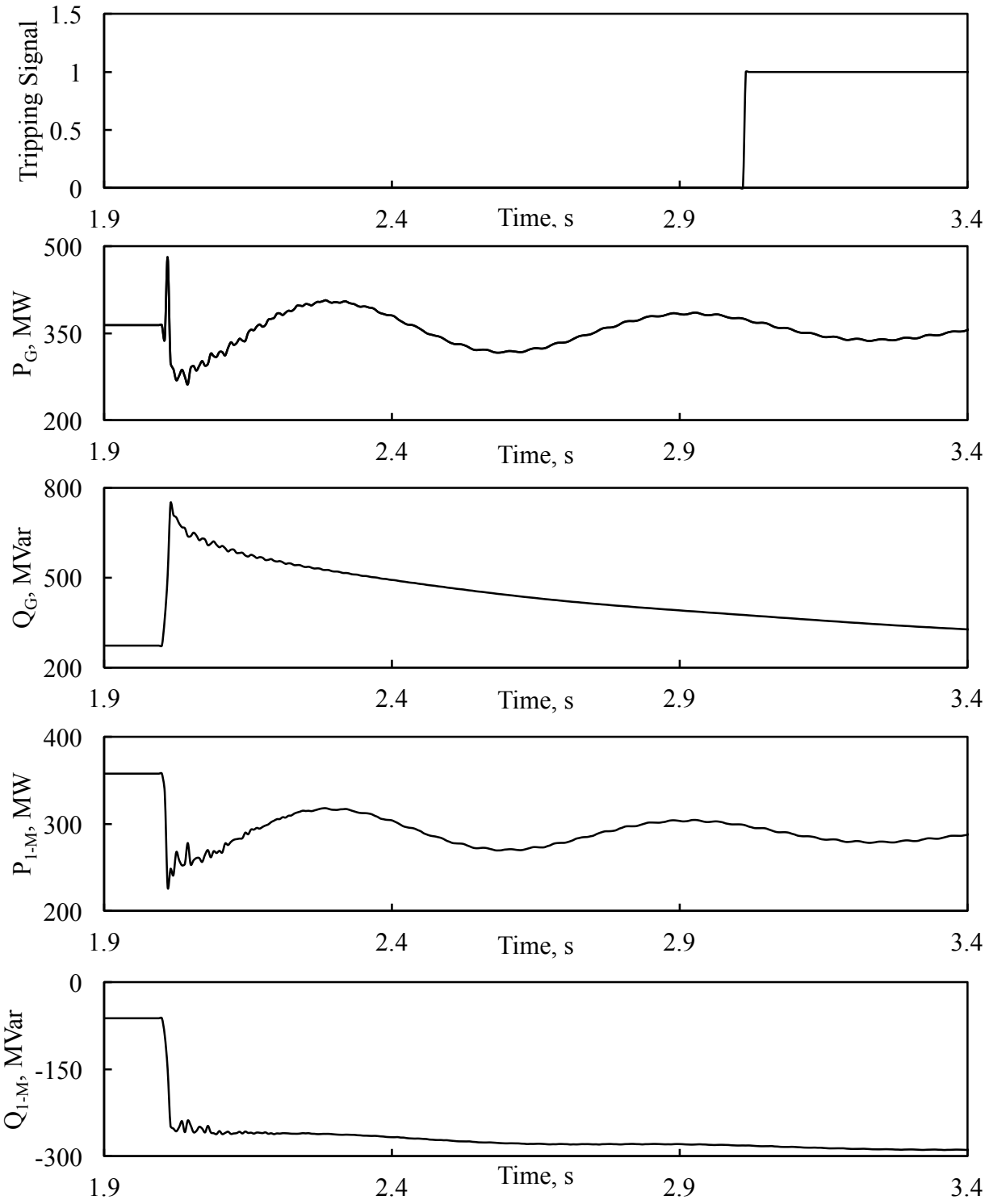

Figure C.19: Relay (21) tripping signal, transient time responses of generator active and reactive powers, active and reactive power flows from bus 1 to bus M during a line-to-line fault at F_3 (no wind farm in the system, generator loading is 65%).

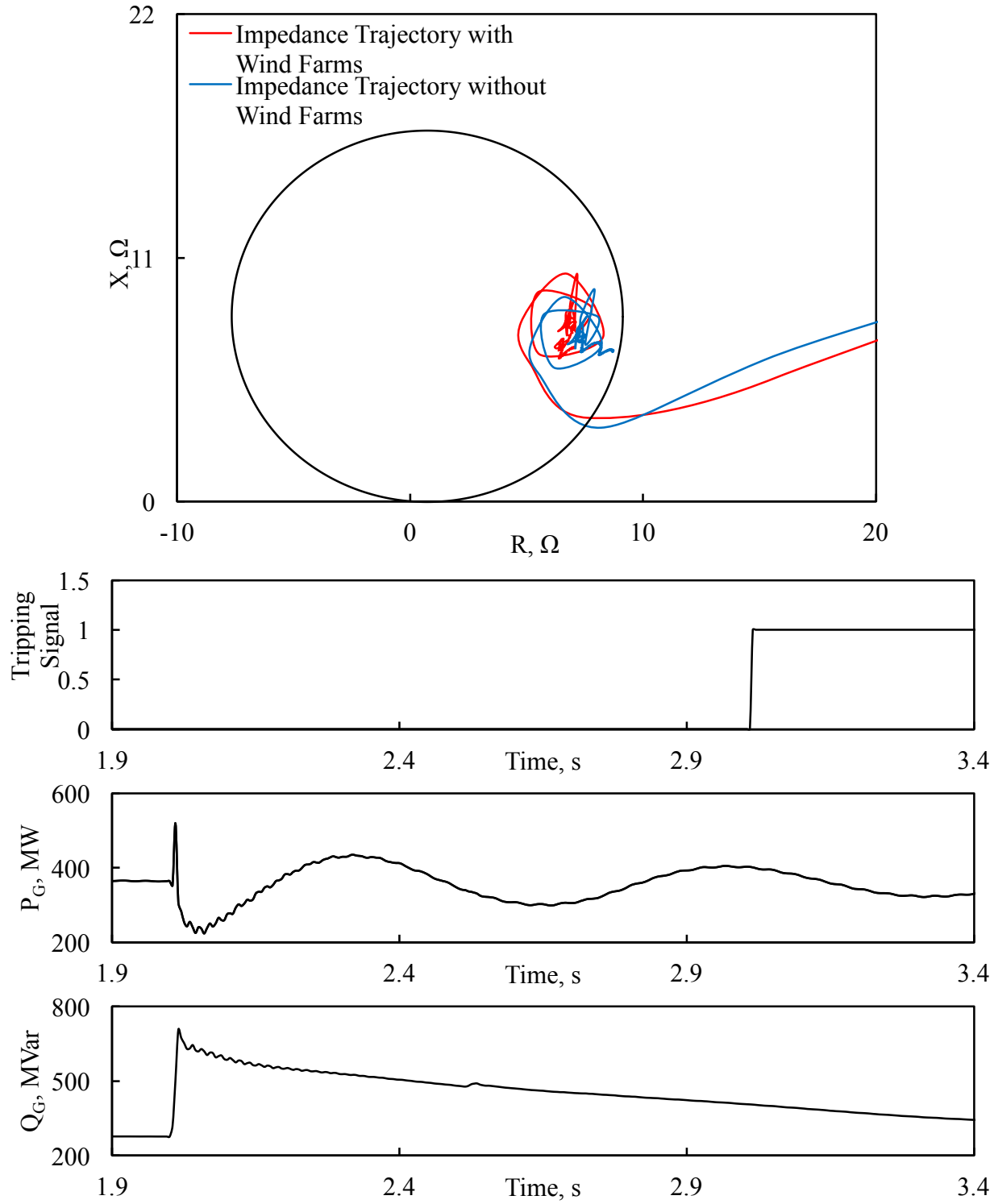

Figure C.20: Relay (21) measured impedance trajectory and its tripping signal, transient time responses of generator active and reactive powers, active and reactive power flows from bus 1 to bus M, DFIG- and FFC-based wind farm active and reactive powers during a line-to-line fault at F_3 (generator loading is 65%).

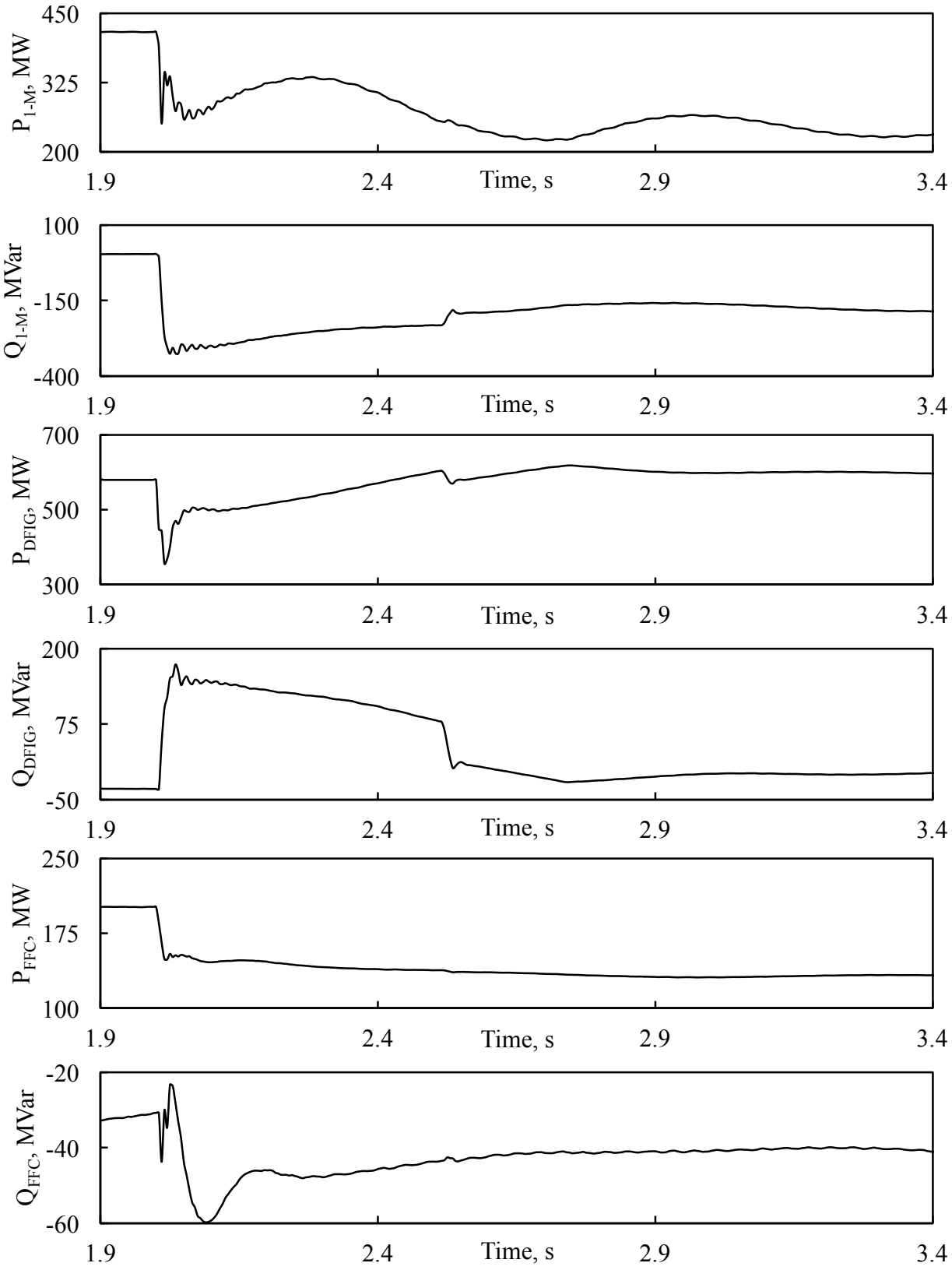

Figure C.20: Continued.